UNIVERSIDADE FEDERAL DE PERNAMBUCO-UFPE
CENTRO DE TECNOLOGIA E GEOCIÊNCIAS-CTG
DEPARTAMENTO DE OCEANOGRAFIA-DOCEAN
PROGRAMA DE PÓS-GRADUAÇÃO EM
OCEANOGRAFIA

PEDRO TYAQUIÇÃ DA SILVA SANTOS

INFLUENCE OF REMOTE PROCESSES ON A SPACE-TIME VARIABILITY OF THE AMAZON RIVER PLUME

Recife
2017

PEDRO TYAQUIÇÃ DA SILVA SANTOS

INFLUENCE OF REMOTE PROCESSES ON A SPACE-TIME VARIABILITY OF THE AMAZON RIVER PLUME

Tese apresentada ao Programa de Pós-Graduação em Oceanografia da Universidade Federal de Pernambuco como requisito para obtenção do título de **Doutor em Oceanografia**.

Área de concentração: Oceanografia

Orientador: Prof. Dr. Moacyr Cunha de Araújo Filho

Recife

2017

Catalogação na fonte
Bibliotecária Valdicea Alves, CRB-4 / 1260

S237i Santos, Pedro Tyaquiçã da Silva.
Influence of remote processes on a space-time variability of the Amazon River plume / Pedro Tyaquiçã da Silva Santos. - 2017.
97 folhas, Il., tabs. e Abr.

Orientadora: Prof. Dr. Moacyr Cunha de Araújo Filho.

Tese (Doutorado) – Universidade Federal de Pernambuco. CTG. Programa de Pós-Graduação em Oceanografia, 2017.
Inclui Referências.
Idiona Inglês.

1. Oceanografia. 2. Pluma do rio Amazonas. 3. Interação física-biogeoquímica. 4. Atlântico tropical. 5. Teleconecções ENSO. 6. aCDOM. I. Araújo Filho, Moacyr Cunha de (Orientadora). II. Título.

UFPE

551.46 CDD (22. ed.) BCTG/2017-395

Pedro Tyaquiçã da Silva Santos

INFLUENCE OF REMOTE PROCESSES ON A SPACE-TIME VARIABILITY OF THE AMAZON RIVER PLUME

Tese apresentada ao Programa de Pós-Graduação em Oceanografia do Departamento de Oceanografia da Universidade Federal de Pernambuco, como requisite para obtenção do grau de Doutor em Oceanografia.

Aprovada em 30 de agosto de 2017.

BANCA EXAMINADORA

_____

Prof. Dr. Moacyr Cunha de Araujo Filho
(Orientador/Presidente/Titular Interno – PPGO/UFPE)

_____

Profª. Drª. Monica Ferreira da Costa
(Titular Interna – PPGO/UFPE)

_____

Prof. Dr. Paulo Eurico Pires Ferreira Travassos
(Titular Interno – PPGO/UFPE)

_____

Prof. Dr. Pedro Augusto Mendes de Castro Melo
(Titular Externo – DOCEAN/UFPE)

_____

Dr. Gbeko Aubains Hounsuo-Gbo
(Titular Externo – CEERMA/UFPE)

Agradecimentos

Agradeço à Deus pela minha saúde e da minha família. Sem isso nada é possível.

Aos meus amados pais Fernando Moreira da Silva Santos e Nyedja Aracy Moreira da Silva Santos por todo seu amor.

Ao professor Dr. Moacyr Araújo por sua amizade, orientação, confiança e incentivo desde que cheguei no Departamento de Oceanografia.

À professora Dra. Maycira Costa pela sua ajuda e orientação durante a obtenção dos dados *in situ*.

À professora Dra. Dóris Veleda por toda sua ajuda e ensinamentos ao longo deste doutorado.

À banca avaliadora desta tese, minha total admiração e meus agradecimentos pelas críticas e sugestões para melhoria deste trabalho.

À Coordenação de Aperfeiçoamento de Pessoal de Nível Superior (CAPES) pela concessão da Bolsa de Doutorado.

Aos amigos do CEERMA e do LOFEC, pela amizade compartilhada ao longo desses anos. A todos os amigos da pós-graduação do DOCEAN pela amizade e momentos de descontração vivenciados sempre que possível. Aos professores do DOCEAN, os quais muito me ensinaram e compartilharam de suas experiências.

Aos funcionários e demais colegas do CEERMA e do DOCEAN pela boa convivência e atenção a mim prestadas. Agradeço especialmente à Myrna Lins por toda ajuda dispensada durante o doutorado.

Enfim, minha gratidão a todos que, de uma forma ou de outra, contribuíram para a conclusão deste trabalho.

Abstract

The main objective is to evaluate how teleconnections of chlorophyll-*a* (*Chl*) and sea surface salinity (SSS) to oceanic climatic phenomena (e.g. El Niño Southern Oscillation, Atlantic Dipole, etc.). To meet this objective, we addressed: (1) a spatio-temporal variability of *Chl* and SSS over the Amazon River plume; and (2) the relationship between climatic indexes and spatiotemporal patterns in the variables. The results are presented through three manuscripts submitted to scientific journals. The 10-year MODIS/Aqua dataset was used to determine the seasonal and interannual variability of *Chl* in the western tropical North Atlantic (WTNA) under the influence of local forcing (Amazon River flow (Q), sea surface temperature (SST), meridional wind stress (τy) and zonal current (u)) and remote (canonical (EC) and Modoki (EM) El Niños). There has been a change in ENSO in recent decades to an increasing frequency of EM over EC mode. EM events remotely induce above-normal rainfall over the Amazon basin, which increases Q and nutrient supply in the WTNA. This study suggests that, interannual and annual positive anomalies of *Chl* concentration in the WTNA depends on rainfall/Q events forced mainly by EM mode. A variability of SST in the Pacific and Atlantic influences strongly precipitation changes in the Amazon River basin, impacting the river flow and consequently SSS in the Amazon plume. An analysis of the Orthogonal Empirical Function (FSO) was performed with 46 years of SST data, rainfall and SSS, in order to establish a relationship between these variables. The results show that the influence of El Niño Modoki on the spatial pattern of rainfall in the Amazon basin is a preponderant factor for positive anomalies of *Chl* and negative anomalies of SSS over the Amazon River plume. In addition, a characterization of the relationship between a spectral absorption of the colored dissolved organic matter (*a*CDOM) and the salinity on the Amazon River plume demonstrate the freshwater dispersion and biogeochemical variability in the WTNA. These results support future studies on large-scale climate variability, thermohaline circulation, global hydrological cycle, sediment deposition, biogeochemistry, oceanic fluxes, CO_2 absorption and ecological impacts in the food chain over the WTNA.

Keywords: Amazon river plume. Physical-biogeochemical interaction. Tropical atlantic. ENSO teleconnections. *a*CDOM.

Resumo

O objetivo principal desta tese foi avaliar as teleconecções da clorofila-a (*Chl*) e da salinidade da superfície do mar (SSM) aos fenômenos climáticos oceânicos (ex. El Niño Oscilação Sul, Dipolo do Atlântico, etc.). Para atender este objetivo, foram avaliados: (1) a variabilidade espaço-temporal de *Chl* e SSM sobre a pluma do Rio Amazonas e (2) a relação entre os índices climáticos e os padrões espaço-temporais dessas variáveis. Os resultados são apresentados através de três manuscritos submetidos para revistas científicas. O conjunto de dados MODIS/Aqua de dez anos foi usado para determinar a variabilidade sazonal e interanual da *Chl* no Oceano Atlântico Tropical Norte (OATN) sob a influência de forçantes locais (vazão do Rio Amazonas (Q), temperatura da superfície do mar (TSM), estresse meridional do vento (τy) e a corrente zonal (u)) e remotas (El Niño canônico (EC) e El Niño Modoki (EM)). As mudanças no ENOS nas últimas décadas apontam para uma frequência crescente do EM sobre o modo EC. Os eventos de EM induzem chuvas acima do normal sobre a bacia do Rio Amazonas, o que aumenta a Q e o suprimento de nutrientes no OATN. Este estudo sugere que, as anomalias anuais e interanuais de concentração de *Chl* sobre o OATN dependem dos eventos de chuva/vazão forçados principalmente pelo modo EM. A variabilidade da TSM no Pacífico e no Atlântico influencia fortemente as mudanças de precipitação na bacia do Rio Amazonas, impactando a vazão do rio e consequentemente a salinidade da superfície do mar (SSM) no OATN. Uma análise da Função Ortogonal Empírica (FOE) foi realizada com 46 anos de conjuntos de dados de TSM, chuva e SSM, a fim de estabelecer a relação entre essas variáveis. Os resultados apresentados mostram que a influência do El Niño Modoki sobre o padrão espacial de chuvas na bacia do Amazonas é um fator preponderante para as anomalias positivas de *Chl* e anomalias negativas de SSM na pluma do Rio Amazonas. Além disso, uma caracterização da relação entre a absorção espectral da matéria orgânica dissolvida colorida (*a*CDOM) e a salinidade apresentada no âmbito do cruzeiro oceanográfico Camadas Finas V realizado sobre a pluma do Rio Amazonas, demonstra uma indicação da dispersão de água doce e da variabilidade biogeoquímica no OATN. Estes resultados servem de subsídios para futuros estudos sobre variabilidade climática em larga escala, circulação termohalina, ciclo hidrológico global, deposição de sedimentos, biogeoquímica, fluxos de atmosfera oceânica, absorção de CO_2 e impactos ecológicos na cadeia alimentar no OATN.

Palavras-chave: Pluma do rio Amazonas. Interação física-biogeoquímica. Atlântico tropical. Teleconecções ENSO. *a*CDOM.

List of Illustrations

List of Tables

List of Abbreviations

*a*CDOM	CDOM absorption coefficient
ADCP	Acoustic Doppler Current Profilers
AMM	Atlantic Meridional Mode
ASCAT	Advanced Scatterometer
AVHRR	Advanced Very High-Resolution Radiometer
cc	Cross-correlation
CDOM	Chromophoric Dissolved Organic Matter
Chl	Chlorophyll-*a*
CI	Color Index algorithm
CTA	Atlantic Cold Tongue
CTD	Conductivity, temperature, and pressure probe
DHN	*Diretoria de Hidrografia e Navegação Marinha do Brasil*
DOC	Dissolved Organic Carbon
DOM	Dissolved Organic Matter
dof	Degrees of Freedom
DPR	Dual-Frequency Precipitation Radar
EC	canonical El Niño
ECMWF	European Centre for Medium-Range Weather Forecasts
EM	El Niño Modoki
EMI	El Niño Modoki Index
ENSO	El Niño Southern Oscillation
EOF	Empirical Orthogonal Function
GPCC	Global Precipitation Climatology Centre
GV	Ground Validation
IR	Infrared
ITCZ	Intertropical Convergence Zone
Kd490	Attenuation coefficient at 490 nm
MCMs	Moored Current Meters
MODIS	Moderate Resolution Imaging Spectroradiometer
NBC	North Brazilian Current
NBCS	North Brazilian Continental Shelf
NECC	North Equatorial Counter Current

NEMO	Nucleus for European Modelling of the Ocean
NOAA	National Oceanic and Atmospheric Administration
NTA	North Tropical Atlantic Index
OC3	Ocean Color version 3 algorithm
OCx	Ocean Color algorithm
OI	Optimal Interpolation
ORAS4	Ocean ReAnalysis System 4
OSCAR	Ocean Surface Current Analyses
PCA	Principal Component Analysis
POES	Polar Operational Environmental Satellites
PP	Primary production
PSU	Practical Salinity Unit
Q	River discharge
QC	Quality control
QuickSCAT	Quick Scatterometer
R/S	Remote sensing
SAL	Salinity in PSU
SCF	Squared Covariance Fraction
SSH	Sea Surface Height
SSS	Sea Surface Salinity
SST	Sea Surface Temperature
SVD	Singular Value Decomposition
TNA	Tropical Northern Atlantic Index
TRMM	Tropical Rainfall Measuring Mission
TSA	Tropical Southern Atlantic Index
u	Zonal current
UFPE	*Universidade Federal de Pernambuco*
UV	Ultra-violet
UVic	University of Victoria
WOA05	World Ocean Atlas 2005 database
WTNA	Western Tropical North Atlantic
λ	Wavelength
σ	SST anomalies standard deviation

Θ	Satellite zenith angle
τ_y	Meridional wind stress

Summary

1 INTRODUCTION AND OBJECTIVES

Plumes of large rivers are places of intense ecological complexity and biogeochemical transformation and play an important role in oceanic physical processes (McKee et al., 2004; Hickey et al., 2010). The Amazon River has the largest hydrographic basin and the largest flow in the world and is by far the largest single source of terrestrial freshwater for the Atlantic Ocean and contributes approximately 30% of the fluvial flow (Wisser et al., 2010). This flow is distinctly seasonal with minimum discharge occurring in November (~0.8 x 10^5 m^3 s^{-1}) and maximum discharge occurring in late May (2.4 x 10^5 m^3 s^{-1}) (Lentz, 1995). This flux impacts the surface western tropical North Atlantic (WTNA) water density more than 3500km from the Amazon River mouth (Hellweger and Gordon, 2002), and causes a surface discoloration readily detectable in satellite ocean color data that can extend over areas as large as 500,000 km^2 (Subramanian et al., 2008) (Figure 1). The Amazon River plume signature, which is characterized by large amounts of low-salinity waters, nutrients and suspended and dissolved material, has different dispersion patterns during the year. Amazon waters enters the WTNA near the equator and is carried northwestward along the Brazilian Shelf by the North Brazilian Current (NBC) (Muller-Karger et al., 1988). Although, part of the Amazon plume waters continues northwestward into the Guyana Current, a sizable fraction reaching 3° N – 10° N is carried eastward by the North Equatorial Counter Current (NECC) (Fratantoni and Glickson, 2002) which reaches maximum velocities during the boreal summer to fall period.

The Amazon River plume has a great influence on the northeastern South American coast, the Caribbean and Equatorial Atlantic Ocean, particularly regarding to phytoplankton biomass and primary productivity (Smith and DeMaster, 1996), coastal deposition and erosion (Froidefond et al., 2002), carbon sink and nutrient input (Cooley et al., 2007) and ocean atmosphere interactions as ring and hurricane intensification (Ffield, 2007). In the North Brazilian Continental Shelf (NBCS) the Amazon plume is subject to energetic forcing from various environmental factors. The most significant of these factors include the ocean currents, the wind field, tidal variations and large amount of energy resulting from the river discharge (Geyer et al., 1995; Nittrouer and DeMaster, 1996). All these forcing variables have large spatial and temporal variability, and consequently exert a unique influence on the Amazon plume waters dispersal.

Figure 1. Map of the study area in the WTNA region under the influence of the Amazon River plume. Monthly mean *Chl* (mg m^{-3}) in log_{10} scale, for August/September climatology (2002 to 2015) derived from MODIS/Aqua.

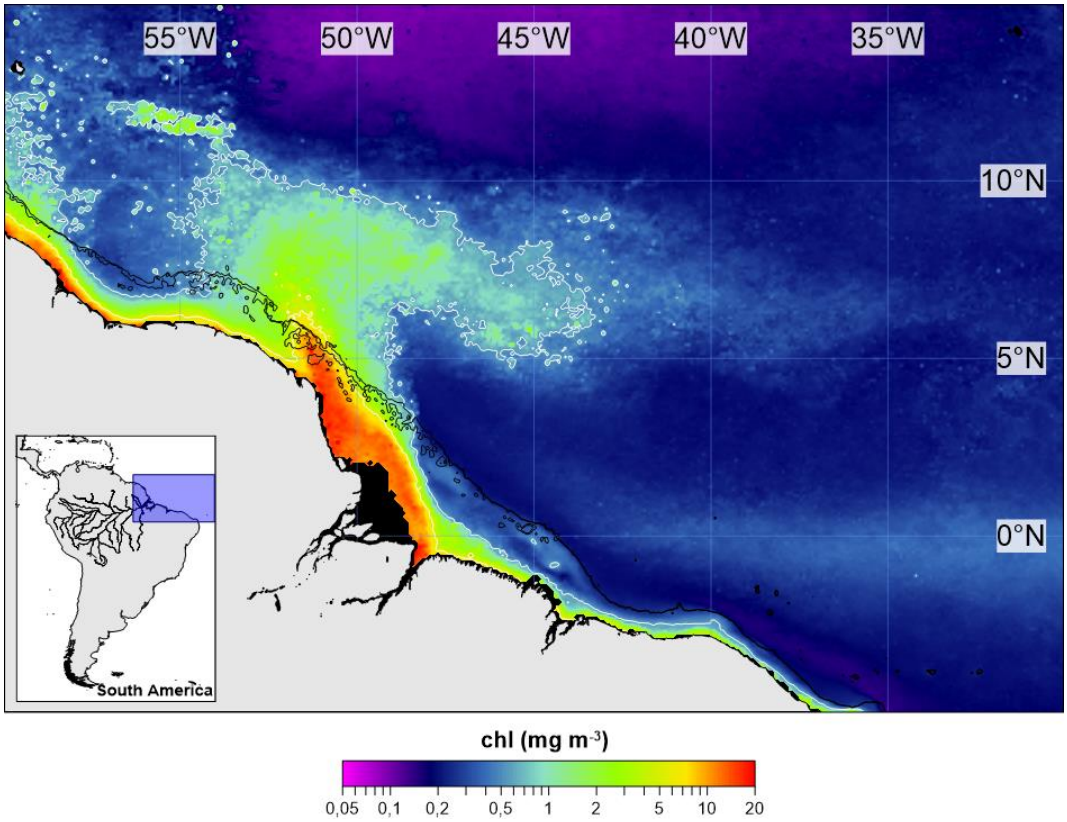

Source: the author

Changes in Sea Surface Salinity (SST) patterns caused by large river plumes indicate where marine and terrestrial systems mix. The variability of ocean salinity is an indicator of changes in the global hydrological cycle and large-scale climatic variability. It has an important role in the thermohaline circulation in the distribution of mass and heat and reflects the patterns of ocean-atmosphere fluxes (evaporation, precipitation, heat, energy and solubility). The terrestrial nutrients that are carried through the drainage of the Amazon River basin and consequently into the ocean are responsible for the increase of the phytoplanktonic biomass and Primary Production (PP) and, like salinity, alter the biogeochemical cycles causing a substantial of CO_2 uptake, thus impacting the local habitat. With the launch of satellites Remote sensing of the oceans historically has been estimating the concentration of chlorophyll-a (*Chl*) in the open ocean. Knowledge of the heterogeneity of the *Chl* concentration in oligotrophic waters is essential for understanding the dynamics of marine ecosystems. As the main optical variable, *Chl* assumes important role in biogeochemistry due to the pigment biomass in the water that is originated by phytoplankton photosynthesis.

Rainfall over the Amazon basin exhibits distinct spatial and temporal variability, partly due to climate signals in the Tropical Pacific, such as the El Niño Southern Oscillation (ENSO),

and part occurring as a function of the surface temperature gradient in the Tropical Atlantic, called the Atlantic Dipole. The effects of ENSO on South America have a strong impact on rainfall, flow, floods and erosion along the drainage of the Amazon River basin towards the sea. ENSO is a coupled ocean-atmosphere phenomenon occurring across the Tropical Pacific, characterized by irregular fluctuations between warm (El Niño) and cold (La Niña) phases with periodicity ranging from 2 to 7 years. Because ENSO is major source of interannual climate variability over much of South America, its impact on Amazon climate has been well studied (Garreaud et al., 2008). It's well known that "no two El Niño events are quite alike" (Wyrtki, 1975), yet the typical evolution of such event was thought to consist in an initial warming of South America and later in the central equatorial Pacific during austral summer (DJF) (Rasmusson and Carpenter, 1982). This belief changed with the extraordinary 1982–83 and 1997–98 El Niño events, which had large amplitudes and different evolutions with respect to the "canonical" composite (Cane, 1983). Recently, several studies argue for the existence of a different type of El Niño, the "Modoki" mode, with SST anomalies concentrated in the central equatorial Pacific, (Ashok et al., 2007; Kug et al., 2009; Kao and Yu, 2009), and there has been an increasing interest in determining the characteristics of its evolution, dynamics and associated teleconnections (e.g., Weng et al., 2007; Kao and Yu, 2009; Kug et al., 2009; Yu and Kim, 2010). Furthermore, there is evidence that of El Niño Modoki has been more frequent during the last decades (Yeh et al., 2009; Lee and McPhaden, 2010). According to some climate models an increase in the frequency of occurrence of the El Niño Modoki is justified by the anthropogenic climate change (Yeh et al., 2009). Unfortunately, the spatiotemporal distribution of rainfall in remote areas is difficult to describe and fraught with many problems, especially in the Andes and adjacent Amazon drainage basin, where mountainous terrain and dense vegetation prevent implementation and maintenance of a densely spaced rain-gauge network, measuring rainfall distribution and amount is difficult (Ronchail et al., 2002). Despite the remoteness, there are rain-gauge data in some sectors of the Amazon catchment region that provide a coherent view of temporal rainfall variations. Large-scale rainfall monitoring in the Amazon basin has benefitted from innovative remote-sensing products, as the Tropical Rainfall Measuring Mission (TRMM) and provides insights into these processes (Laraque et al., 2007).

The main objective of this thesis is to evaluate the Amazon plume chlorophyll-a (*Chl*) and sea surface salinity (SSS) teleconnections to ocean climate phenomena. To achieve this intent, specific goals were performed: (1) evaluate the *Chl* and SSS spatio-temporal variability over the Amazon River plume and (2) Assess the relationship of the climatic indices to the spatio-temporal patterns of these variables. This thesis brings an overview of the study area, a

description of the remote sensing, model and climate indices datasets and analysis tools. The results are presented by a copy of the three manuscripts submitted to scientific journals and, finally, the main conclusions and perspectives.

2 THE STUDY AREA

This thesis concentrates on the western tropical North Atlantic (WTNA) with focus more precisely at the Amazon plume continuum. The purpose here is to introduce the area of study with a view of the major variables that influence it.

The North Brazil Current (NBC) (Figure 2) is a western boundary current and flows to the northwest with maximum speeds around 1.0 ms^{-1} (Richardson et al., 1994), with average transport of 26 Sv. In July – August occurs the maximum transport of 36 Sv and the minimum transport (13 Sv) in April - May (Johns et al., 1998). The NBC transport dynamics also produce several meso-scale rings along their flow (Fratantoni and Glickson, 2002), so that they assume greater hydrodynamic importance in the environment than the platform break.

Thus, the Amazon plume is strongly pressured against the coast by the northeast trade winds (until May), being diverted to the northwest towards the Caribbean Sea due to the trade winds direction shift from northeast to southeast from June (Lentz et al., 1995). A synoptic view of the seasonal variablity of the main variables that influence the WTNA region is presented in the Figures 3, 4, 5 and 6.

Figure 2. Schematic representation of the main surface currents that interact with the Amazon plume in the study area. A MODIS/Aqua *Chl* image for the month of September 2009 is used to highlight the NBC retroflection and the NBC anticyclonic ring displacement.

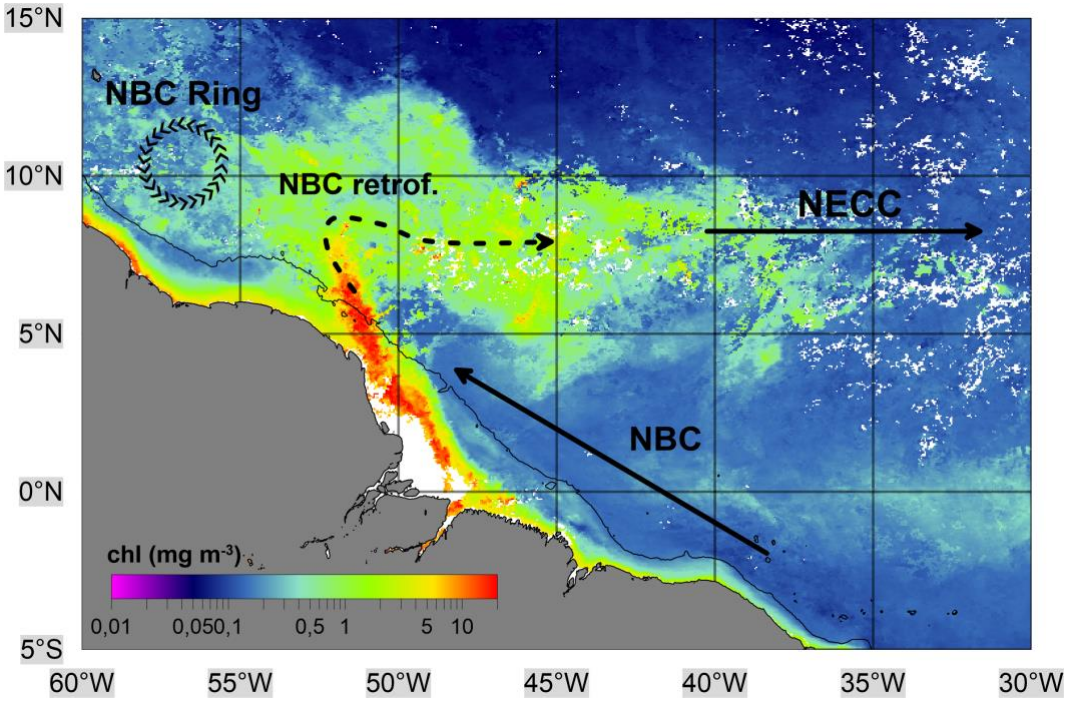

Source: the author

Figure 3. December, January and February climatology from 2002 to 2015 of *Chl* (a), SSS (b), rainfall (c), SST (d), wind speed (e) and ocean currents velocity (f) for the study area.

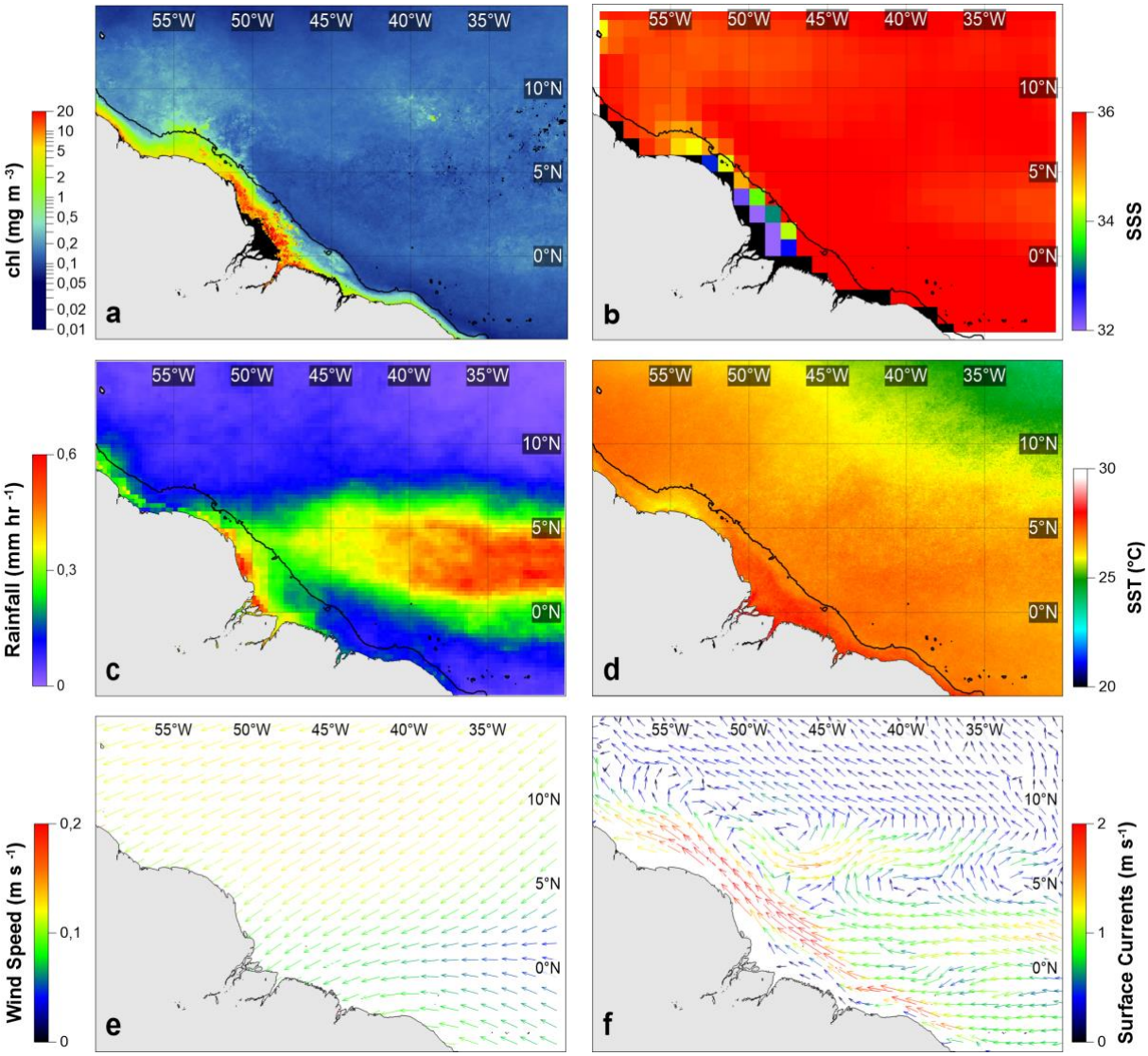

Source: the author

The December, January and February climatology from 2002 to 2015 of *Chl* (Figure 3a), SSS (Figure 3b), rainfall (Figure 3c), SST (Figure 3d), wind speed (Figure 3e) and ocean currents velocity (Figure 3f) for the study area show a well-defined pattern. The Chl is cofined to continental shelf, as the the SSS. The rainfall is instense in the region below 5° N, and the SST presents a temperature of 25 °C in the northern part, above 10° N. The wind speed is more intense to the eastward direction towards the river mounth near the equator (0°) as the current velocity is more intense above the shelf towards the northwestern direction.

Figure 4. March, April and May climatology from 2002 to 2015 of *Chl* (a), SSS (b), rainfall (c), SST (d), wind speed (e) and ocean currents velocity (f) for the study area.

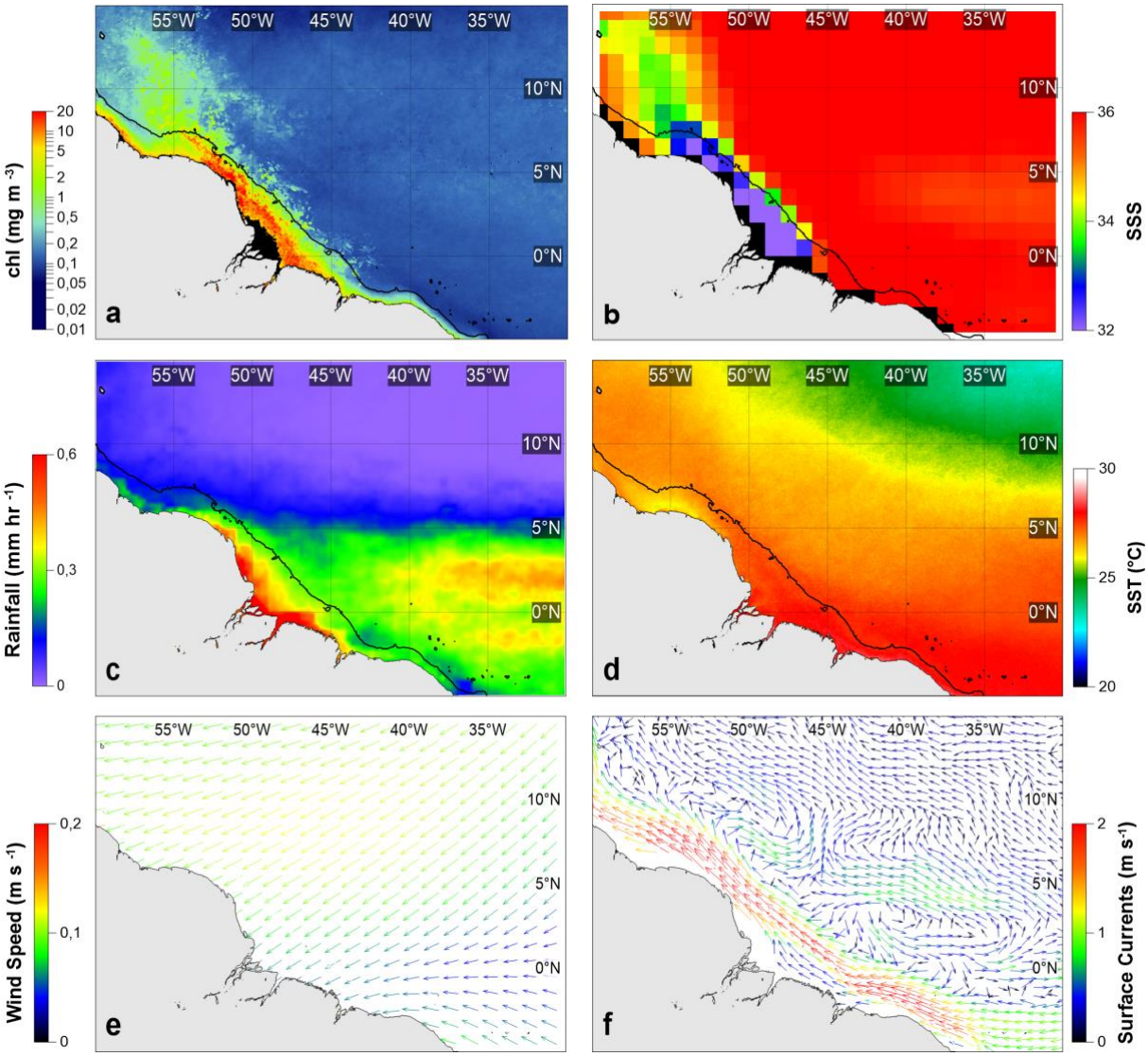

Source: the author

In the March, April and May climatology from 2002 to 2015 the *Chl* (Figure 4a) extendends beyond the continental shelf in the northwestward direction. The SSS (Figure 4b) flows the same pattern as the *Chl*, the rainfall (Figure 4c) is weak but extends to a region below the equator and near the coast at west. SST (Figure 4d) still defined by temperatures of ~27 °C over the WTNA region and 10 °C below 10° N. Wind speed (Figure 4e) is weaker than DJF climatology (Figure 3e) although with the same direction. The ocean currents velocity (Figure 4f) for the study area is more confined above the shelf with the eastward branch weak than DJF climatology (Figure 3f).

Figure 5. June, July and August climatology from 2002 to 2015 of *Chl* (a), SSS (b), rainfall (c), SST (d), wind speed (e) and ocean currents velocity (f) for the study area.

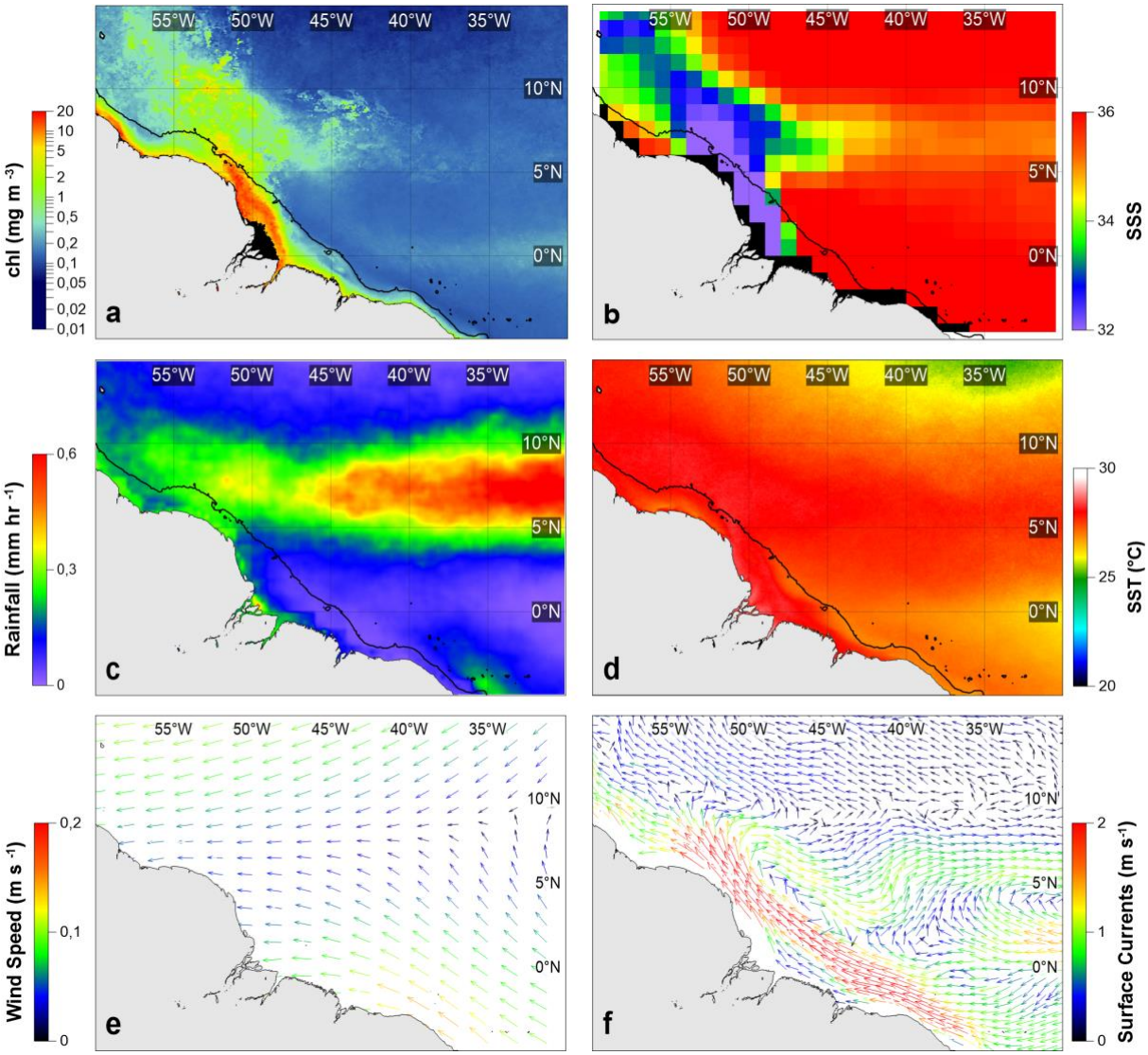

Source: the author

In the climatology for June, July and August from 2002 to 2015, the Chl (Figure 5a) extends beyond the continental shelf in a retroflection pattern towards eastward direction. The SSS (Figure 5b) flows the same pattern as the Chl. The rainfall (Figure 5c) shifts above 5° N, with more intense precipitations. SST (Figure 5d) with temperatures above 27° C covers a major area over the WTNA. Wind speed (Figure 5e) is more intense towards west direction, near 5° N. The ocean currents in this region (Figure 5f) are more intense above the shelf and near the retroflection branch.

Figure 6. September, October and November climatology from 2002 to 2015 of *Chl* (a), SSS (b), rainfall (c), SST (d), wind speed (e) and ocean currents velocity (f) for the study area.

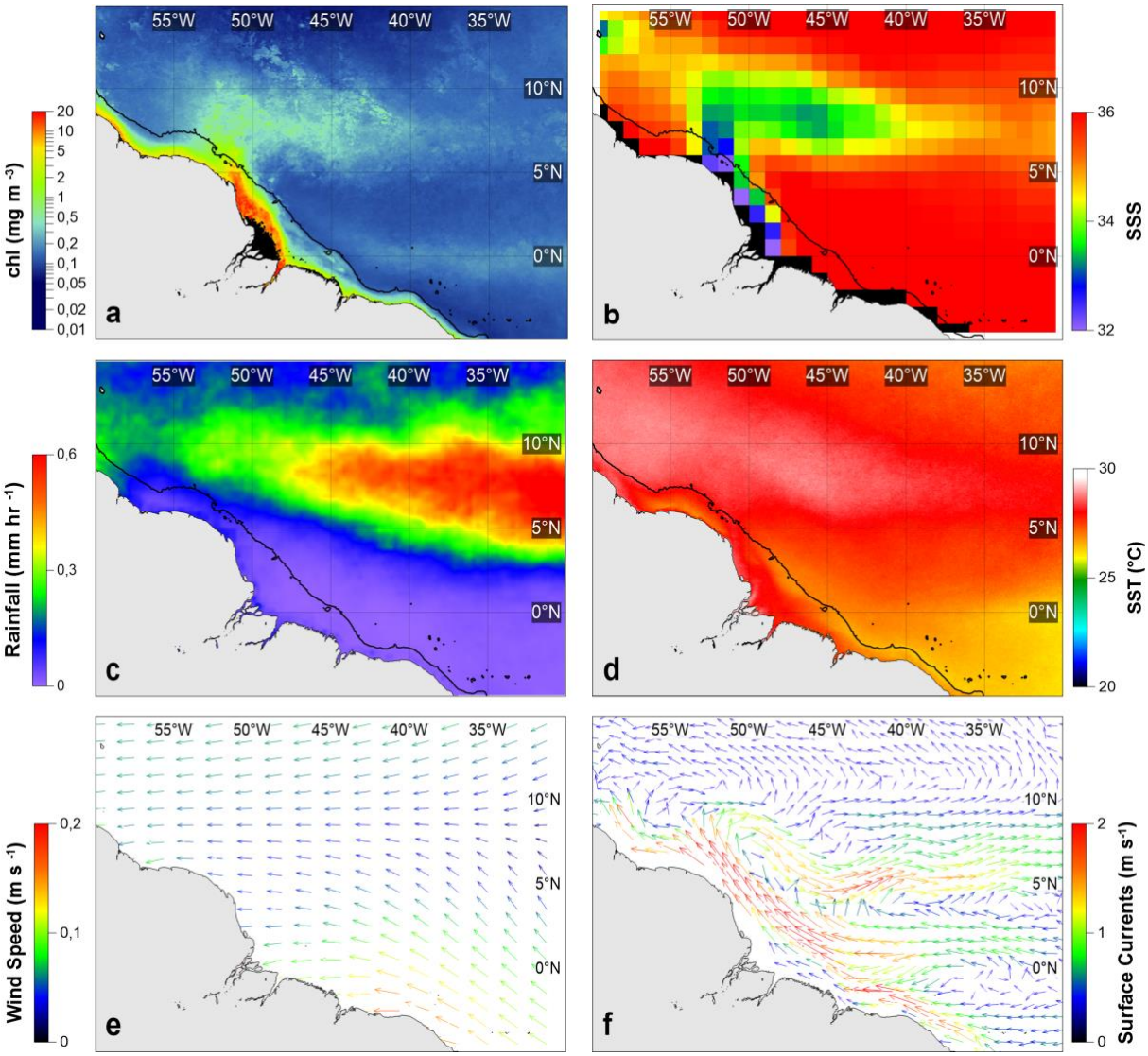

Source: the author

The October, November and December climatology for 2003 to 2012 presents the *Chl* (Figure 6a) with major concentration above the retroflected Amazon River plume. As the same patterns exposed before the SSS (Figure 6b) pattern is similar to the *Chl*, with salinity below 33. The Rainfall (Figure 6c) is still in the same position as the JAS climatology (Figure 5c). Altough the SST (Figure 6d) presents values near 30 °C in the same pattern as the *Chl*. The wind speed is still in the same direction but, the velocities are weaker than the JAS climatology. The ocean currents speed is by far more intense in the retroflection pattern than JAS climatology, with velocities near 2 m s^{-1}.

3 DATA AND METHODS

3.1 Data

Chlorophyll-*a* (*Chl*)

The satellite imagery has proven effective for deriving biophysical variables in waters dominated by phytoplankton at temporal and spatial scales difficult to attain with oceanographic surveys (Sathyendranath et al., 2004). Chlorophyll-a (*Chl*) concentrations have typically been the main biophysical variable derived from ocean-colour imagery.

Standard *Chl* concentration images produced by NASA Ocean Color Group using the Moderate Resolution Imaging Spectroradiometer (MODIS) sensor imagery are based on the OC3 (Ocean Color version 3) algorithm that returns the near-surface *Chl* concentration in mg m^{-3} (O'Reilly et al., 2000). The OC3 *Chl* product combines two algorithms, the O'Reilly et al. (1998) band ratio Ocean Color (OCx) and Hu et al. (2012) Color Index (CI) algorithm. The CI algorithm is a three-band reflectance formed linearly between the remote sensing reflectance (R_{rs}) in the blue, green and red bands, as follow:

$$CI = R_{rs}\left(\lambda_{green}\right) - \left[R_{rs}\left(\lambda_{blue}\right) + \left(\frac{(\lambda_{green} - \lambda_{blue})}{(\lambda_{red} - \lambda_{blue})}\right) * \left(R_{rs}(\lambda_{red}) - R_{rs}(\lambda_{blue})\right]\right. \quad (1)$$

Where $\lambda_{blue}, \lambda_{green}$ and λ_{red} are the instruments-specific wavelengths closest to 443, 555 and 670 nm respectively. The OCx algorithm is a fourth-order polynomial to derive *Chl* in logarithmic scale.

$$log_{10}(chl - a) = a_0 + \sum_{i=1}^{4} a_i \left(log_{10}\left(\frac{R_{rs}(\lambda_{blue})}{R_{rs}\left(\lambda_{green}\right)}\right)\right)^i \quad (2)$$

Where R_{rs} values and the coefficients, a_0-a_4, are sensor- specific. The MODIS/Aqua data used in this work are Monthly *Chl* surface data with 4 km spatial resolution from January of 2003 to December 2012 were obtained from the MODIS/Aqua sensor processed with standard NASA global coefficients (O'Reilly et al., 1998), available at oceancolor.gsfc.nasa.gov. The *Chl* data was analised and processed with the SeaDAS 7.4 software provided by NASA, available at https://seadas.gsfc.nasa.gov.

Sea Surface Temperature (SST)

The need for accurate global sea surface temperature (SST) fields has been receiving increasing attention, primarily because of their importance in understanding variability in the global climate. Satellite SST measurements are attractive because of their global repeated coverage compared to any other type of measurements of this quantity. Space-based multichannel infrared radiometers operating in cloud-free conditions provide the most reliable global SST data sets (Barton, 1995).

Since 1981, the National Oceanic and Atmospheric Administration (NOAA) series of Polar Operational Environmental Satellites (POES) spacecraft has carried the second generation Advanced Very High-Resolution Radiometer (AVHRR), an instrument with three infrared (IR) channels suitable for estimating SST (Schwalb, 1978). The channels 4 and 5 from the sensor are used to estimate the SST and operate in the wavelength regions between 3.5 and 3.9 μm and between 10 and 12.5 μm, where the atmosphere is comparatively transparent. The AVHRR/NOAA-19 sensor SST algorithm published by Walton et al. (1998) has the form:

$$SST_{sat} = a + bT_4 + c\ (T_4 - T_5)\ SST_{guess} + d(T_4 - T_5)\ [sec(\theta) - 1] \quad (3)$$

Where SST_{sat} is the satellite-derived SST estimate, T_4 and T_5 are brightness temperatures in the 10.8 and 11.4 μm bands of AVHRR channel 4 and channel 5, respectively, SST_{guess} is a first-guess SST value, and θ is the satellite zenith angle. Coefficients *a*, *b*, *c*, and *d* are estimated from regression analyses using *in situ* and satellite calibrated measurements. The monthly SST data, with 4 km of spatial resolution with standard calibration from the data provider were derived from the AVHRR sensor and obtained from Coastwatch NOAA available from http://coastwatch.pfeg.noaa.gov.

Meridional Wind Stress (τy)

Spaceborne wind scatterometry has become an increasingly important tool in the effort to monitor the Earth climate, forecast weather, and study ocean–atmosphere interaction. As with all scatterometers, Seawinds/QuickSCAT from NASA and ASCAT/MetOp from EUMETSAT – European Space Agency (ESA) will obtain an estimate of the wind vector by measuring the ocean-surface radar backscatter cross section at multiple azimuth angles (Figure 7).

Data from January 2003 to October 2009 of τy was obtained from SeaWinds

Scatterometer/QuickSCAT, whereas wind-based forcing from November 2009 to December 2012 was obtained from Advanced Scatterometer/METOP and both τy series were obtained from the CoastWatch database (http://coastwatch.pfeg.noaa.gov).

Figure 7. Overview of wind retrieval algorithm

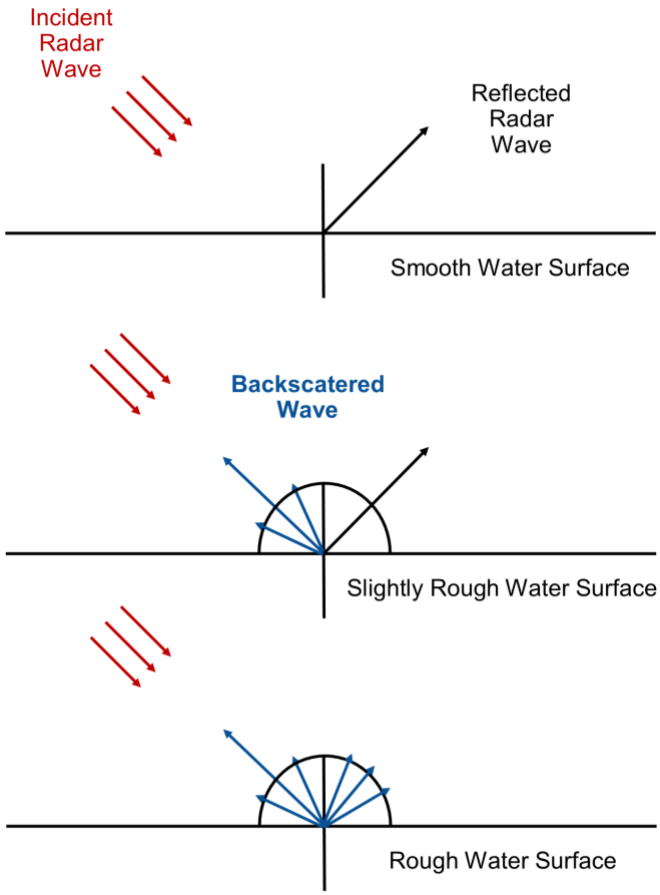

Source: the author (Adapted from Office of Satellite and Products Operations – NOAA)

The geophysical-model function, which relates windspeed and direction to backscatter cross section, is then numerically inverted to infer the near-surface winds. The raw radar data has two unknowns, namely wind speed and wind direction, so, if more than two backscatter measurements (waves) are available then these two unknowns may be estimated as the objective function for determining wind vector solutions, defined by the following equation:

$$J = \left(Z_{oi} - Z_m(u, X_i)\right)^{2,} \quad (4)$$

Where z = (σ 0) are the transformed backscatter data, Z_{oi} are the backscatter measurements, $Z_m(u, X_i)$ are the model backscatter values corresponding to the measurements.

The local minima of *J* correspond to wind vector solutions. The three independent measurements (before, mid and after beam/wave) sample the azimuth variation to resolve the wind direction.

Zonal Currents (u)

High-resolution ocean surface currents are of great importance for many oceanographic applications. From a practical perspective, they are necessary for monitoring the surface advection of oil spills (e.g., Wahl et al. 1996) or the role of horizontal advection on plankton dynamics (Garçon et al. 2001) for interpreting ocean in situ measurements with respect to meandering fronts or eddies (Morrow et al. 2003) or interpreting the trajectories of migrating sea mammals, birds, or turtles (e.g., Girard et al. 2006). Global coverage of the surface circulation is relatively new. Global surface geostrophic currents have been determined from satellite altimetry data over the last 10– 15 years, excluding the tropical band where the Coriolis force approaches zero (e.g., Ducet et al. 2000).

The zonal current (u) product is a direct computation of global surface currents using satellite Sea Surface Height (SSH), wind, and SST. Currents are calculated using a quasi-steady geostrophic model together with an eddy viscosity based wind-driven geostrophic component and a thermal wind adjustment. The model calculates a surface current averaged over the top 30m of the upper ocean. And this dataset is calibrated using *in situ* measurements from drift buoys, Acoustic Doppler Current Profilers (ADCP) and Moored Current Meters (MCMs). This formulation also combines geostrophic, Ekman and Stommel shear dynamics, and a complementary term from the surface buoyancy gradient. Data from January 2003 to December 2012 was used on a 1/3° grid were obtained from the Ocean Surface Current Analyses OSCAR/NOAA archives resolution (http://www.oscar.noaa.gov).

River Discharge (Q)

The Amazon River gauge station Óbidos is generally used to quantify the total discharge of the Amazon Basin into Atlantic Ocean. A ten-year time series of monthly Amazon River discharge at the Óbidos gauge station (1°55'9.01" S, 55°30'47.02" W) (yellow dot at Figure 13) obtained from the National Water Agency (ANA) database, Brazilian Ministry of Environment (MMA).

Rainfall

Rainfall data rely on passive and active measurements to measure the properties of precipitation. Active radars like Dual-Frequency Precipitation Radar (DPR) transmit and receive signals reflected to the radar. The signal returned to the radar receiver (called radar reflectivity) provides a measure of the size and number of rain/snow drops at multiple vertical layers in the cloud (Figure 8).

Figure 8. TRMM fundamentals for active and passive measurements

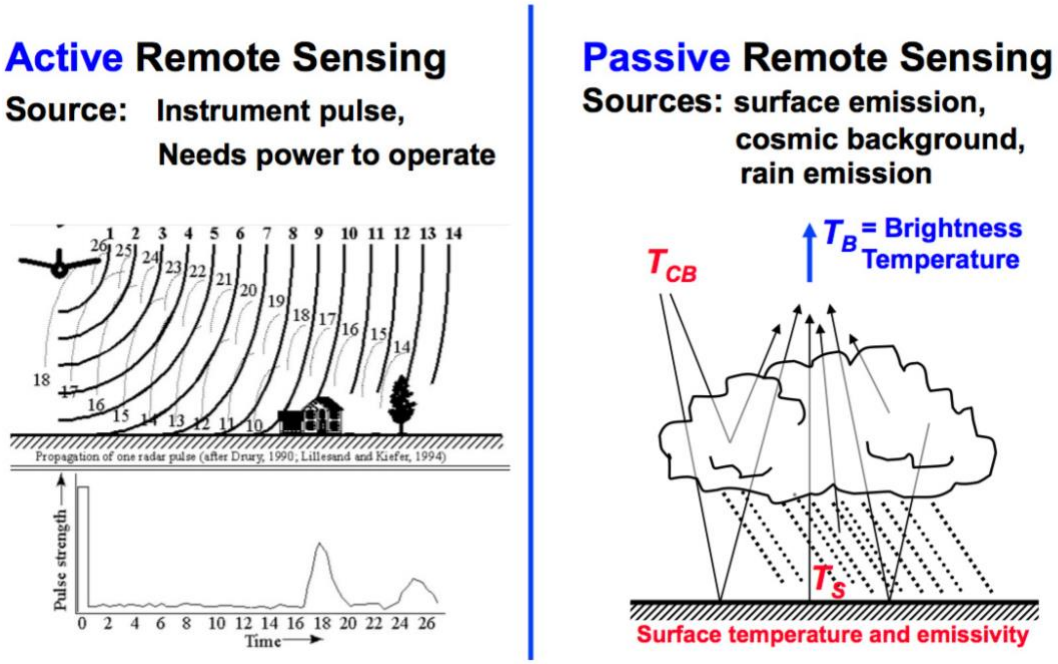

Source: the author (adapted from Precipitation Measurement Missions – NASA)

On the other hand, passive precipitation radiometers measure natural thermal radiation (called brightness temperatures) from the complete observational scene including snow, rain, clouds, and the Earth's surface (Figure 8). The combined use of coincident active and passive microwave sensor data provides complementary information about the macro and microphysical processes of precipitating clouds which can be used to reduce uncertainties in combined radar/radiometer retrieval algorithms. In simple terms, the combined algorithms use the radiometer signal as a constraint on the attenuation seen by the radar. The algorithm performance is verified against Ground Validation (GV) data. In the algorithm development stage, GV data may be used to improve the science of the retrievals. Rainfall data over the Amazon River Basin (10°–20° S, 80°–50° W) during 2003-2012 were obtained from the Tropical Rainfall Measuring Mission – TRMM (http://trmm.gsfc.nasa.gov).

ENSO

The El Niño Modoki has distinct signatures in SST anomaly and its evolution as compared the canonical El Niño. El Niño (La Niña) Modoki events are characterised with warm (cold) SST anomaly in the central Pacific (Figure 9, A light red area) flanked on the east and west by cooler (warmer) SST anomalies (Figure 9, B and C light blue areas). Whereas canonical El Niño (La Niña) (Figure 9 gray shaded area) refers to anomalous warming (cooling) in the eastern equatorial Pacific Ocean often accompanied by cooler (warmer) SST anomaly in the western Pacific.

Figure 9. SST anomalies sites for canonical (gray shaded area) and Modoki (A light red area, B and C light blue areas) El Niños/La Niñas.

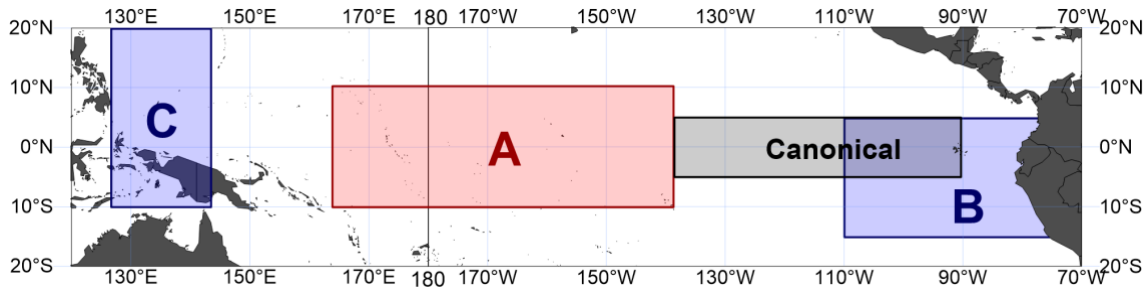

Source: the author

The global teleconnections of El Niño Modoki are also different from that of canonical El Niño. They are opposite to one another, or weaker/stronger or asymmetric, depending on the region and the season of teleconnection. The canonical El Niño is calculated at the El Niño 3 area, by subtracting the long-term mean. A quarter is characterized as under canonical El Niño influence if the SST anomaly in the canonical region is below (above) or equal $0.7\sigma_{canonical}$ $(-0.7\sigma_{canonical})$, where $\sigma_{canonical}$ is the standard deviation of SST anomalies in the canonical region.

A quarter is characterized under influence of an El Niño Modoki if the EMI is above (below) or equal to $0.7\sigma_m(-0.7\sigma_m)$ and the area A is above (below) $0.7\sigma_m(-0.7\sigma_m)$, were σ_m is the standard deviation of EMI series and σ_a is the standard deviation of SST anomaly series for the area A. The El Niño Modoki Index (EMI) is calculated as follow:

$$EMI = |SST|_A - 0.5|SST|_B - 0.5|SST|_C \quad (5)$$

Where, $|SST|$ is the mean SST anomalies in indicated areas (A, B and C).

Atlantic Climate indices

As the Pacific Ocean, the Atlantic Ocean presents SST anomalies representing his inherent climate indices. The Atlantic Meridional Mode (AMM) is the dominant source of coupled ocean-atmosphere variability in the Atlantic (Figure 10, grey shaded area). The AMM affects rainfall in Northeast Brazil and tropical cyclone development in the North Atlantic. During a positive phase of the AMM, the Atlantic Intertropical Convergence Zone (ITCZ) is displaced northward, causing drought in Northeast Brazil. Warmer than normal sea surface temperatures (SSTs) and weaker than normal vertical wind shear during positive phases of the AMM tend to enhance tropical cyclone development in the Atlantic. The conditions are opposite for the negative phase of the AMM. The AMM exhibits strong variability on interannual to decadal timescales. A key component of the AMM is a positive feedback between the ocean and atmosphere. During a positive phase of the AMM, SSTs become warmer than normal in the tropical North Atlantic and cooler than normal in the tropical South Atlantic. Surface air pressure responds to the SST anomalies, becoming higher than normal over the anomalously cold SSTs and lower than normal over anomalously warm SSTs. Anomalous surface winds flow from the cold to the warm hemisphere, strengthening the mean southeasterly trade winds in the South Atlantic and weakening the northeasterly trade winds in the North Atlantic. The surface wind anomalies thus provide a positive feedback onto the initial SST anomalies by forcing changes in wind-induced evaporative cooling of the ocean.

Figure 10. SST anomalies sites for AMM (gray shaded area), TNA (orange shaded area), NTA (blue shaded area), CTA (red shaded area) and TSA (green shaded area).

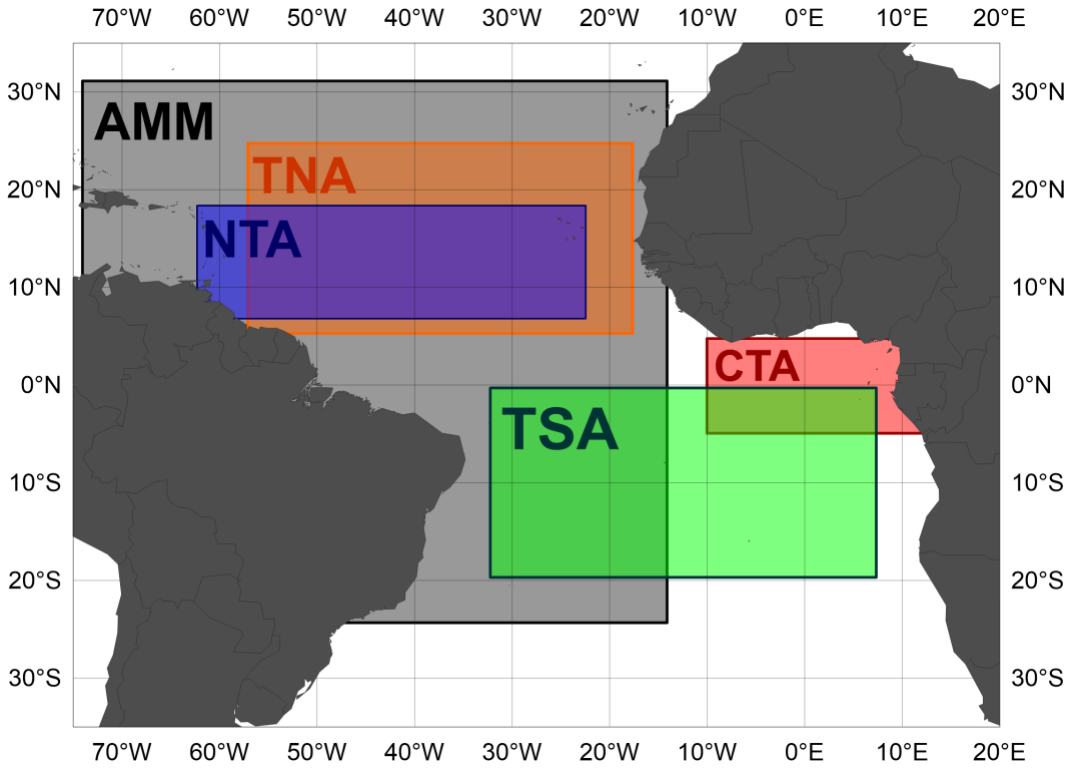

Source: the author

The North Tropical Atlantic (NTA) SST index is an indicator of the surface temperatures in a broad swath of the tropical North Atlantic Ocean. It is calculated with SSTs in the box 40°W - 20°W, 5°N - 20°N (Figure 10, blue shaded area). The NTA index is defined in a paper by Chang et al. (1997), where they were associated with a potential decadal 'dipole' mode of coupled variability in the tropical Atlantic. The index is calculated using the Reynolds Optimal Interporlation (OI) v2 SST analysis, made available by NOAA, and is updated weekly. The anomaly is calculated relative to a monthly climatological seasonal cycle based on the years 1982 to 2005. The monthly climatology is linearly interpolated to determine weekly anomalies. The OI analysis is produced weekly on a one-degree grid. Before the analysis is computed, the satellite SST data is adjusted for biases using the method of Reynolds (1988) and Reynolds and Marsico (1993). A description of the OI analysis can be found in Reynolds and Smith (1994).

The Tropical Northern Atlantic Index (TNA) SST anomaly index is an indicator of the surface temperatures in the eastern tropical North Atlantic Ocean. It is calculated with SSTs in the box 55°W - 15°W, 5°N - 25°N (Figure 10, orange shaded area). The index is also calculated using the Reynolds OIv2 SST analysis, made available through by NOAA/ESRL. The anomaly is calculated relative to a monthly climatological seasonal cycle based on the years 1982-2005.

The monthly climatology is linearly interpolated to determine weekly anomalies. Spatial averaging of the gridded analysis is weighted by surface area.

Tropical Southern Atlantic Index (TSA) SST anomaly index is an indicator of the surface temperatures in the Gulf of Guinea, the eastern tropical South Atlantic Ocean. It is calculated with SSTs in the box 30° W - 10° E, 20° S - 0° (Figure 10, green shaded area). As the the last two indices, the TSA is also, calculated using the Reynolds OIv2 SST analysis, made available by NOAA/ESRL. The anomaly is calculated relative to a monthly climatological seasonal cycle based on the years 1982 to 2005. The monthly climatology is linearly interpolated to determine weekly anomalies. Spatial averaging of the gridded analysis was weighted by surface area (Tokinaga and Xie, 2011). Both TNA and TSA indices were defined in a paper by Enfield et al. (1999), where dipolar patterns across the tropical Atlantic were found with a periodicity of 8-12 years for the boreal winter-spring, and 2.3 years for the boreal summer-fall.

Atlantic Cold Tongue (CTA) SST montly anomalies are averaged over 10° W – 15° E and 5° N – 5° S (Figure 10, red shaded area) based on the years 1970 to 2015.

3.2 Reanalysis Data

Ocean ReAnalysis System 4 (ORAS4)

Ocean reanalyses are historical reconstructions of the ocean climate, based on the objective synthesis of the information provided by ocean models, atmospheric forcing fluxes and ocean observations, combined via data assimilation methods and are also referred to as ocean syntheses. The designation reanalysis is not so intuitive, but mirrors the equivalent designation used for the more consolidated activities in the historical reconstruction of the atmosphere (Balmaseda et al., 2008). Ocean reanalysis is now an established activity in several research and operational centres. Ocean reanalyses are revisited every so often, and new ‘vintages’ of reanalyses are produced at intervals of about five years, when improvements in ocean models, data assimilation methods, forcing fluxes or ocean observations are available.

The Ocean ReAnalysis System 4 (ORAS4) has been implemented to replace the previous system ORAS3 (Balmaseda et al., 2008). The ORAS4 reanalysis ORAS4 uses version 3.0 of the NEMO ocean model (Madec, 2008) in the horizontal discretization. The configuration corresponds to a horizontal resolution of 1° in the Extratropics and refined meridional resolution in the Tropics with a minimum value of 0.3° directly at the Equator. The ORAS4 has 42 vertical levels, 18 of which are in the upper 200 m. The first level has a 10m thickness. The vertical discretization scheme uses partial steps to have better representation of the flow over steep

topography. A weak (20-year time-scale) relaxation to temperature and salinity climatological values from the World Ocean Atlas 2005 (WOA05) (Antonov et al., 2006; Locarnini et al., 2006) is applied throughout the water column.

The analysis cycle in ORAS4 is 10 days. Every 10 days, the Nucleus for European Modelling of the Ocean alias NEMO model is integrated forward forced by daily surface fluxes, relaxed to SST and bias corrected to produce the first guess and background trajectory. The model equivalent of each available observation is calculated to construct the vectors, and a quality control (QC) of the performed observations.

Global Precipitation Climatology Centre version 7 (GPCC)

Gridded data sets of long-term mean (climatological) precipitation help to quantify the mean characteristics of the global water and energy cycle and its changes in the context of climate change. In December 2011, the Global Precipitation Climatology Centre (GPCC) released the previous version of its precipitation climatology (Meyer-Christoffer et al., 2011), based on climatological normals of about 67,200 stations (Figure 10) and came up with a (at that time) best estimate for the mean precipitation over the global land surface of 786 mm per year (Schneider et al., 2014). Since then, the GPCC has further improved and enhanced its database by adding, besides an additional level of quality-control, more precipitation data, so that the most recent release of the precipitation climatology dataset (Meyer-Christoffer et al., 2015) is based on about 75,100 stations with climatological normals in the GPCC database.

Updates for many countries have been integrated and a significant amount of data has been added for Brazil, Colombia, Mexico and some previously data sparse regions (i.e., for Ethiopia, Libya, Somalia, the Lake Chad region, Cambodia, and Kyrgyzstan). The database has also been significantly enhanced for Indonesia and for other island/atoll regions (Bahamas, Caribbean Islands, French Polynesia, Mauritius, Reunion, Seychelles and Vanuatu). Figure 11 shows Spatial distribution of monthly *in-situ* stations.

Figure 11. GPCC spatial distribution of *in-situ* stations.

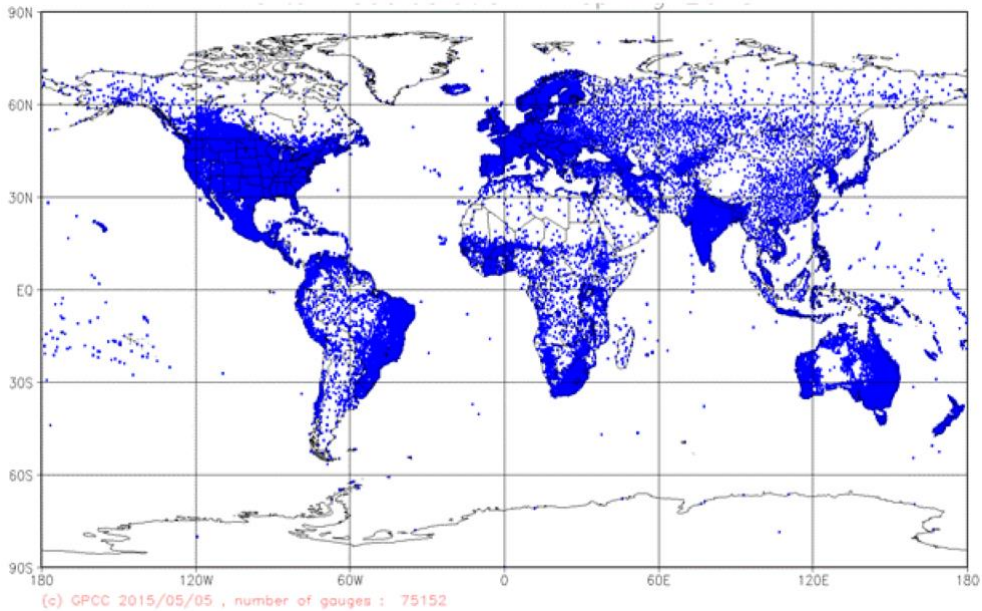

Source: GPCC

ERA-Interim

The evolution of the global land surface state (moisture content and/or temperature) of the different components, soil, vegetation, snow, is of great interest to understand climate-change impact in recent years. The numerical weather prediction system ERA-Interim is a global land-surface dataset covering recent decades, is the result of a single 32-year simulation of atmospheric reanalysis and precipitation adjustments based on Global Precipitation Climate Project (GPCP). ERA-Interim preserves closure of the water balance and includes several parameterisations improvements in the land surface scheme with respect to the original ERA-Interim dataset, which makes it suitable for climate studies involving land water resources.

The quality of ERA-Interim includes several parameterisations improvements introduced in recent years, was assessed in comparison to site measurements, satellite-based products and other reanalyses, and it is supporting the study of climate trends. In this study, we used data for 46 years of monthly zonal, meridional, and vertical components of winds from ERA-Interim reanalysis, produced by the European Centre for Medium-Range Weather Forecasts (ECMWF), and available at http://www.ecmwf.int/.

3.3 Analysis Tools

Climatology is commonly known as the study of our climate, yet the term encompasses many other important definitions. Climatology is defined as the long-term average of a given variable over time periods of 20-30 years. Climatology is frequently employed in the

atmospheric sciences, and may be computed for a variety of time ranges. A monthly climatology, will produce a mean value for each month, over a specified time range (time-series). Anomalies are created by subtracting climatological values from observed data:

$$Anomaly = X_{obs} - X_{climatology} \quad (6)$$

The correlation is defined as the measure of linear association between two variables. A single value, commonly referred to as the correlation coefficient (r^2), is often needed to describe this association estimating correlations by negative (-1) or positive (1). The climatology composites were processed with the implementation in the SeaDAS 7.4 software package. The statistical and EOF analysis were perfomed with MATLAB R2016a software.

Empirical Orthogonal Function (EOF)

In climate studies, Empirical Orthogonal Function (EOF) is often used to identify spatial modes (i.e., patterns) of variability and how they change with time (e.g., Atlantic Ocean Dipole). In statistics, EOF analysis is known as Principal Component Analysis (PCA). As such, EOF analysis is classified as a multivariate statistical technique. However, there is no *a priori* hypothesis based on some probability distribution and, hence, no statistical test. EOF analysis is not based on physical principles. Rather, a field is partitioned into mathematically orthogonal (independent) modes which are interpreted as atmospheric and oceanographic modes or patterns.

EOF is a technique that has the purpose of efficiently producing a large group of variances of the original data in new variances. This method is used to extract intrinsic characteristics of the data series that vary temporally and spatially, transforming several dimensions into a few (Wilks, 1995). The EOF decomposes a multivariate data set into modes, which represent variability in time and space from the original data based on multivariate analysis (Wilks, 1995). The EOF generates as results where, for the first mode (EOF1) the first main component (PC1) is estimated, which is represented by the maximum fraction of the variance related to this mode (EOF1). In the second mode (EOF2) is unrelated to the EOF1, represented by the largest variance of the remaining data set. In the third mode (EOF3), similarly, there is not related to the previous mode (EOF2). The principal components (PC1, PC2, PC3, …) are associated to the temporal patterns for each mode (EOF1, EOF2, EOF3, …), representing the evolution of spatial modes in time (Wilks, 1995).

To perform the EOF it is necessary to transform the data matrix into three dimensions, resulting in a space vs time matrix, considering *N* maps for each time $t = 1 \dots N$, where each map have position measurements $m = 1 \dots M$. Each spatial matrix *M* have latitudes and longitudes as position measurements, making a tri-dimensional matrix with time *N*, f = *[latitudes longitudes time]*. Combinatorial analysis of matrix f is needed to generate the *F* matrix with two dimensions *F* = *M* x *N* as follow:

$$F = \begin{bmatrix} \overset{time}{\longrightarrow} & & & \\ F_1(1) & F_1(2) & \dots & F_1(N) \\ F_2(1) & F_2(2) & \dots & F_2(N) \\ \dots & \dots & & \dots \\ F_M(1) & F_M(2) & \cdots & F_M(N) \end{bmatrix} \downarrow position \tag{7}$$

where *M* rows represents the position *m*, and *N* columns represent time *t*.

Typically, the EOF is found by computing the eigenvalues and eigenvectors of a spatially weighted anomaly covariance matrix of a field. The derived eigenvalues provide a measure of the percent variance explained by each mode. The Singular Value Decomposition (SVD), calculates the temporal amplitudes, the spatial oscillation modes and their corresponding eigenvalues (Yi and Venegas, 1999). The SVD is based on the concept that. Any *F* squared matrix *M* x *N* could be described by three matrix product, one matrix *U M* x *N*, one diagonal matrix *S M* x *N* and one transposed matrix (*V*') of the matrix *V M* x *N*. The SVD as follow:

$$F = U * S * V' \tag{8}$$

Unfortunately, the eigenvalues are not necessarily distinct due to sampling issues. North et al. 1982 provide a 'rule' for determining if an eigenvalue is distinct from its nearest neighbour. Typically, in atmospheric and oceanographic processes most of the variance is contained within the first few modes. The time series of each mode (PCs) are determined by projecting the derived eigenvectors onto the spatially weighted anomalies. This will result in the amplitude of each mode over the period of record.

By construction, the EOF patterns and the principal components are independent. Two factors inhibit physical interpretation of EOFs: (1) the orthogonality constraint and (2) the derived patterns may be domain dependent. Physical systems are not necessarily orthogonal and if the patterns depend on the region used they may not exist if the domain changes. Still,

even with these short comings, classical EOF analysis has proved to be useful (Yi and Venegas, 1999)).

3.4 Camadas Finas V survey *in situ a*CDOM measurements

CDOM samples were collected from September 18th to 24th of 2014 during oceanographic survey *Camadas Finas V* with an orientation towards the measurements of apparent optical properties (AOP) and inherent optical properties (IOP) of waters influenced by the Amazon River plume. This ship campaign was planned as the result of collaboration between the UFPE (*Universidade Federal de Pernambuco*) in Recife (Brazil), UVic (University of Victoria) in Victoria (Canada) and DHN (*Diretoria de Hidrografia e Navegação – Marinha do Brasil*) in Niterói (Brazil) The station locations of this cruise are shown in Figure 31. The sampling was performed in two distinct zones: (1) Open Ocean (stations made after the shelf break) and (2) Shelf zone (stations made above the shelf that are strongly influenced by the Amazon River). These different zones were delimited according to the presumed (different) inputs of CDOM. A well- established correlation between an optically active component and a physical parameter (i.e. salinity), could therefore be used as an indicator of hydrography in those highly dynamic regions. Salinity measurements was acquired with a SeaBird 911+ CTD probe. CDOM water samples were collected using 10 l Niskin bottles from the CTD carrousel at a minimum of two depths (surface and maximum *Chl*). For each depth, triplets were collected in 1 l Nalgene bottles and first filtered in Whatman GF/F of 0.7 μm of porosity membranes to separate the pigments. The leftover water was filtered in 0.2 μm acetate Pall membranes and stored in 100 ml amber bottles in a dark environment at 4 °C. The absorption measurements were performed 4 hours after the filtration. The filtrates of the 0.2 μm membrane was used for the CDOM absorption (*a*CDOM) measurements, which were performed directly onboard the vessel. These *a*CDOM values were obtained using an Ocean Optics USB4000 Spectrometer, following post-processing protocols as described by Pegau et al. (2003), in accordance with guidelines following storage and analysis as described by Loos and Costa (2010).

4 RESULTS

In this chapter, this work results are presented in three sessions (4.1, 4.2 and 4.3) that show the scientific articles produced throughout the present study.

4.1 Pacific ENSO change enhances chlorophyll-a concentration in the Amazon River plume

The first scientific paper was submitted to *Nature Scientific Reports* periodic. This manuscript analyses chlorophyll-*a* (*Chl*) concentration derived from the MODIS/Aqua sensor in a 10-year time series (January 2003 - December 2012). The main objective is to characterize the *Chl* concentration seasonal and interannual variability over the Amazon plume related to local and remote physical processes, as El Niño Southern Oscillation (ENSO) in the Pacific Ocean. Also, to investigate positive interannual anomalies of *Chl* related to canonical El Niño and El Niño Modoki. This manuscript is described below:

Abstract

Ten-year MODIS/Aqua dataset was used to determine seasonal and interannual chlorophyll-*a* (*Chl*) variability in the Western Tropical North Atlantic (WTNA) under influence of the Amazon River discharge (Q). Changes in El Niño Southern Oscillation (ENSO) in recent decades points toward an increasing frequency of El Niño Modoki (EM) over the El Niño canonical (EC) mode. EM events remotely induce above normal rainfall over the Amazonian basin, which increases Q and nutrient supply to the WTNA. Results showed *Chl* interannual positive anomalies in 2003, 2004, 2006, 2009 and 2012. Significant correlations between *Chl* and Q, sea surface temperature (SST), meridional wind stress (ty) and zonal current (u) occur on a seasonal scale. The transition to Modoki mode mainly in 2006, 2009 and 2012, stands out as a precursor for positive rainfall, Q and high *Chl* anomalies in the interannual scale. Indicating that, this interannual variability not only intensified the *Chl* concentration on seasonal cycle, but also throughout the whole year. Our study suggests that, the interannual positive anomalies of *Chl* concentration over the WTNA are dependent of rainfall/Q events forced mainly by the EM mode.

Keywords: Chlorophyll-*a*. Amazon plume. El Niño.

Introduction

The high nutrient input from the continents to the oceans is of fundamental importance for the maintenance of aquatic biota and the determination of the preferential pathways of biogeochemical processes governing the composition of coastal and oceanic waters and their interaction with the atmosphere (Lefèvre et al., 2013; Araujo et al., 2014; Noriega and Araujo, 2014). Nutrient loads carried by large rivers and discharged into the adjacent oceanic region, for example, increase primary production (PP) and can lead to substantial CO_2 uptake (Körtzinger, 2003; Regnier et al., 2013). Plumes of major rivers are also intense sites of ecological complexity (Hickey et al., 2010) and biogeochemical transformation and they also play an important role in physical processes (McKee et al., 2004). Freshwater inputs may change the stratification and influence the nutrient flux and light regime in the upper mixed layer, thus controlling phytoplankton growth (Smith and DeMaster, 1996).

The Amazon River discharge is responsible for substantial algal blooms that occur on the Amazonian shelf (Milliman and Boyle, 1975; Edmond et al., 1981; DeMaster et al., 1996), confirming his importance for nutrient budget. The Amazon River is by far the largest single source of terrestrial freshwater to the ocean, contributing approximately 30% of the total river discharge to the Atlantic (Wisser et al., 2010). This inflow varies seasonally, reaching a maximum discharge in May and a minimum in November (Geyer and Beardsley, 1995; Dai and Trenberth, 2002).

In addition to the discharge of continental waters from the Amazon River, the Western Tropical North Atlantic (WTNA) has been identified as a particularly high-energy marine system because of the combined action of tidal oscillations, ocean currents and trade winds (Silva et al., 2009). The seasonal variation of the Intertropical Convergence Zone (ITCZ) causes the predominant southeast trade winds in the region from June to November and the northeast trades from December to May and thus the interhemispheric transportation of the Amazon River plume by the North Brazil Current (NBC) (Geyer and Beardsley, 1995). Also, sea surface temperature (SST) in this region is linked to Amazon Basin rainfall and the ITCZ position (Liebmann and Marengo, 2001; Labat, 2004; Servain et al., 2014). During high-discharge periods, the NBC retroflects and ocean currents can transport the freshwater/nutrient supply to a great distance eastward over the WTNA. Satellite images show high chlorophyll-*a* (*Chl*) concentrations and low sea surface salinities far from the river mouth because the Amazon waters are transported eastward by the North Equatorial Counter Current (NECC) in boreal autumn (Johns et al., 1990; Brandt et al., 2006; Reul et al., 2014).

Previous studies have also shown that fluctuations in the tropical Atlantic north-south SST gradient caused by ENSO events have been linked to changes in rainfall over South America (Kossin and Vimont, 2007; Rodrigues et al., 2011). Indeed, recent research emphasizes the existence of noncanonical or "non-traditional" ENSO mode. This noncanonical ENSO is reported in the literature as central Pacific, warm pool, or El Niño Modoki (EM) (Yeh et al., 2009; Kao and Yu, 2009; Kug et al., 2009). El Niño canonical (EC) is characterized by strong anomalous warming in the eastern equatorial Pacific, whereas EM is associated with strong anomalous warm central equatorial Pacific flanked by anomalously cold regions in both west and east. Positive correlations from the central equatorial Pacific SST (EM region) extend to regions of South America, indicating more than normal rainfall compared with eastern equatorial Pacific (EC region) (Ashok et al., 2007) (Figure 12).

Figure 12. Composite for Sea surface temperatures (SST) anomalies for the three largest events of canonical El Niño (1982, 1987, and 1997) and Modoki El Niño (1994, 2002, and 2004) in the Equatorial Pacific and, rainfall over the Amazon basin during these events.

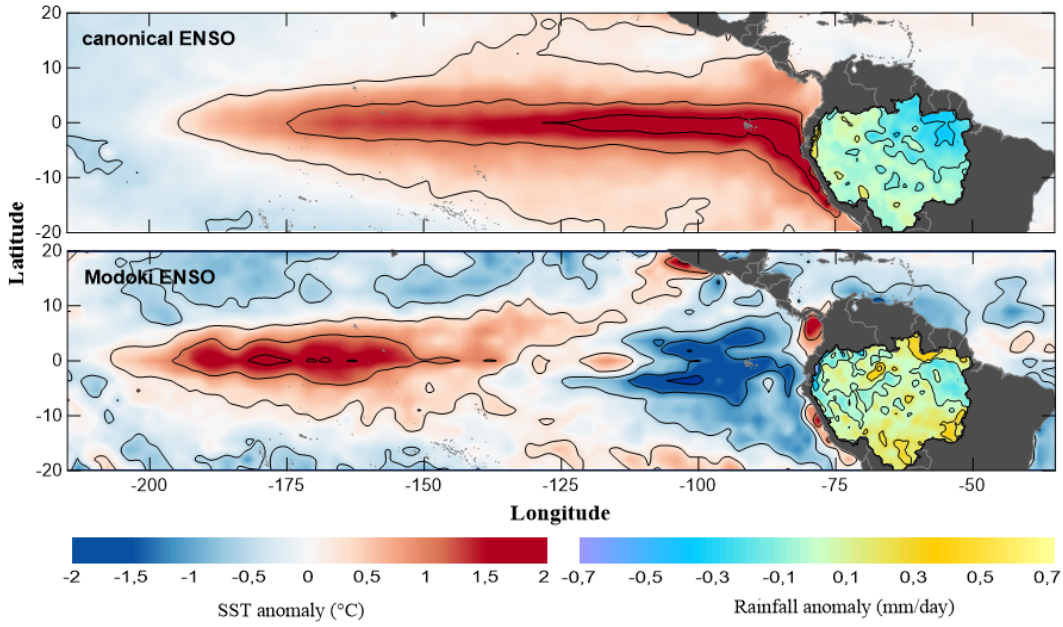

Source: The author

Studies point out that the recent SST warming trends in the western equatorial Pacific appeared to be result of greater frequency and amplitude of EM compared to EC (Ashok et al., 2007; Weng et al., 2007; McPhaden et al., 2011; Wang and Wang, 2014). In this work, we focus on the seasonal and interannual variability of *Chl* over the Amazon River plume retroflection related to local and remote forcing. In particular, we investigate the *Chl* high concentrations in the WTNA waters related to EC and EM events.

Methods

The WTNA region under the influence of the Amazon River plume is shown along with the 200 m isobaths (Figure 13), representing the approximate outer edge of the continental shelf. The study area in this work is located after the North Brazilian Current retroflection (5°-10° N and 45°-50° W). This area is represented by the black square (Figure 12) and corresponds to the offshore ocean region were the well-developed river plume is transported eastward by the NBC retroflection. Within this area, we evaluated a ten-year time series (January 2003 to December 2012) of satellite-derived data regarding *Chl*, sea surface temperature (SST), meridional wind stress (τy), and zonal current velocity (u). The variability of remote forcing during this same period was examined these include river discharge (Q), rainfall over the Amazon River basin and the following ENSO indices: canonical and Modoki.

Figure 13. Monthly mean *Chl* (mg m^{-3}) in log_{10} scale, for August/September climatology (2003 to 2012) under the influence of the Amazon River plume and the study area (Black Square). The black line alongshore represents the 200m isobath that defines the continental shelf boundary.

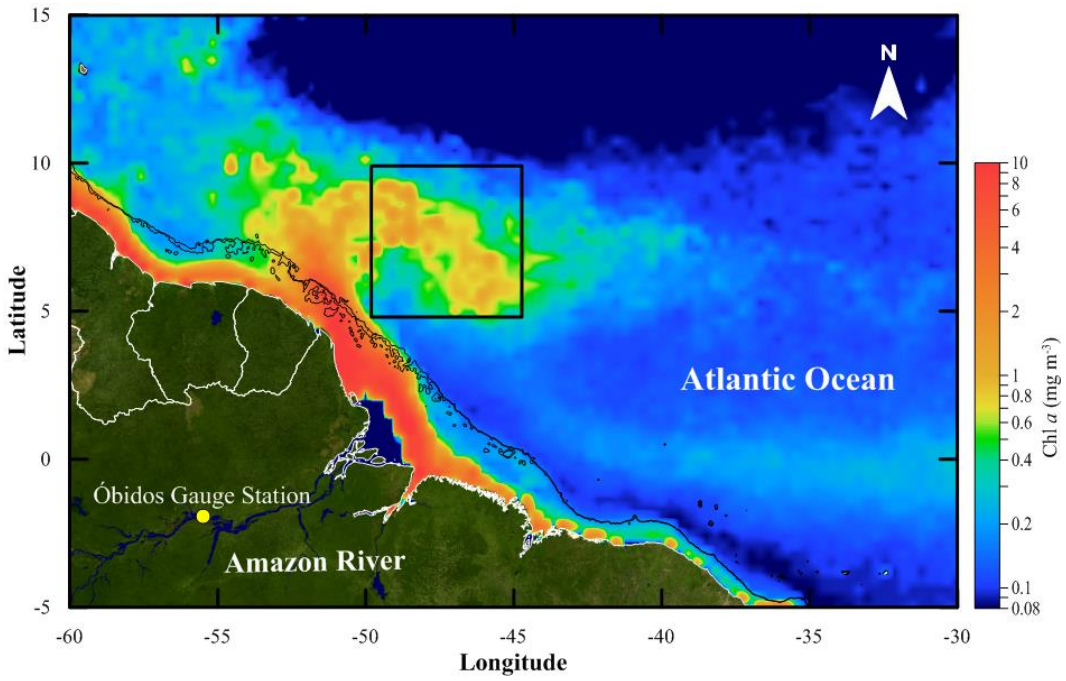

Source: The author

Monthly *Chl* surface data with 4 km spatial resolution were obtained from the MODIS/Aqua sensor processed with standard NASA global coefficients (O'Reilly et al., 1998), available at oceancolor.gsfc.nasa.gov. The SST data were derived from the AVHRR sensor (http://coastwatch.pfeg.noaa.gov). Data from January 2003 to October 2009 of τy was obtained from SeaWinds Scatterometer/QuickSCAT, whereas wind-based forcing from November 2009

to December 2012 was obtained from Advanced Scatterometer/METOP and both τy series were obtained from the CoastWatch database (http://coastwatch.pfeg.noaa.gov).

The zonal current (u) data consists on horizontal velocity that is directly estimated from sea surface height, surface vector wind and sea surface temperature. The formulation combines geostrophic, Ekman and Stommel shear dynamics, and a complementary term from the surface buoyancy gradient. Data are on a 1/3° grid were obtained from the Ocean Surface Current Analyses OSCAR/NOAA archives resolution (http://www.oscar.noaa.gov). A ten-year time series of monthly Amazon River discharge at the Óbidos gauge station (1°55'9.01" S, 55°30'47.02" W) (Figure 13, yellow dot) was obtained from the National Water Agency (ANA) database, Brazilian Ministry of Environment (http://www2.ana.gov.br).

The Amazon River station Óbidos is generally used to quantify the total discharge of the Amazon Basin into Atlantic Ocean. Rainfall data over the Amazon River Basin (10°–20° S, 80°–50° W) during 2003-2012 were obtained from the Tropical Rainfall Measuring Mission – TRMM (http://trmm.gsfc.nasa.gov). For this study, data from EMI (El Niño Modoki Index) was used to characterize the El Niño Modoki (EM), and El Niño 3 index for the canonical El Niño (EC), both data sets of ENSO indexes were obtained at http://www.cpc.ncep.noaa.gov.

Satellite *Chl* data were averaged over the 120 monthly composites to produce monthly ten-year time series. These *Chl* charts were, in turn, used to compute the climatology and anomalies of space-averaged *Chl* values in the study area. The anomalies are defined as the differences between the month values and the climatological monthly average for the ten-years time series. No significant long-term trend was detected over the period 2003-2012 on *Chl* and any other physical parameter. Spearman Correlation coefficients (r^2) between *Chl*, local (SST, τy, u) and remote forcing (Q, rainfall) time series were calculated.

Chl mapping was measured in a logarithmic base-10 scale. *Chl* concentrations range from hundredths of mg m^{-3} to tens of mg m^{-3}, representing a range of more than 3 orders of magnitude. A logarithmic base-10 scale plot reveals complex structures throughout the oceans in both nearshore and offshore waters.

Results

Monthly climatology (Figure 14) from Jan/2003 to Dec/2012, for *Chl*, river discharge (Q), Sea Surface Temperature (SST), meridional wind stress (τy) and zonal current (u) in the study area and rainfall over the Amazon basin exhibit well-marked seasonal cycles.

In the first half of the year, *Chl* exhibit average values of 0.16 mg m^{-3}, with low

concentration in March, 0.10 mg m^{-3}, and high in June, 0.33 mg m^{-3} (Figure 14a). In this period, Q increases from 1.43 x 10^5 in January to 2.53 x 10^5 m^3 s^{-1} in May, decreasing in June, 2.5 x 10^5 m^3 s^{-1} (Figure 14b). SST average value is about 27.1 °C, with low temperature of 26.7 °C in February/March (Figure 14c). τy values range from -0.05 in February to -0.02 N m^{-2} in June (Fig. 3d), u varies from positive to negative values, ranging from -0.10 in January to 0.05 m s^{-1} in March/April, decreasing to -0.02 m s^{-1} in May/June (Figure 14e). Rainfall presents values from 229.96 mm in February to 285 mm in March, decreasing to 207.73 mm in June (Figure 14f).

In contrast to the earlier season, in the second half of the year, *Chl* increases from 0.54 mg m^{-3} in July to 0.57 mg m^{-3} in August, and start do decrease in September, reaching 0.12 mg m^{-3} in December (Figure 14a). Q decreases from 2.32 x 10^5 m^3 s^{-1} in July to 9.49 x 10^4 m^3 s^{-1} in October/November, with a minor increase in December, 1.13 x 10^5 m^3 s^{-1} (Figure 14b). 28.7 °C is the SST in July, increasing to 30 °C in September. After this period, the SST starts to reduce, reaching 27.8 °C in December (Figure 14c). At the second half of the year, τy exhibit positive values from July to September, near 0.02 N m^{-2}. In December, this value decreases to -0.02 N m^{-2} (Figure 14d). u flow remains positive all over this season, with a maximum value of 0.22 m s^{-1} in August, after this month, decreasing to 0.06 m s-1 in December (Figure 14e). Rainfall presents lower values in August/September (~136 mm), increasing from October (174.6 mm) to the maximum of 225.56 mm in December (Figure 14f).

Figure 14. Ten-year time series climatology of (a) *Chl*, (b) Q, (c) SST, (d) τy, (e) u and (f) rainfall. The error bars represent the standard deviations.

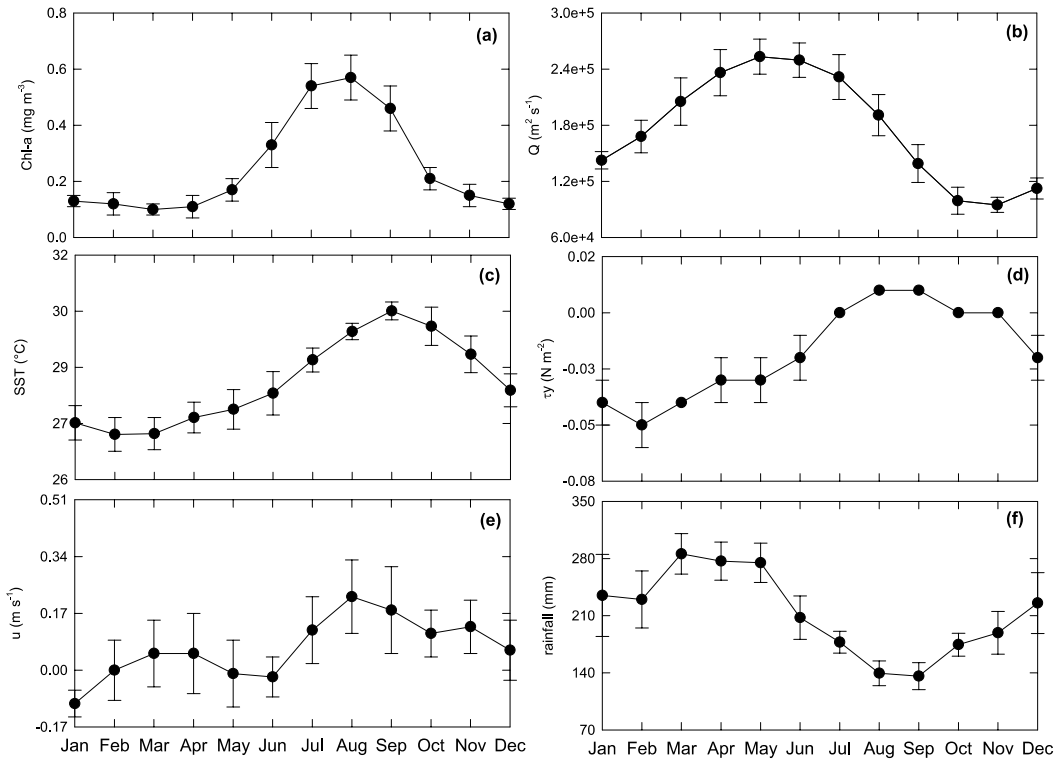

Source: the author

Climatology maps of *Chl* concentration (Figure 15) shows two main dispersion patterns related to the Amazon River plume: In the first period, from December to Mar, *Chl* remains confined to the coast as the plume flows towards northwest above the shelf. *Chl* varies from 0.6 to 10 mg m^{-3} near the coast and increases beyond the continental shelf with values varying from 0.4 to 8 mg m^{-3} in April/May. In the second period, from June to November, *Chl* concentration spreads eastward with values from 0.4 to 8 mg m^{-3} in August/September. From October to November, there is a *Chl* reduction in the region, values of 0.1 to 0.6 mg m^{-3}, while the plume eastward branch can still be noted.

Figure 15. Climatology from 2003 to 2012 of the *Chl* (mg m^{-3}) distribution in the WTNA under the influence of the Amazon River plume.

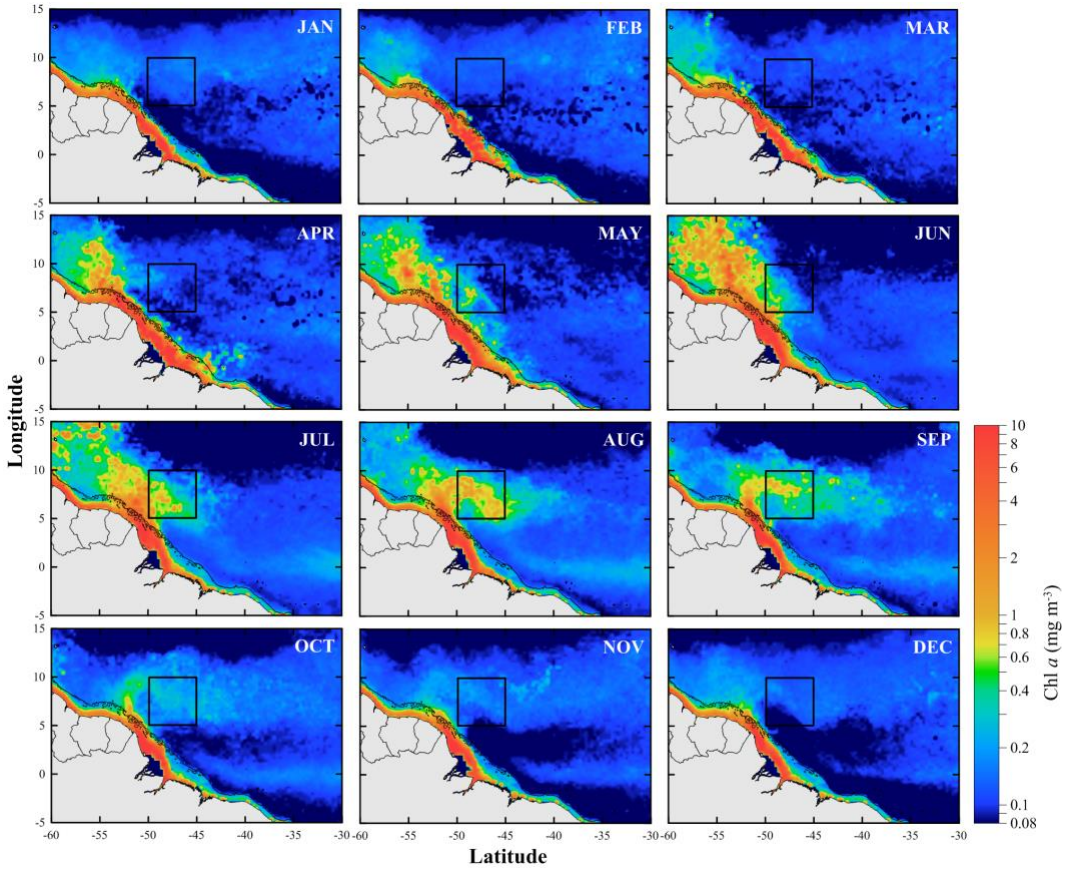

Source: the author

Following this description, the ten-year time series of the factors that contribute to the seasonal variability of *Chl*, where calculated by the Spearman correlation (r^2) with his current degree of freedom (dof) on the Table 1. Analysis showed positive correlations between *Chl* and Q ($r^2 = 0.60$; $\alpha = 0.05$; $p < 0.05$), SST ($r^2 = 0.48$; $\alpha = 0.05$; $p < 0.05$), τy ($r^2 = 0.53$; $\alpha = 0.05$; $p < 0.05$), u ($r^2 = 0.40$; $\alpha = 0.05$; $p < 0.05$), rainfall ($r^2 = 0.50$; $\alpha = 0.05$; $p < 0.05$), and between Q and rainfall ($r^2 = 0.85$; $\alpha = 0.05$; $p < 0.05$).

Table 1. Correlation coefficients (r^2) between *Chl*, Q, SST, τy, u, and rainfall.

	r^2	**lag (months)**	**n**	**α**	**P**	**dof**
Q/*Chl*	0.60	2	120	0.05	< 0.05	99
SST/*Chl*	0.48	0				
τy/*Chl*	0.53	0				
u/*Chl*	0.40	0				
rainfall/*Chl*	0.50	4				
rainfall/Q	0.85	2				

Source: the author

Chl ten-year time series (Figure 16a) presents a mean of 0.25 mg m^{-3}, maximum of 1.26 mg m^{-3} and minimum of 0.09 mg m^{-3}. At interannual timescales the high *Chl* concentrations were identified in 2003 (0.91 mg m^{-3}), 2004 (1.06 mg m^{-3}), 2006 (1.03 mg m^{-3}), 2009 (1.26 mg m^{-3}) and 2012 (1.03 mg m^{-3}). Interannual *Chl* variability is identified by the positive anomalies in Figure 16b. The 2005, 2007, 2008, 2010 and 2011 years show *Chl* low concentrations in the second half of the year, although these values do not exceed 0.5 mg m^{-3} (Figure 16b).

Figure 16. *Chl* concentration for the ten-year time series (a), *Chl* anomalies (b). Calculated values were averaged over the study area.

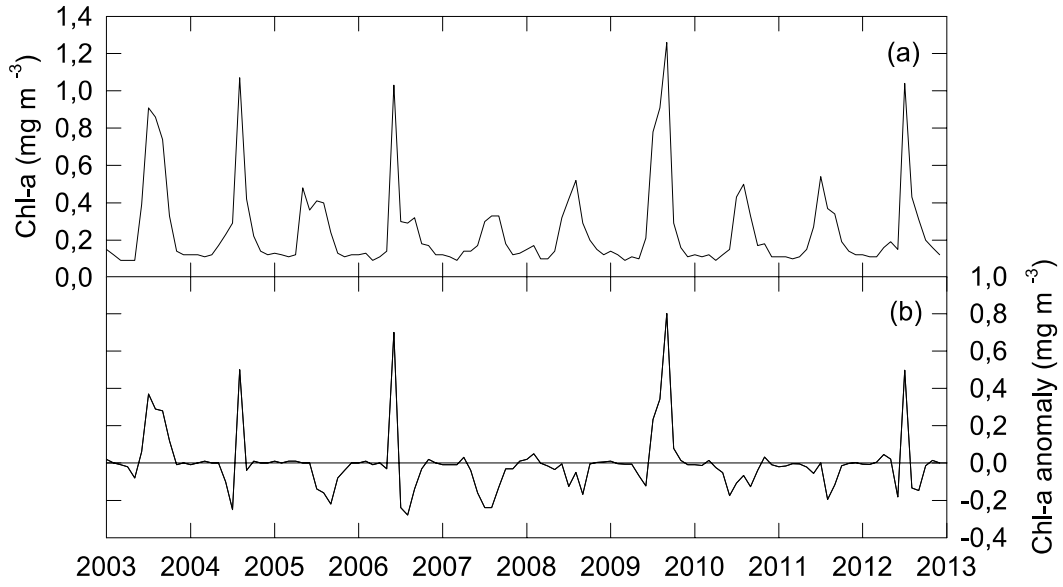

Source: the author

Spatial distributions of *Chl* for August and September (from 2003 to 2012) (Figure 17), which is the period where the Amazon River plume retroflection in its mature phase, indicates higher concentrations during 2003, 2004, 2006, 2009 and 2012, when the maximum values of 8 mg m^{-3} were present in the study area. Among the years of higher *Chl* values, 2003 and 2004 showed similar behaviours, with *Chl* being well distributed in the study area and reaching concentrations of 6-7 mg m^{-3}. In 2009, the *Chl* map showed a greater area of coverage, with high values in the study area (8 mg m^{-3}).

Similar *Chl* distributions were observed during 2006 and 2012, although the maximum value of 6 mg m^{-3} appears only sporadically in the study area and it is surrounded by values of approximately 0.2 to 2 mg m^{-3}. Although 2005, 2007, 2008, 2010 and 2011 maps also show a well-retroflected plume during August and September, *Chl* concentrations in the study area do not exceed 2 mg m^{-3} in these years.

Figure 17. August/September monthly-averaged *Chl* (mg m^{-3}) from 2003 to 2012 under the influence of the Amazon River plume retroflection.

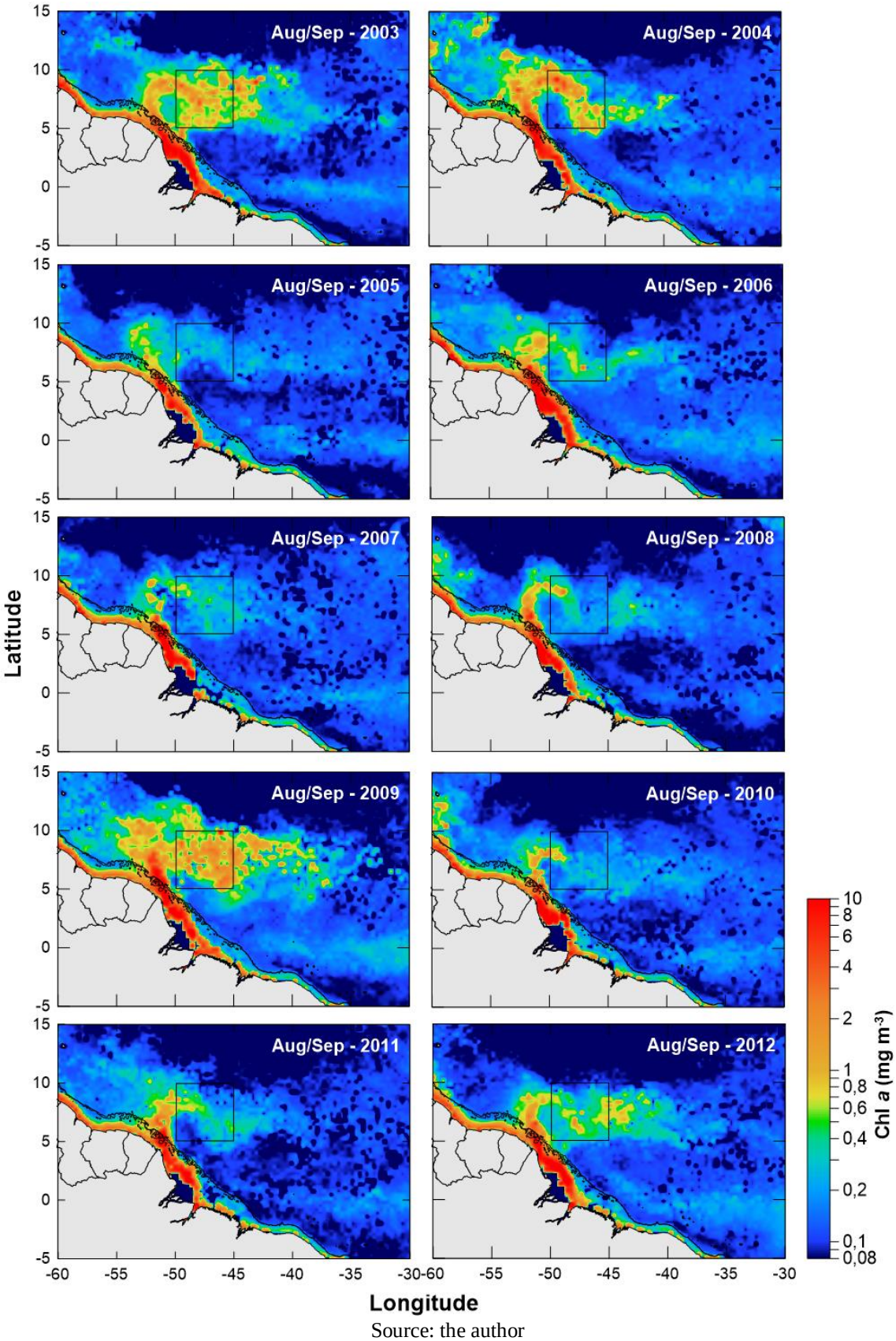

Source: the author

Chl concentrations in the study area exceeded the values of the rest of the series data in the following 5 years: 2003, 2004, 2006, 2009 and 2012. (Figures 17 and 18). *Chl* anomalies for the ten-year time series, rainfall, EC and EM (Figure 18) shows that, *Chl* positive anomalies values for 2003 (0.37 mg m^{-3}), 2004 (0.49 mg m^{-3}), 2009 (0.82 mg m^{-3}) and 2012 (0.48 mg m^{-3}) occur every second half of each year (August/September), except 2006 (0.68 mg m^{-3}), which positive anomaly was in May to July. For these years, rainfall was >24 mm, reaching 63 mm positive anomaly in late 2008 early 2009. Negative anomalies of *Chl* are identified in 2005 (-0.22 mg m^{-3}), 2007 (-0.24 mg m^{-3}), 2008 (-0.17 mg m^{-3}), 2010 (-0.17 mg m^{-3}) and 2011 (-0.19 mg m^{-3}). Rainfall presents values < -45 mm, with strong negative anomaly (-79 mm) in 2007, year of major negative anomaly of *Chl* in the series.

In 2003, positive *Chl* anomalies occurred in July (0.37 mg m^{-3}), August (0.29 mg m^{-3}) and September (0.28 mg m^{-3}) (Figure 17). In this year Q anomaly was mostly negative, with mean values of -2.5 x 10^4 m^3 m^{-1} between January and August, and positive from September to December, value of 1.23 x 10^4 m^3 m^{-1}. Rainfall anomalies shows values ranging from negative to positive along the year, with minimum of -78.5 mm in January and maximum of 24.8 mm in May. The EC mode initiates the year in El Niño phase in January (0.9 °C), changing to La Niña in May (-0.85 °C), and returning to El Niño until December (0.78 °C). EM remains positive along the year, with maximum anomaly of 0.58 °C occurring in March.

Figure 18. *Chl* (mg m^{-3}), Q (m^3 s^{-1}) and rainfall anomalies (mm) and EC and EM indexes.

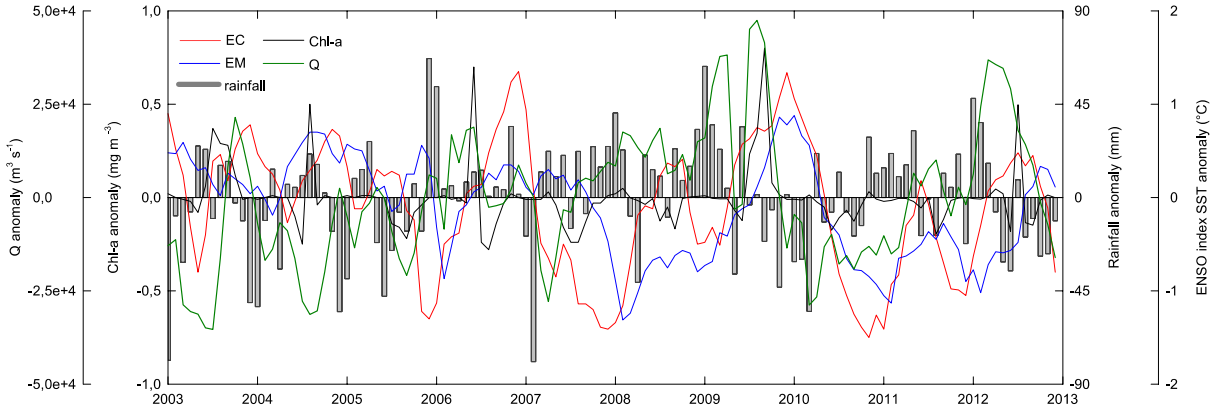

Source: the author

2004 exhibit similar behaviour as 2003 (Figure 18). The maximum anomaly of *Chl* (0.49 mg m^{-3}) occurs in August. The Q anomalies are negative from January to November, with the lowest value occurring in August (-3.13 x 10^4 m^3 m^{-1}), however, in December the Q anomaly

becomes positive (2.51 x 10^3 m^3 m^{-1}). The rainfall also oscillates between negative anomalies in January/February to positive in May to September, with 21 mm positive anomaly in August.

EC was positive from January to April, shifting to La Niña mode in May/June and returning to positive phase from July to December. EM for 2004 was mostly positive during the year, but with negative values in February, March and April.

In 2006, *Chl* remained negative throughout the year, though a positive peak (0.70 mg m^{-3}) occurred in June. Q was positive from March to June, where, in this month the flow rate was maximum, 1.89 x 10^4 m^3 s^{-1}. The maximum negative anomaly occurred in February with the value of -8.48 x 10^3 m^3 s^{-1}. The rainfall was positive in January, 53.4 mm, with a mean value of 11.6 mm along the year. EC presented La Niña phase from January to April and positive in the rest of the year. EM was negative from January to May with positive values occurring from June to December.

Chl in 2009 exhibit negative anomalies between February and June. Positive anomalies occurred in July (0.23 mg m^{-3}), August (0.34 mg m^{-3}) and September (0.80 mg m^{-3}) in this month, the maximum positive anomaly. Q values for this year presented positive anomalies in two distinct periods, from January to April and from July to November. The maximum Q positive anomaly occurred in August (4.75 x 10^4 m^3 s^{-1}). The rainfall in 2009 showed positive anomalies between January and April. January was the month with the highest positive anomaly of rainfall in the year, with a value of 63.3 mm. Negative anomaly occurred in May, -36.9 mm, followed by a positive anomaly in June, 34.1 mm. EC was negative between January and April, with average values of -0.35 °C, and positive from May to December. EM from January to July was in La Niña phase, becoming positive from August to December. November was the month of maximum positive anomaly in the year, 0.86 °C.

In 2012, there was a positive anomaly of *Chl* of 0.49 mg m^{-3} in July, followed by negative anomalies in August and September, -0.13 and -0.14 mg m^{-3} respectively. Q showed positive anomalies from January to September, maximum values in March, April and May. April was the month with the highest positive anomaly, 3.57 x 10^4 m^3 s^{-1}. In this year, Q negative values occurred in October, November and December. Rainfall shows positive anomalies from January to March, with maximum value, 47.8 mm, occurring in January. For the remaining year, the values were negative. EC was negative in January and February. From March, values become positive until October. The maximum positive anomaly occurred in July, 0.48 °C. EM was in La Niña phase from January to July, progressing to El Niño phase from August to December, maximum positive anomaly occurring in October, 0.33 °C. The 2005, 2007, 2008, 2010 and 2011 years, showed similar behaviour, where *Chl* remained with negative anomalies.

The Q values are mostly negative or positive anomalies not exceeding 1 x 10^3 m^2 s^{-1}. The rainfall values were in average 2.5 mm. EC and EM are mostly in their La Niña phase. The Table 2 shows averaged values of Q before *Chl* minimum (i.e. February to April) and maximum (i.e. June to September). Q anomaly values were selected with distinct lags through these two periods.

Table 2. Q anomalies before the period of minimum *Chl*, (February to April), and before the period of maximum *Chl* (June to September).

	Minimum *Chl*			**Maximum *Chl***		
Year	Q (m^3 s^{-1})	*Chl* (mg m^{-3})	Lag (months)	Q (m^3 s^{-1})	*Chl* (mg m^{-3})	Lag (months)
2003	-0.23	-0.52	2	-0.53	1.27	1
2004	0.08	-0.18	2	-0.17	0.16	1
2005	-0.06	-0.05	1	-0.02	-0.71	0
2006	**0.04**	**0.07**	0	**0.27**	**0.23**	1
2007	0.09	-0.41	2	-0.37	-1.12	3
2008	0.15	-0.51	1	0.24	-0.51	2
2009	**0.21**	**0.67**	1	**0.43**	**1.84**	0
2010	-0.11	-0.48	2	-0.40	-0.70	2
2011	-0.23	-0.14	4	-0.06	-0.53	4
2012	**0.04**	**0.06**	2	**0.63**	**0.64**	2

Source: the author

Q anomalies at the minimum *Chl* concentration period, exhibit negative anomalies around -0.23 m^3 s^{-1} in 2003 and 2011. -0.11 m^3 s^{-1} occurred in 2010 and -0.06 m^3 s^{-1} in 2005. In these years *Chl* concentration was negative, with values ranging from -0.52 mg m^{-3} (2003) to -0.05 mg m^{-3} (2005). Q present positive anomalies in the *Chl* minimum period in 2004 (0.08 m^3 s^{-1}), 2006 (0.04 m^3 s^{-1}), 2007 (0.09 m^3 s^{-1}), 2008 (0.15 m^3 s^{-1}), 2009 (0.21 m^3 s^{-1}) and 2012 (0.04 m^3 s^{-1}). Despite the Q positive anomalies for this period, *Chl* exhibit negative values in 2004 (-0.18 mg m^{-3}), 2007 (-0.41 mg m^{-3}) and 2008 (-0.51 mg m^{-3}). The *Chl* concentration in 2006, 2009 and 2012 years followed the Q positive anomalies with, 0.07, 0.67 and 0.06 mg m^{-3}, respectively.

Anomalies of Q for the maximum *Chl* period exhibit negative values in 2003 (-0.53 m^3 s^{-1}), 2004 (-0.17 m^3 s^{-1}), 2005 (-0.02 m^3 s^{-1}), 2007 (-0.37 m^3 s^{-1}), 2010 (-0.40 m^3 s^{-1}) and 2011 (-0.06 m^3 s^{-1}). *Chl* anomalies were negative in 2005, 2007, 2010 and 2011, except in 2003 and 2004 were *Chl* anomalies were positive, 1.27 and 0.16 mg m^{-3}, respectively. Q positive anomalies occurred in 2006 (0.27 m^3 s^{-1}), 2008 (0.24 m^3 s^{-1}), 2009 (0.43 m^3 s^{-1}) and 2012 (0.63

m^3 s^{-1}). Except for 2008, the *Chl* concentrations followed the Q positive anomalies in 2006 (0.23 mg m^{-3}), 2009 (1.84 mg m^{-3}) and 2012 (0.64 mg m^{-3}).

Discussion and Conclusions

General spatial patterns of chlorophyll-*a* (*Chl*) do exist in the surface ocean, resulting from differences in nutrient and light availability for phytoplankton growth, which are in turn influenced by regional and global physical processes. Latitudinal and seasonal changes in the wind forcing, solar radiation, ocean circulation and remote forcing play an important role in primary productivity (PP) (Sarmiento et al., 2004). In the continental shelves areas, changes are also expected due to the variability of freshwater outflows (Belkin, 2009) hence nutrient inputs and circulation patterns.

The climatology distribution of *Chl* (Figure 15) evidences the two *Chl* dispersion patterns over the WTNA. From December to March, *Chl* remains confined to the coast as the plume flows towards northwest above the shelf, and starts to spread beyond the shelf break in April/May. In the second period, from June to November, *Chl* concentration increases eastward in August/September, reducing again in October to November, with *Chl* values from 0.1 to 0.6 mg m^{-3} in the region.

Monthly climatology of sea surface temperature (SST), meridional wind stress (τy), zonal current (u) in the study area, river discharge (Q) and Amazon Basin rainfall (Figure 14) exhibit well defined seasonal cycles. In the first half of the year, rainfall is maximum in March, Q is maximum in May, and SST is minimum in February-March. τy is predominantly negative from July to November, indicating the presence of Northeast winds, while u is prevailing westwards and *Chl* is minimum. At the second half of the year, rainfall presents low values, Q decrease after June reaching a minimum in November and SST increases in September. τy weakens with values near 0.02 N m^{-2} in September, while u intensifies with positive values (0.22 m s^{-1}), indicating the retroflection of the North Brazil Current to east, and the rainfall decreases to a minimum in September.

The high Q lags rainfall by 2 months (r^2 = 0.85) and provides dissolved and detrital material to be spread over the WTA region, enhancing the nutrient input for *Chl*. Correlation between Q and *Chl* (r^2 = 0.60) show that, there is a 2 months delayed response of *Chl*. This can occur because the Q data where obtained from the Óbidos gauge station, which is 1369 km far away from the river mouth.

SST is correlated to *Chl* with zero lag (r^2 = 0.48). Despite the SST and *Chl* start to

increase in May, the maximum of *Chl* occurs in August while the maximum of SST occurs in September, however both present high values from June to October and decrease gradually during the rest of the year. The seasonal variability of SST has a positive correlation with the *Chl*, corresponding to the seasonal river discharge with a lag of 2 months. SST provides oceanic environment suitable for enhanced production. This seasonal pattern with positive correlation between SST and *Chl* is also described in Orinoco and Congo rivers, and suggests that, it results from high Q flow, that carry suspended (sediments) and dissolved material (nutrients) toward open ocean (Jutla et al., 2011). Suspended solids present on river plumes can increase the temperature of water as they absorb additional heat from the sun (Santos et al., 2008a).

The transition from negative to positive values of τy reflects the wind shift from the NE to SE flow direction, influenced by the north/south migration of the Intertropical Convergence Zone (ITCZ) (Santos et al., 2008b). Changes in wind direction from SE to NE, have great influence ($r^2 = 0.53$) in the residence of *Chl* concentrations near the river mouth (Salisbury et al., 2011). The u variation, from negative to positive, is interpreted as the current moving from west to east, toward offshore waters. From January to June, the NBC presents low transport rates toward the Central Equatorial Atlantic. From July to November, NBC increase the transport rates, toward the North Equatorial Countercurrent (NECC) (Muller-Karger et al., 1988; Fratantoni and Glickson, 2002) which support the plume dispersion over the WTA waters. This presents high influence ($r^2 = 0.40$) on *Chl* dispersion in the WTA region. *Chl* concentrations in the study area exceeded the values of the rest of the series data in the following 5 years: 2003, 2004, 2006, 2009 and 2012. (Figures 17 and 18). *Chl* anomalies for the ten-year time series, rainfall, EC and EM (Figure 18) shows that, *Chl* positive anomalies values for 2003 (0.37), 2004 (0.49), 2009 (0.82) and 2012 (0.48) occur every second half of each year (August/September), except 2006 (0.68), which positive anomaly occurred in June.

The interannual variability of *Chl*, EM, EC and rainfall/discharge events is shown in the Figure 12. Despite the Modoki presence in 2001/2002 years, in 2003 and 2004, the positive Q anomalies don't occur after the rainfall in 2003 and 2004 as expected, as mentioned, Óbidos gauge station is far 1369 km from the Amazon River mouth (Dai and Trenberth, 2002), and we can also consider an influence of Tocantins and Araguaia Rivers discharge that flow to the ocean, near the Amazon River mouth in the positive anomaly of *Chl* in these years. In August-November 2005 there is an El Niño phase of Modoki signal, succeeded by a La Niña phase, which is coincident with positive rainfall anomalies from November 2005 to January 2006, lagged by 2 months of positive Q anomalies from March to July 2006, and positive *Chl* anomaly

at the end of this period, which occurs at the beginning of the El Niño phase of Modoki event in this year.

The most intense positive anomaly of *Chl* occurred in 2009. This anomaly was caused by a strong Modoki La Niña event influencing the rainfall, which took place in early 2008 and extended until March-April of 2009. During this period, the positive rainfall anomaly in the Amazon River Basin occurred for nearly all of 2008 and exhibited greater intensity at the beginning of 2009. The Modoki La Niña was succeeded by a strong El Niño phase, the strongest of the series that have effects on the persistent rainfall in the Amazon Basin. The La Niña Modoki, contributed to positive anomalies of rainfall, with maximum peak in January 2009, lagged by positive discharge anomaly 2 months later, in March 2009, and a second and stronger peak of discharge anomaly in July/September, leading to a positive *Chl* anomaly in September/October, that coincide with the El Niño phase of Modoki, in the second semester of 2009.

In April 2010 starts a strong La Niña Modoki phase, with positive rainfall anomalies 6 months later, in October, lagged by 2 months of weak positive anomalies of discharge at the middle of 2011, when starts a second peak of La Niña Modoki, accompanied by strong positive rainfall anomalies at the first semester of 2012, lagged by 2 months of positive discharge anomalies during the remainder of the year. The maximum peak of discharge leads about 3 months the positive *Chl* anomalies.

The canonical La Niña exceeded La Niña Modoki phase in 2006 and intensified positive rainfall anomalies, while in 2009 and 2012 the La Niña Modoki phase was stronger than canonical La Niña and caused positive rainfall anomalies in these years. The transition from strong La Niña to the El Niño phase of Modoki in 2006, 2009 and 2012, stands out as the precursor to positive anomalies of rainfall, discharge and high productivity. This interannual variability caused a shift in phase of the *Chl* in 2006, while in 2009 and 2012 it reinforces the seasonal cycle. The averaged values of Q and *Chl* anomalies show that in the years of 2006, 2009 and 2012, there is a positive response of *Chl* anomalies to the positive anomalies of Q in both semesters, indicating that the interannual variability not only intensified the seasonal cycle in these years, but also increase the productivity along the year.

The Table 2 shows averaged values of Q and *Chl* anomalies, highlighting what happens with the Q anomaly before the period of minimum *Chl* (i.e. February/April) and, what happens with Q anomaly before the period of maximum *Chl*, (i.e. June/September). As described, Q negative anomalies occurred in 2003, 2005, 2010 and 2011, and as expected, *Chl* negative anomalies followed this Q anomalies for these years. Q positive anomalies occurred in 2004,

2006, 2007, 2008, 2009 and 2012. The typical behaviour, where, increased Q leads to increased *Chl* occurred only in 2006, 2009 and 2012. For 2009, Q exhibits the maximum positive anomaly for this period, 0.21 $m^3 s^{-1}$, where is also followed by the maximum positive anomaly of *Chl*, 0.67 mg m^{-3}, in the minimum *Chl* period.

During the maximum *Chl* period, Q presented negative anomalies in 2003, 2004, 2005, 2007, 2008, 2010 and 2011. Despite the Q negative anomaly, the *Chl* concentration anomaly was positive in 2003 and 2004. This behaviour shows that in those years the *Chl* was not directly influenced by the Q anomaly. However, is worth emphasizing that the *Chl* concentration anomaly in 2003 was strong, equalling the value to the years of positive Q. Positive anomalies of Q occurred only in 2006, 2009 and 2012. The *Chl* presents positive anomalies, with values much higher than presented in the minimum *Chl* period. Again 2009 was the year of maximum *Chl* concentration anomaly, 1.84 mg m^{-3}. The years of 2006, 2009 and 2012 were the ones to present *Chl* and Q positive anomalies in both periods (minimum and maximum *Chl*), but the *Chl* values on the maximum period were substantially high. In 2006 and 2009, the *Chl* anomalies were more than three times, and in 2012 more than ten over the minimum *Chl* period.

The analysis presented here revealed a strong seasonal and interannual cycle dominating the variability of *Chl* in the Western Tropical Atlantic. We investigated how the recent increased occurrences of Central Pacific/Modoki El Niño episodes (versus Eastern Pacific/canonical El Niños) are reflected in the *Chl* concentrations in the Amazon River plume. The results showed distinct surface *Chl* concentration patterns concerning different ENSO phases (El Niño - La Niña) and indexes (canonical and Modoki), which is linked to river discharge variability due to higher rainfall over the Amazon Basin.

We conclude that the seasonal and interannual variability of *Chl* concentrations in the study area is the result of different stages in the local and remote forcing. Using ten years of *Chl* satellite data, we draw the following conclusions: (i) *Chl* is influenced by Q, SST, τy and u variability on a seasonal scale; (ii) *Chl* distribution and concentration over the WTA is influenced by nutrient supply from the high river discharge (Q), by southeast meridional wind stress (τy) and zonal current (u) east intensification, where nutrients are carried eastward to the open ocean; (iii) The ENSO variability have strong influence in the Q and *Chl* concentration not only at seasonal scales, but throughout the year; (iv) *Chl* positive anomalies are linked to strong rainfall/Q events influenced by canonical (La Niña phase) and more strongly by Modoki (La Niña/El Niño) modes with an interannual variability of 3 years.

Hence, we speculate that an increasing EM frequency will affect positively the phytoplankton growth in the WTNA waters, but further investigations are needed. A potential

outcome of this study is to investigate how Pacific ENSO change affects ocean biogeochemistry pathways and sea-air CO_2 exchanges (global warming feedback) as well as the habitats and ecology of the local species in the Western Tropical North Atlantic.

4.2 Amazon Plume salinity response to ocean teleconnections

The second manuscript was accepted by the *Frontiers in Marine Science* periodic. The paper has as main objective analyse the sea surface salinity (SSS) response to Pacific and Atlantic climate indices over the Amazon plume. For this, 46 years of sea surface temperature (SST) over the Pacific and Atlantic Oceans, rainfall in the Amazon basin, and SSS over the Amazon plume were used. This paper is described as follow:

Abstract

Pacific and Atlantic sea surface temperature (SST) variability strongly influences rainfall changes in the Amazon River basin, which impacts on the river discharge and consequently the sea surface salinity (SSS) in the Amazon plume. An Empirical Orthogonal Function (EOF) analysis was performed using 46 years of SST, rainfall, and SSS datasets, to establish the relationship between these variables. The first three modes of SST/rainfall explained 87.83% of the total covariance. Pacific and Atlantic SSTs led Amazon basin rainfall events by four months. The resultant SSS in the Western Tropical North Atlantic (WTNA) lagged basin rainfall by three months, with 75.04% of the total covariance corresponding to the first four EOF modes. The first EOF mode indicated a strong SSS pattern along the coast that was connected to negative rainfall anomalies covering the Amazon basin, linked to El Niño events. A second pattern also presented positive SSS anomalies, when the rainfall was predominantly over the northwestern part of the Amazon basin, with low rainfall around the Amazon River mouth. The pattern with negative SSS anomalies in the WTNA was associated with the fourth mode, when positive rainfall anomalies were concentrated in the northwest part of South America. The spatial rainfall structure of this fourth mode was associated with the spatial rainfall distribution found in the third EOF mode of SST vs rainfall, which was a response to La Niña Modoki events. A statistical analysis for the 46-year period and monthly anomaly composites for 2008 and 2009 indicated that La Niña Modoki events can be used for the prediction of low SSS patterns in the WTNA.

Keywords: El Niño. Sea surface temperature. rainfall. Sea surface salinity. Amazon River plume.

Introduction

Ocean salinity is an indicator of changes in the global hydrological cycle and large-scale climate variability (Du et al., 2015). The spatial distribution of salt in the ocean and its seasonal and interannual variability are important for understanding Earth's climate. Ocean salinity has an important role in the thermohaline circulation and the distribution of mass and heat. The spatial distribution of sea surface salinity (SSS) in the global ocean also reflects the pattern of air-sea freshwater fluxes, evaporation and precipitation, heat, momentum, solubility, and the biological pump (Geider et al., 2001; Yu et al., 2007; Schmitt, 2008; Du et al., 2015).

Changes in salinity patterns indicate where terrestrial and marine systems mix, which is where nutrients are distributed, and in turn impacts on the production of coastal and oceanic ecosystems (Smith and Demaster, 1996; Araujo et al., 2014). The Amazon River is by far the largest single source of terrestrial freshwater to the ocean, contributing approximately 20–30% of the total river discharge to the Atlantic (Wisser et al., 2010; Salisbury et al., 2011; Korosov et al., 2015). SSS in the western tropical North Atlantic (WTNA) is strongly influenced by the Amazon River discharge, advection by surface currents, and rainfall (Grodsky et al., 2015; Ibánhez et al., 2017). The low salinity Amazon plume creates a near-surface barrier layer that inhibits mixing, increases the sea surface temperature (SST), and enhances salinity stratification thus, preventing vertical mixing between the upper warm mixed layer and the cold deep ocean (Ferry and Reverdin, 2004; Balaguru et al., 2012; Grodsky et al., 2012; Coles et al., 2013).

The latitudinal displacement of the Intertropical Convergence Zone (ITCZ) in association with high precipitation modifies the surface conditions, following the input of freshwater inputs from large rivers. Ibánhez et al. (2017) compared the monthly precipitation rate with monthly SSS in five regions of the tropical Atlantic. They found significant linear relationships of precipitation with SSS across the western Atlantic basin. The extension of the Amazon River plume is significant, with a range of 0.25 to 1.60 $\times$ 10^6 km^2 after removing the influence of rainfall. The intense rainfall associated with the ITCZ has led to a significant overestimation of the spatial extension of the Amazon River plume in previous studies (Körtzinger, 2003; Lefèvre et al., 2010).

The Amazon plume is transported by the North Brazilian Current (NBC) near the equator and is carried northwestward along the Brazilian Shelf towards the Caribbean Sea (Muller-Karger et al., 1988; Salisbury et al., 2011). The eastward propagation of Amazon waters is observed when the retroflection of the NBC takes place. The seasonal variations in these currents occurs in response to the annual migration of the ITCZ, which leads to the northward transport of Amazon water in the austral winter, and the eastward transport of

Amazon water into the North Equatorial Counter Current (NECC) in the austral spring through fall (Muller-Karger et al., 1988; Lentz, 1995; Coles et al., 2013; Foltz et al., 2015). The fresh and cold waters of the Amazon River are then transported hundreds to thousands of kilometers away from the coast, and the nutrients delivered by the river plume contribute to the enhancement of primary production thus, contributing to carbon sequestration (Subramanian et al., 2008).

The Amazon River discharge is also affected by remote climatic signals via Amazon basin rainfall variability that is under different influences from the Pacific and Atlantic tropical oceans. The influence of the El Niño Southern Oscillation (ENSO) on seasonal precipitation anomalies over South America has been extensively studied (Marengo, 1992; Uvo et al., 1998; Grimm et al., 2000; Paegle and Mo, 2002; Ronchail et al., 2002; Grimm, 2003, 2004; Misra, 2008a). ENSO influences the large-scale east–west and meridional circulations in the global tropics that have consequences over tropical South America (Grimm, 2003, 2004; Misra, 2008b).

The rainfall over the Amazon basin and northeast Brazil has a distinct interannual variability, in part due to the climate signals in the tropical Pacific from the ENSO and to the meridional SST gradient in the tropical Atlantic (Marengo et al., 2013). This modify the spatial and temporal Amazon rainfall variability, consequently affecting the Amazon plume. Recent studies have shown that the canonical ENSO has become less frequent, while a different kind of ENSO in the central Pacific, called the Modoki ENSO, is occurring more frequently and has become more common during the late twentieth century (Ashok et al., 2007; Ashok and Yamagata, 2009; Kao and Yu, 2009; Yeh et al., 2009; Yu et al., 2010; Li et al., 2011; McPhaden et al., 2011). The traditional ENSO is characterized by strong anomalous warming in the eastern equatorial Pacific. In contrast, the Modoki ENSO phenomenon is characterized by an anomalous warm SST in the central equatorial Pacific, flanked by anomalously cool regions in both the west and east. The teleconnections associated with these distinct warming and cooling patterns are very different from those of the conventional ENSO (Yeh et al., 2009).

Weng et al. (2007) performed a correlation analysis between Global Precipitation Climatology Centre (GPCC) rainfall rate anomalies and the El Niño Modoki Index (EMI) and Niño 3. They identified positive and negative rainfall anomalies over northwest South America related to Niño 3. However, during Modoki El Niño events, they found negative rainfall anomalies over the east Pacific and positive rainfall anomalies in the western part of the Amazon basin. Because of the conclusions of this and other studies, the Modoki ENSO is considered to be a new driver of global climate change (Xie et al., 2014) and is being linked to

global warming (Yeh et al., 2009). Based on the detection of the principal Empirical Orthogonal Function (EOF) analysis modes, this study identified the coupled modes of variability between SSTs and rainfall over the Amazon basin, and between Amazon rainfall and SSS over the Amazon plume in the WTNA to better understand the climate impacts on biogeochemical cycles in the WTNA.

Datasets

Datasets containing 46-year (January 1970 to December 2015) records of SST, rainfall, and SSS were used to conduct the analysis. SST monthly data were obtained from the Ocean ReAnalysis System 4 (ORAS4: http://icdc.cen.uni-hamburg.de/), with 1° × 1° grid resolution. ORAS4 was evaluated by comparison with observed ocean currents, derived transport, sea-level gauges, and bottom pressure (Balmaseda et al., 2013). The monthly rainfall data were obtained from the GPCC, full data reanalysis version 7 (GPCC v7: http://www.esrl.noaa.gov/psd/). The GPCC v7 provides global land-surface rainfall in a regular grid, with a resolution of 1° × 1°. This dataset is based on 75,000 gauges located worldwide and enables the analysis of climate variability and historical trends (Schneider et al., 2014, 2015). The Global Precipitation Climatology Project (GPCP), version 2.3, with 2.5° resolution was also used to determine anomalies of land and oceanic rainfall. In addition to SST, SSS was also obtained from the ORAS4 database, with the same spatial and temporal resolution.

We also used data for 46 years of monthly Amazon discharge values recorded at the Óbidos Gauging Station, which was available from the Environmental Research Observatory – Geodynamical, hydrological and biogeochemical control of erosion/alteration and material transport in the Amazon basin (ORE–HYBAM: http://www.ore-hybam.org). The values recorded at the Óbidos Gauging Station, about 600 km west of the river mouth, were used to estimate the interannual variability of the Amazon River discharge.

In this study, we used data for 46 years of monthly zonal, meridional, and vertical components of winds from ERA-Interim reanalysis, produced by the European Centre for Medium-Range Weather Forecasts (ECMWF), and available at http://www.ecmwf.int/.

Statistical analysis

The influence of the Pacific and Atlantic SST on rainfall over South America and the rainfall distribution on SSS in the Amazon River plume on an interannual timescale was analysed by applying a coupled EOF analysis. The EOF was constructed by a Singular Value

Decomposition (SVD) analysis (Bretherton et al., 1992; Wallace et al., 1992) of the cross-covariance matrix between SST (140°E–20°E, 20°S–20°N) and rainfall (20°S–20°N and 80°W–20°E) for the dataset period. SVD was conducted by analysing the covariance matrix between Pacific and Atlantic SSTs and precipitation anomalies over South America, and was conducted after the monthly climatology were removed from the SST, rainfall, and SSS datasets.

From this analysis, we computed the loadings and scores for both modes, SST vs rainfall and rainfall vs SSS. These loadings were computed from the left and right eigenvectors and represented the spatial patterns of the corresponding mode. The scores of the SVD modes were computed by projecting the data on to the loadings of the corresponding field. The squared covariance fraction (SCF) expresses the percentage explained by the modes. One of the benefits of SVD is that the order of the calculated modes is based on the strength of their co-variability, as the first mode is the strongest and the last mode is the weakest. To identify the connection between rainfall EOF patterns, a linear regression analysis was performed between the rainfall vs SSS principal components (PCs) and SST vs rainfall PCs.

To improve the analysis of rainfall behaviour over the Amazon basin, the PCs from each EOF were correlated with Pacific and Atlantic climatic indices (Table 3). The statistical significance of the cross-correlations between climate indices and the PCs was determined from a two-sample *t*-test at 95% confidence levels. The climatic indices were obtained from the Earth System Research Laboratory/National Oceanic and Atmospheric Administration (ESRL/NOAA), and are available at https://www.esrl.noaa.gov/.

Table 3. ENSO and Atlantic climate indices and respective regions of SST anomalies

Index	Covered area
Niño12	El Niño 1+2. Area-averaged SST anomaly over Extreme Eastern Pacific SST, from equator to 10° S, 90° W - 80° W
Niño3	El Niño 3. Area-averaged SST anomaly over Eastern Tropical Pacific SST, 5° N - 5° S, 150° W - 90° W
Niño34	El Niño 3.4. Area-averaged SST anomaly over East Central Pacific SST, 5° N - 5° S, 170° W-120° W
Niño4	El Niño 4. Area-averaged SST anomaly over Central Pacific SST, 5° N-5° S, 160° E-150° W
EMI	El Niño Modoki Index. Computed by combining SST anomalies averaged over each box-area, A-(B+C)/2. Where: A (165° E -140° W, 10° S - 10° N), B (110° W - 70° W, 15° S - 5° N) and, C (125° E - 145° E, 10° S - 20° N)
NTA	North Tropical Atlantic SST Index. SST anomalies averaged over 60° W - 20° W, 6° N - 18° N and 20° W - 10° W, 6° N - 10° N
TNA	Tropical Northern Atlantic Index. SST anomalies averaged over 57.5° W - 15° W and 5.5° N - 23.5° N
TSA	Tropical Southern Atlantic Index. SST anomalies averaged over Eq – 20° S and 10° E - 30° W
AMM	Atlantic Meridional Mode. Maximum Covariance Analysis (MCA) to sea surface temperature (SST) and the zonal and meridional components of the 10m wind field over the time period 1950-2005, from the NCEP/NCAR Reanalysis. The spatial pattern covers 21° S – 32° N, 74° W – 15° E
CTA	Cold tongue anomaly, SST anomalies averaged over 10° W – 15° E and 5° N – 5° S

Source: the author

Results and discussion

Pacific and Atlantic SST vs Amazon basin rainfall

The distinct patterns of SST anomalies in the Pacific and Atlantic oceans induced different rainfall responses over the watershed of the Amazon basin and this subsequently influenced the river discharge. The results of the EOFs performed between SST and rainfall reflected this behaviour. The EOF analysis was performed with rainfall lagging SST by one to four months. SST acted as the predictor and precipitation acted as the response series. The results were limited to a four month-lagged cross-covariance matrix, with rainfall lagging SST, based on the best response relation. This EOF analysis of the lagged cross-covariance matrix between tropical Pacific and Atlantic SST and rainfall in the Amazon basin revealed three main modes. These modes together explained 87.83% of the total covariance between SST and rainfall, with 73.89, 7.91, and 6.03% of the signal explained by EOF1, EOF2, and EOF3 respectively. The PC1 SST signal was correlated with El Niño 3 (0.94, $p < 0.05$). In the canonical El Niño phase, SST anomalies over tropical and subtropical latitudes were warmer than normal. The spatial pattern of EOF1 (Figure 19) was characterized by a basin-scale

warming from the eastern to central Pacific, which was negatively associated with rainfall in the northeast Amazon basin portion. Rainfall during a canonical El Niño event was increased in the west coast regions of South America, while La Niña events increased rainfall over central South America and the Amazon basin. The regions in the Amazon basin that received most rainfall corresponded to the western portion of the watershed near the Andean elevation. Below average rainfall covered the central and eastern areas of the basin, near the river mouth.

It is known from previous work that on interannual timescales the ENSO system has a large variance in the Pacific (Yeh and Kirtman, 2004; Di Lorenzo et al., 2015). Jiménez-Muñoz et al. (2016) have classified the 2015/2016 El Niño event as an unprecedented warming, with extreme drought in Amazonia compared to the earlier strong El Niño events of 1982/83 and 1997/98. They found that both eastern and central Pacific SST anomalies in December 2015 contributed to this ENSO, with a strong decay from January to June 2016, which was characterized by a stronger contribution from the central Pacific.

Figure 19. First EOF mode of 4 month-lagged covariance matrix between SST and rainfall (normalized scale by 10^3), the Squared Covariance Fraction (SCF) in percentage, and the first Principal Component (PC1).

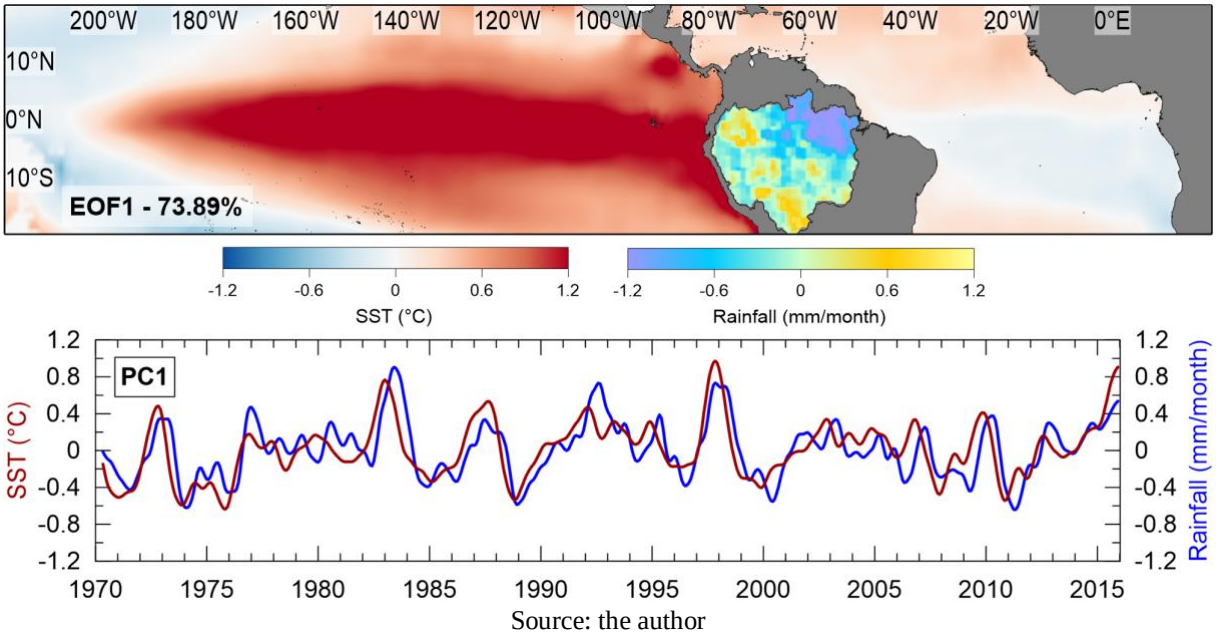

Source: the author

As shown in Figure 19, the Pacific SST anomalies in the Pacific Ocean were most often present near the South American coast, dispersing westward through the ocean, with a pattern similar to El Niño 3. Following this SST pattern, rainfall was more concentrated in the westward and southwestward portion of the Amazon basin. El Niño 3 events are associated with periodic severe droughts in Amazonia due to convective inhibition and rainfall reduction in the northern,

eastern, and western parts of Amazonia (Marengo and Espinoza, 2015). Some of this reduction in rainfall in Amazonia is associated with canonical El Niño events, with a contribution from the Atlantic. This increase in SST would weaken the northeast trade winds, reducing the moisture transport from the tropical Atlantic into the Amazon region.

PC2 (Figure 20), which corresponded to 7.91% of the variance, was negatively correlated with the cold tongue anomaly (CTA) (-0.74, $p < 0.05$). The EOF2 pattern was characterized by sparse positive rainfall anomalies mainly in the central part of the Amazon basin (Figure 20). The sparse rainfall distribution was weakly correlated with Pacific climatic indices, but there were stronger negative correlations with the equatorial and North Atlantic (Table 4). Marengo (1992) and Marengo et al. (2008) reported that cold SST events in the North Atlantic were associated with stronger northeast trade winds and an increase in moisture transport from the North Atlantic into the Amazon.

Figure 20. Second EOF of 4 month-lagged covariance matrix between SST and rainfall (normalized scale by 10^3), the Squared Covariance Fraction (SCF) in percentage, and the second Principal Component (PC2).

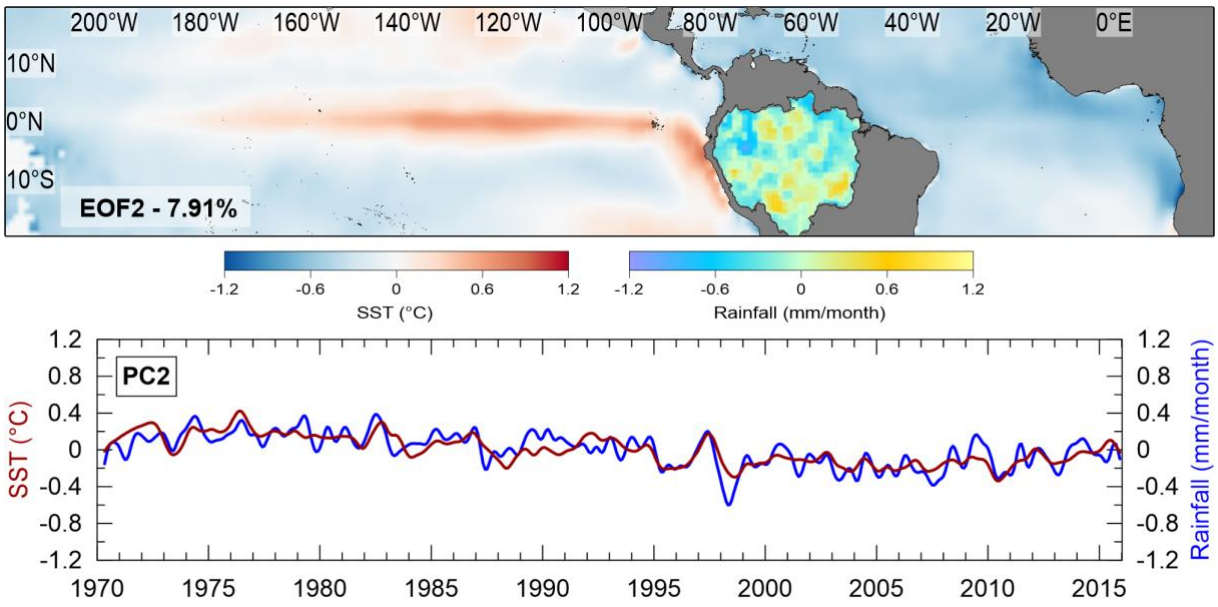

Source: the author

Table 4. 46 years Cross-correlation between PCs of 4 month-lagged EOF SST x Rainfall with Pacific and Atlantic Indices. The cross-correlations in bold are significant with 95% confidence level. The effective number of degrees of freedom (dof) was calculated by the autocorrelation scale.

	Niño12 *dof=95*	**Niño3** *dof=98*	**Niño34** *dof=92*	**Niño4** *dof=71*	**TNA** *dof=17*	**TSA** *dof=68*	**AMM** *dof=47*	**CTA** *dof=16*	**EMI** *dof=63*
PC1 SST	**0.80***	**0.94***	**0.94***	**0.85***	**0.25***	-0.01	-0.03	0.03	**0.43***
PC2 SST	**0.15***	**0.12***	**0.12***	-0.06	**-0.62***	**-0.58***	**-0.46***	**-0.75***	0.06
PC3 SST	**0.32***	-0.04	**-0.28***	**-0.56***	**-0.09***	-0.04	-0.03	**-0.13***	**-0.83***

α = 0.05; *dof, degrees of freedom; cc, cross-correlation

Source: the author

The spatial pattern of EOF3 (Figure 21) corresponded to 6% of the covariance and exhibited a zonal structure in the cooling of SSTs in the central Pacific and a warming in the eastern Pacific. PC3 (Figure 21) was negatively correlated with the EMI (-0.83, $p < 0.05$) (Table 2). The PC (Figure 21) associated with this mode corresponded to the negative phase of the Modoki ENSO (La Niña Modoki). The negative correlation presented in the EOF3 indicated that the positive rainfall anomalies over northwest South America responded to La Niña Modoki events. La Niña Modoki events have received less attention than prominent canonical La Niña events observed in the central Pacific due to the difficulty in identifying distinct types of cold events (Shinoda et al., 2011; Kulkarni and Siingh, 2016).

Despite the PC correlation with the negative phase of Modoki El Niño and canonical La Niña events being similar, the spatial structure of SSTs (Figure 21) was characterized by a cold area in the central Pacific and a warmer area in the eastern Pacific, which is a characteristic of La Niña Modoki events (Ashok et al., 2007). The corresponding EOF3 spatial pattern of rainfall over the continent is shown in Figure 21, and indicated positive rainfall anomalies in the northwestern part of the Amazon basin. This is the area that makes the largest contribution to the Amazon River discharge and is formed mainly by the junction of the Negro River, coming from the northwest, and the Solimões River (Beluco and Souza, 2014).

Figure 21. Third EOF of 4 month-lagged covariance matrix between SST and rainfall (normalized scale by 10^3), the Squared Covariance Fraction (SCF) in percentage, and the third Principal Component (PC3).

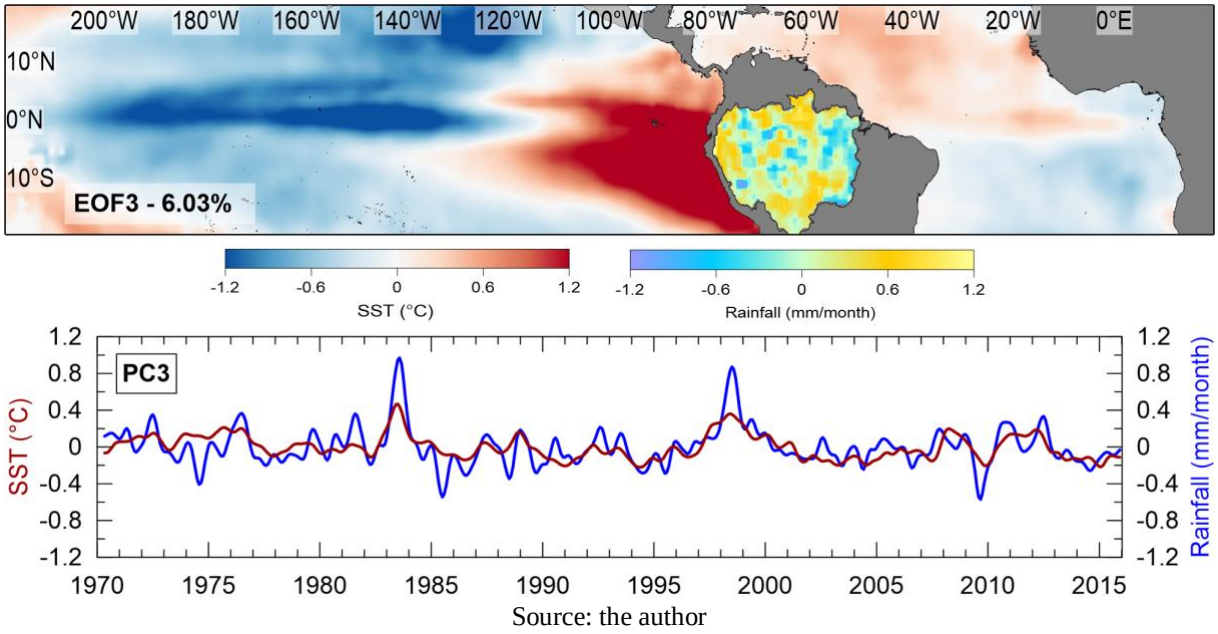

Source: the author

A similar spatial pattern was also reported by Ashok et al. (2007), although they performed a single EOF of SSTs over the Pacific, from 1979 to 2004. They identified the first mode as a canonical El Niño event (45%), with the second mode corresponding to the Modoki signal explaining 12% of the SST variability, the third mode explaining 7%, and the fourth mode explaining 4.5%. Using SST composites, the authors identified two seasonal Modoki events. The first one, which occurred in the austral winter (June to September), was warmer in the central Pacific and extended northeastward in the North Atlantic and southeastward in the South Atlantic. The other mode was confined to the equatorial Pacific from December to February.

Amazon basin rainfall vs WTNA SSS

The EOF spatial patterns of South American rainfall vs SSS over the western tropical WTNA covered the area from 20°S to 20°N and 80°W to 20°E. The best response (i.e., stronger correlations) of SSS to the South American rainfall variability occurred with a three-month lag. Results were limited to the coupled EOF with three month-lagged SSS. The first four modes retained 70.49% of the total covariance between SSTs and rainfall. The first and third spatial modes of rainfall over South America showed a similar pattern to those found for the rainfall patterns of the coupled EOF of SST vs rainfall.

The first mode explained 43.46% of the covariance (Figure 22). The rainfall pattern over the continent corresponded to the spatial pattern found in the first mode between SST and

rainfall with a correlation of 0.96 ($p < 0.05$) (EOF1, Figure 19), which was associated with canonical El Niño events (Table 4). The negative rainfall over the Amazon basin was mostly attributed to canonical El Niño events, with strong droughts experienced in the Amazon basin in 1983, 1997, 2005, and 2010 (Marengo et al., 2013).

Figure 22. First EOF of 3 month-lagged covariance matrix between rainfall (normalized scale by 10^3) and SSS (normalized scale by 10), the Squared Covariance Fraction (SCF) in percentage, and the first Principal Component (PC1).

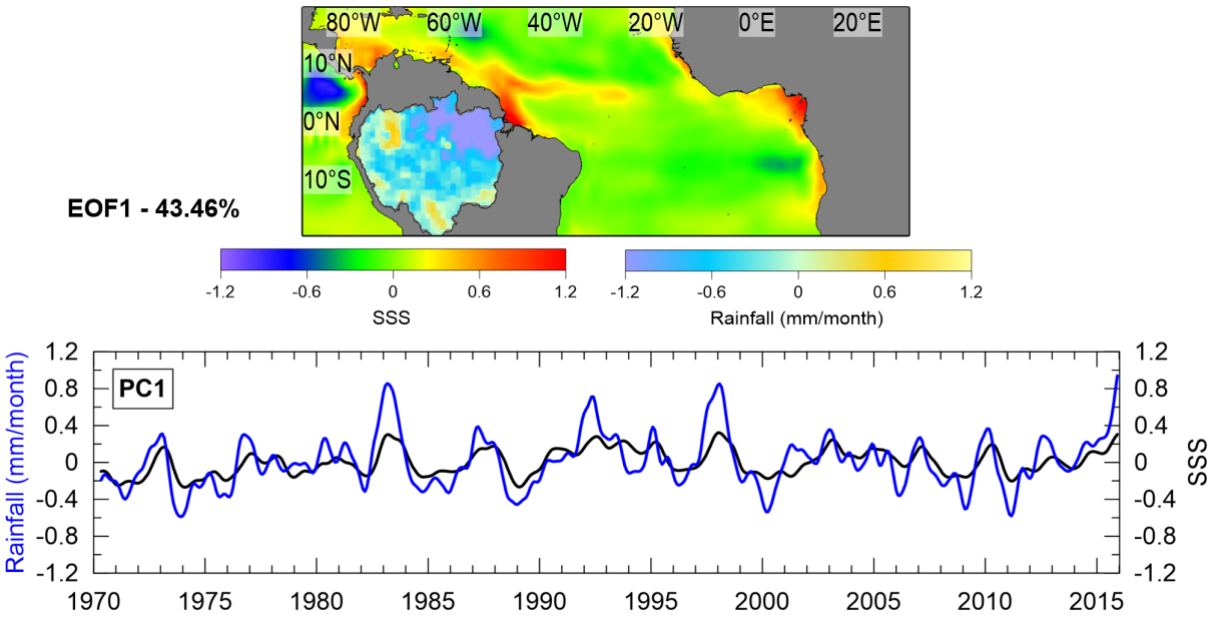

Source: the author

As expected, this rainfall pattern was associated with high SSS along the coast, indicating that negative rainfall anomalies contributed to a low river discharge and consequently high SSS in the WTNA. This high SSS was present along the coast propagating northwestward. At about 50–55°W part of this signal was characterized by an eastward retroflection, with a zonal axis and maximum SSS centered at about 6°–8°N (Figure 22). The eastward NBC retroflection entered the western part of the NECC, transporting salty water that was still detectable until it reached 30°W. Similar structures were also detected by Grodsky et al. (2014a, 2014b), during periods when the Amazon River discharge was low, and salty surface water from the southwestern equatorial Atlantic was transported by the NBC. North of 10°N and west of 50°W there was a core of low SSS, while to the east the low SSS propagated along 10°N. Some studies have described low salinity cores near Caribbean islands, trapped within NBC rings (Johns et al., 1998; Kelly et al., 2000; Hellweger and Gordon, 2002), with typical diameters up to 400 km and a life time of about 100 days.

EOF2 (Figure 23) explained about 14% of the covariance. The spatial distribution of

rainfall over the continent indicated sparse positive rainfall anomalies over the western part of the Amazon basin decreasing to the east, while negative rainfall anomalies were present near the Amazon River mouth. This pattern was associated with a high SSS that was confined to areas near the coast and transported northwestward, with part of this turning right. This eastward pathway that transported the higher salinities followed the NECC meanders, and enclosed a low salinity core with negative SSS anomalies.

Figure 23. Second EOF of 3 month-lagged covariance matrix between rainfall (normalized scale by 10^3) and SSS (normalized scale by 10), the Squared Covariance Fraction (SCF) in percentage, and the second Principal Component (PC2).

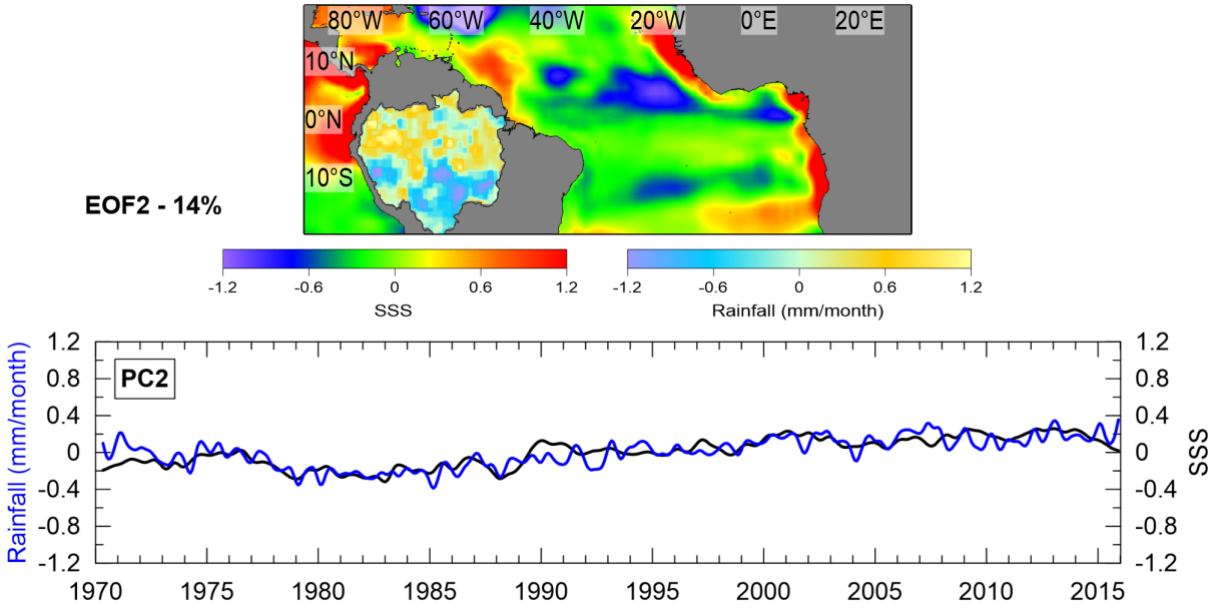

Source: the author

EOF3 (Figure 24) corresponded to 7.54% of the covariance and presented positive rainfall anomalies in the western part of the Amazon basin and negative rainfall anomalies mainly in the northeastern area along the coast. This pattern is associated with a northward axis (50°W) of positive SSS anomalies. This SSS signal was similar to the first mode, however, it was weaker and also had an eastward pathway between 6–8°N, following the NECC.

Figure 24. Third EOF of 3 month-lagged covariance matrix between rainfall (normalized scale by 10^3) and SSS (normalized scale by 10), the Squared Covariance Fraction (SCF) in percentage, and the third Principal Component (PC3).

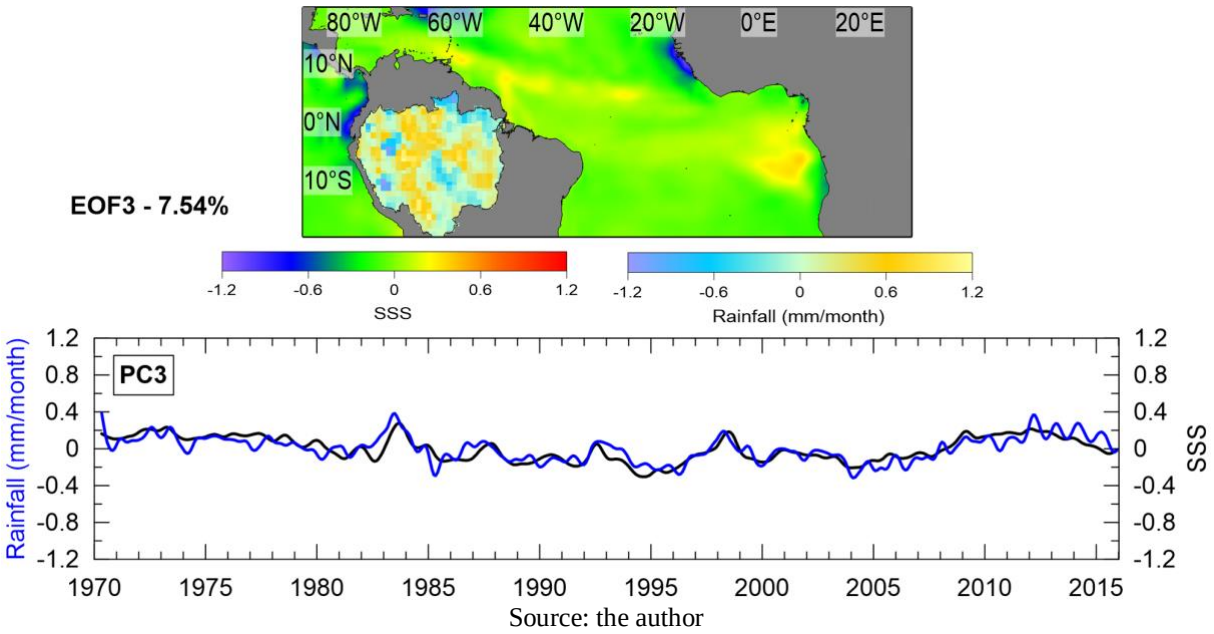

Source: the author

Figure 25 shows EOF4, which was between rainfall and SSS and explained 5.51% of the covariance. This rainfall pattern was similar to the rainfall structure of the third mode of the coupled EOF between SST and rainfall, which explained 6% of the covariance (EOF3, Figure 21), and was associated with cold equatorial waters in the central Pacific and warm waters in the eastern part of the Pacific. It was significantly negatively correlated with the negative phase of Modoki El Niño events (-0.83, Table 4). EOF4 presented positive rainfall anomalies mainly along the Orinoco and Negro basins in the northern area of northeast Brazil. This pattern showed a low-salinity plume emanating from the Amazon mouth in the WTNA, with a retroflection centered at 50°W and an eastward propagation along 6–8°N. The most striking pattern was the way the Amazon plume responded to the NBC and NECC.

Figure 25. Fourth EOF of 3 month-lagged covariance matrix between rainfall (normalized scale by 10^3) and SSS (normalized scale by 10), the Squared Covariance Fraction (SCF) in percentage, and the fourth Principal Component (PC4).

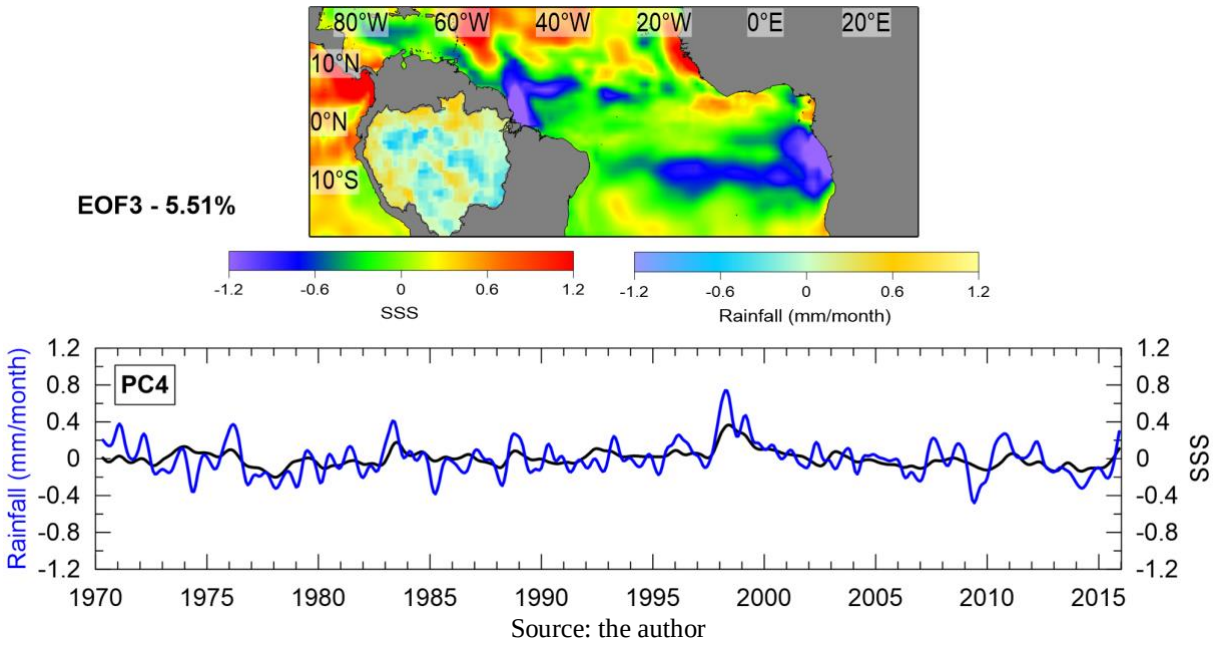

Source: the author

In our EOF analysis, similar spatial rainfall patterns were found between the EOF1 SST vs rainfall and EOF1 rainfall vs SSS, and between EOF3 SST vs rainfall and EOF4 rainfall vs SSS. The relationships between these spatial structures were investigated through a linear regression between the respective PCs. The scatterplot (Figure 26) revealed a strong linear relationship between the first PCs of rainfall in both cases, with an r^2 of 0.92 and the fourth PC of rainfall associated with SSS corresponded to the third PC of rainfall associated with the SST, with an r^2 of 0.67, both at a 95% confidence level. These results confirm that the rainfall patterns associated with El Niño 3.4 and the EMI were the same as those present in the analysis between rainfall and SSS. The structure found in EOF4 differed from the other EOF modes.

The fourth mode showed strong negative SSS anomalies that were associated with the high rainfall in the northwestern Amazon basin, however, the origin of the low salinity remained unclear, because part of this low salinity could also be a contribution from the ITCZ. Our analyses considered rainfall only over the continent, but the SSS signal had an influence from both the continent and rainfall over the ocean.

Figure 26. Linear regression between (a) the first PCs of EOF rainfall vs SSS by EOF SST vs rainfall and, (b) the fourth PC of EOF rainfall vs SSS by the third PC of SST vs rainfall, both at 95% confidence level.

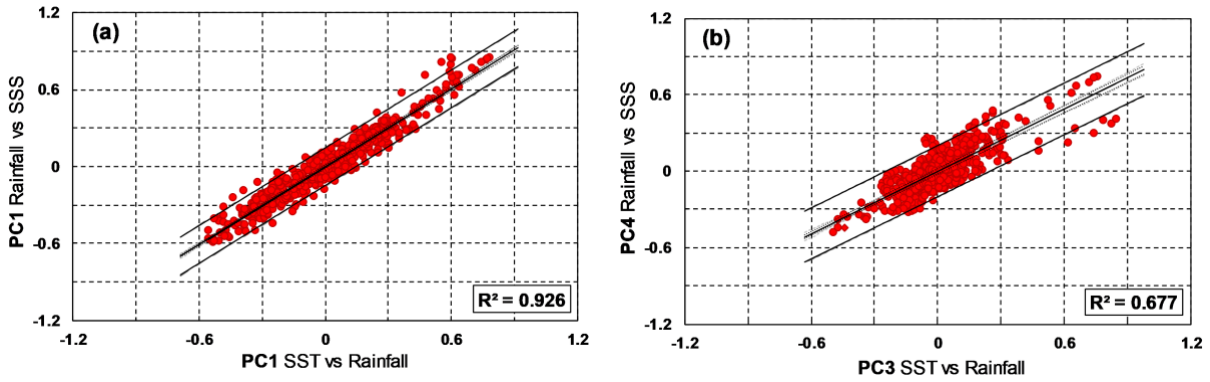

Source: the author

For example, in 2009 and 2012, the most serious floods of the last 40 years were recorded at the Manaus and Óbidos stations, due to the rising levels of the Solimões and Negro rivers, the two main branches of the Amazon River (Marengo et al., 2013). It is important to note that a strong and continuous La Niña Modoki occurred throughout 2008 (Shinoda et al., 2011). However, in 2009 there was also a very strong southern meridional event that was apparently not related to El Niño, which caused a very high anomalous change in the southern ITCZ and severe flooding in northeast Brazil. This southern mode was reported by Foltz et al. (2012). They argue that the anomalous cooling of SSTs in the equatorial North Atlantic triggered a strong southern-mode Atlantic event in April–May, with smaller SSTs in the equatorial North Atlantic and warmer SSTs in the equatorial South Atlantic. This event was characterized by abnormal north winds, causing an anomalous southward shift of the ITCZ and resulting in severe flooding in northeast Brazil.

In this study, we focused on 2009, because of the possible Atlantic oceanic influence in this year, whereas in 2012 there were no strong Atlantic SST anomalies. To better understand the role of the anomalous meridional shift in April–May 2009 and the previous La Niña Modoki event in 2008, in rainfall over the continent, we performed three-month composites of SSTs, rainfall, and surface wind anomalies, for the period of December of 2007 to November 2009 (Figure 27).

Figure 27. Three-month composites of SST, rainfall (normalized scale by 10^3) and surface wind anomalies, from December 2007 to November 2009. Anomalies of SST and rainfall were constructed over the period of 46 years.

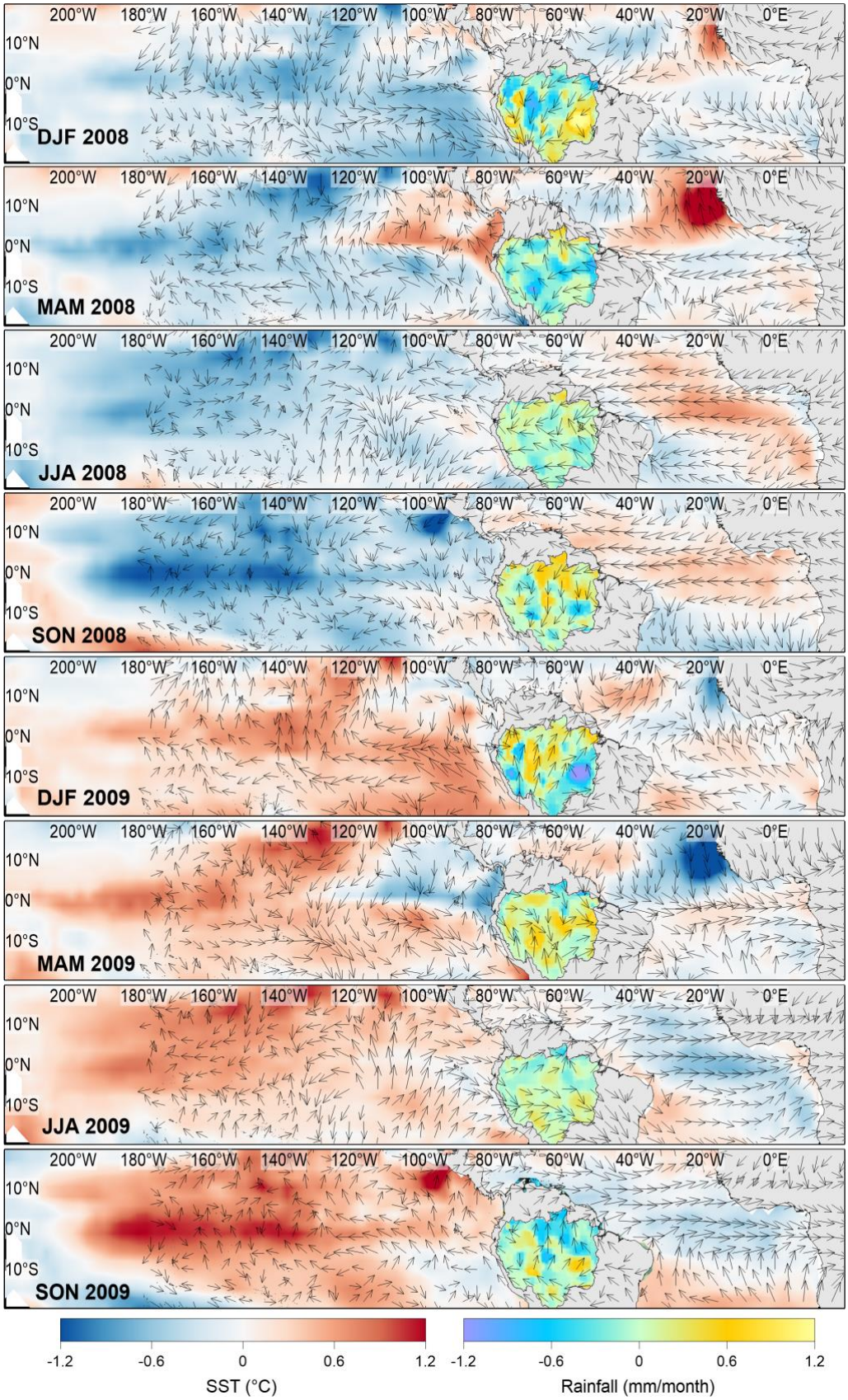

Source: the author

The evolution of the composites indicated an anomalous SST cooling in the Pacific at the beginning of 2008, with positive rainfall anomalies over the southeastern basin and northeast Brazil. During this period, the eastern north Atlantic was characterized by anomalously warmer SSTs and the western north Atlantic was colder than normal.

From March to May of 2008, cooler waters were present in the central Pacific, which was associated with the warm SSTs in the Eastern Pacific. This indicated a well-defined La Niña Modoki, and was reported by Shinoda et al. (2011). Higher than normal rainfall was concentrated in the northwestern part of the Amazon basin, while SST positive anomalies intensified in the eastern North Atlantic and the western North Atlantic remained colder.

From June to November of 2008, cold water remained in the central Pacific, with warmer SSTs in the eastern Pacific, while water in the north and central Atlantic was also warmer and there were positive rainfall anomalies over the northwest Amazon basin.
From December 2008 to February 2009, the Pacific SSTs presented an inverse signal, with warm water throughout the whole Pacific basin, but positive rainfall anomalies still persisting over the northwest Amazon basin.

The rainfall patterns in northwest South America only changed in March to May 2009, when negative rainfall anomalies were present, as a lagged response to the warming in the Pacific. In this period, a meridional dipole was present in the Atlantic, with negative SST anomalies in the North Atlantic and positive anomalies in the South Atlantic. This anomalous southern shift of warmer SSTs in March–April 2009 corroborates the results of Foltz et al. (2012), such as the positive rainfall anomalies over northeast Brazil. Simultaneously, in the Pacific area, the SST anomalies configure the presence of a positive phase of an El Niño Modoki event, with warmer waters in the central Pacific and colder waters in the eastern Pacific.

Despite the La Niña Modoki event that occurred during the whole of 2008, the southward shift of the ITCZ was also detected here, as reported by Foltz et al. (2012). Both events in the Pacific and Atlantic contributed to the increase of rainfall in the north of the Amazon basin throughout 2008 and at the beginning of 2009, which subsequently increased the river discharge anomalies.

To follow the sequence of events, the EMI signal was analysed with four month-lagged rainfall and river discharge normalized anomalies. The rainfall anomalies were constructed with the spatially averaged rainfall in the area of 0°–12°N and 53°–70°W, over the 46-year period, but the analysis was restricted between March 2008 and September 2009, as shown in Figure 28.

Figure 28. Monthly normalized anomalies of rainfall (mm/month), computed over the area of 0° - 12° N and 53° - 70° W (blue line), Amazon River discharge ($m^3 s^{-1}$) (green line) and EMI (red line) shifted + 4 months. Anomalies of SST and rainfall were constructed over the period of 46 years.

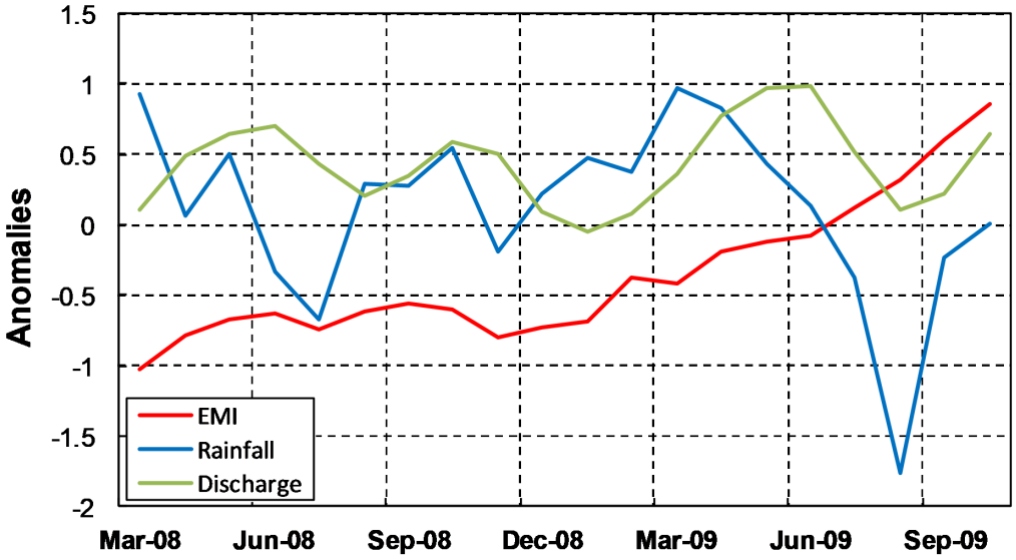

Source: the author

The negative phase of El Niño Modoki preceded the positive rainfall anomalies that peaked in March 2009, with a two-month lag to the strong river discharge anomaly, while the maximum southward shift of the ITCZ occurred in March–May. From March to May of 2008 (Figure 27), a clockwise vortex of surface winds was present over the northern part of South America and a second clockwise vortex was located over the eastern central Pacific, resulting in strong winds coming from the central Atlantic. In addition to this surface wind pattern, we analysed the omega field (height × time), averaged over a section between 75° and 80°W and fixed at 5°N.

The omega field represents the rate of change of pressure in a parcel over time (dp/dt), which is proportional to the vertical wind under hydrostatic balance. The vertical component of velocity in the pressure coordinates is positive in the downward direction. In this averaged section, we identified a strong ascending cell in the hovmöller diagram of the omega field (Figure 29). The upward vertical motion was represented by negative omega values, along the second half of 2008, from the surface to 200 hPa in the atmosphere. The ascending vertical motion favours the formation of convective clouds over the area. In this particular case, it seems to be that both phenomena contributed to an anomalous rainfall in the north of Amazon basin, consequently increasing a 2-month lagged Amazon River discharge anomaly in May of 2009.

Figure 29. Hovmöller diagram of monthly omega or vertical component of velocity in pressure coordinates (dp/dt), from 2008 to 2009, fixed at 5°N and averaged between 75°-80°W. Omega is positive down (Pa s^{-1}).

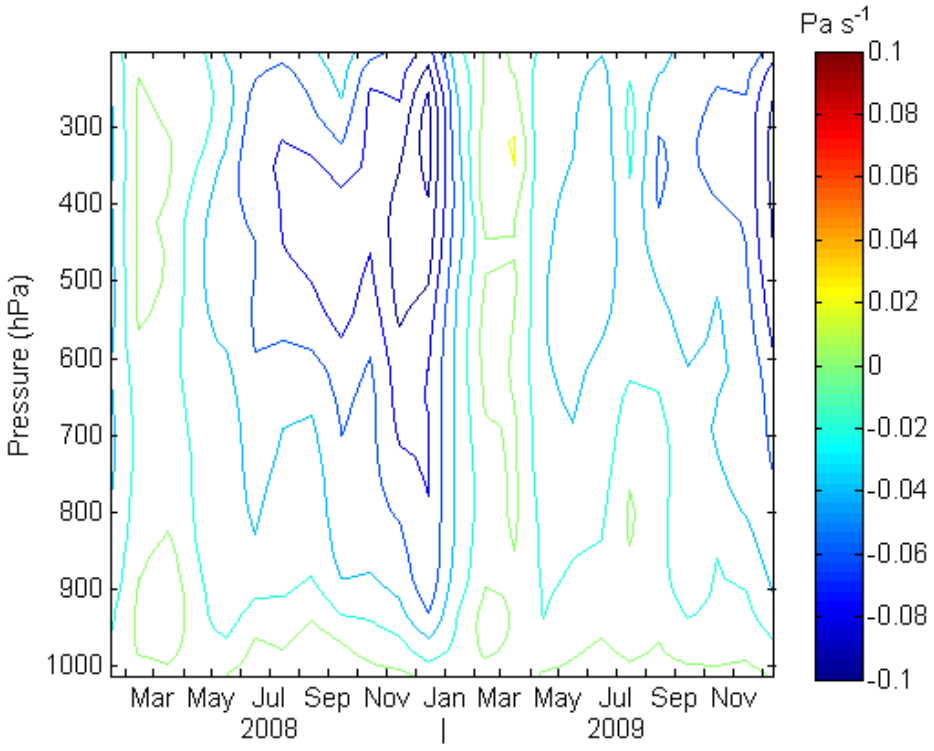

Source: the author

Our EOF analysis revealed an influence of La Niña Modoki events in the spatial pattern of precipitation in the Amazon Basin, highlighting the positive anomalies in the northwest portion of the Amazon Basin. These rainfall patterns were associated with the low SSS pattern in the Amazon River plume. In addition, our analysis focused on the specific period of 2008/2009, showing that La Niña Modoki events associated with an anomalous shift of the ITCZ in the Atlantic, had an important role in the development of convergence over the Amazon basin. Future studies should undertake an individual analysis of each Modoki event, which would improve these analyses and contribute to a better understanding of the role of La Niña Modoki events on the Amazon basin and river discharge. In addition, the influence of land rainfall vs ocean rainfall was quantified through a cross-correlation between the PC associated with EOF4 (rainfall vs SSS), and the rainfall anomalies over the land and ocean.

We used the rainfall anomalies from the GPCP 2.3 dataset, once it became available for both ocean and land. The results of the cross-correlation analysis between EOF4 PCs and rainfall anomalies are shown in Figure 30. The cross-correlation map indicated that the PC of EOF4 (rainfall vs SSS) was associated with rainfall over the continent.

Figure 30. Cross-correlation between EOF4 principal component and GPCP rainfall anomalies over land and ocean, from 1979 to 2015.

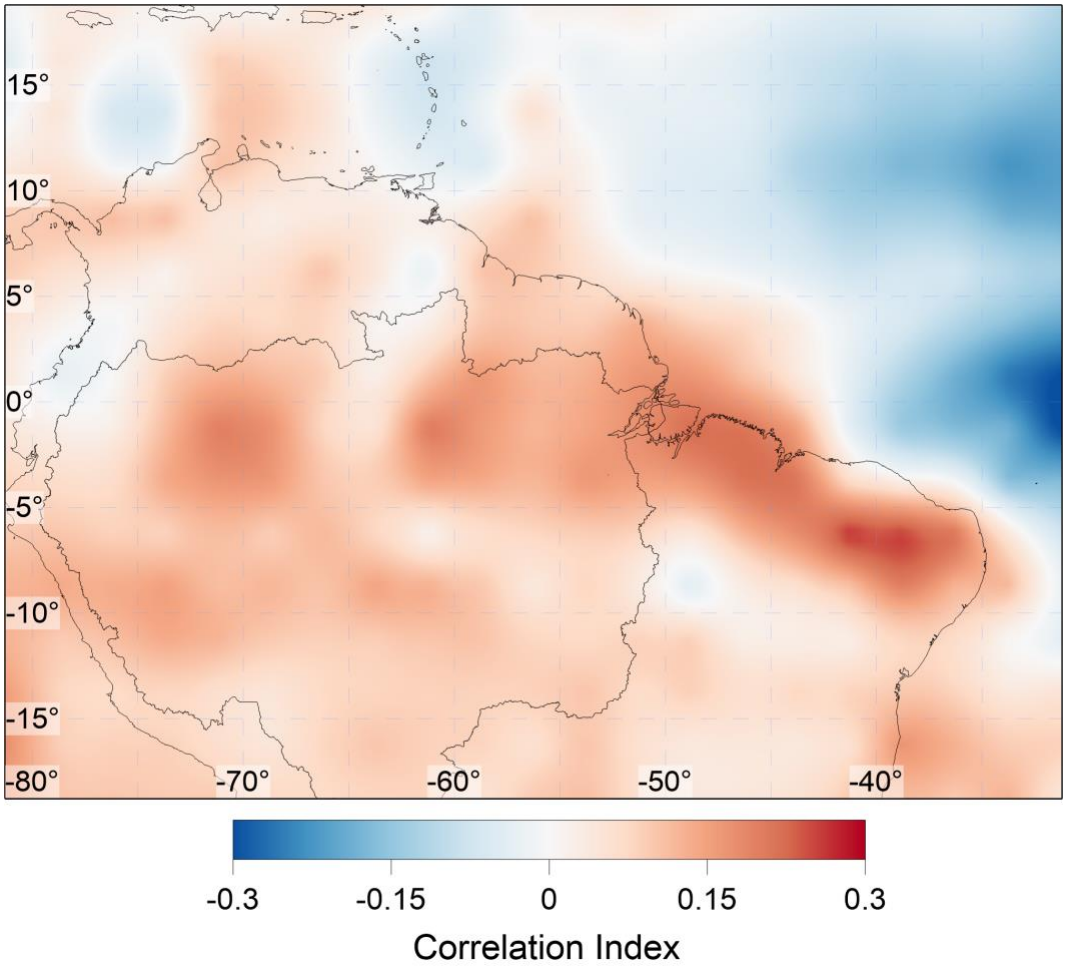

Source: the author

Conclusions

We used 46 years of ocean and atmospheric reanalysis data to show that interannual Pacific and Atlantic SST patterns can lead to different rainfall responses over the Amazon basin and, consequently can drive different interannual patterns in the SSS over the WTNA. The co-variability of SST and Amazon rainfall, and Amazon rainfall and surface salinity were examined using an EOF analysis. As in previous studies, links were found between El Niño and Atlantic indices and Amazon rainfall. The co-variability between rainfall and SSS demonstrated the existence of a strong positive SSS pattern along the coast. This was connected to negative rainfall anomalies over the whole of the Amazon basin, and was linked to canonical El Niño events. A second pattern also presented positive coastal SSS anomalies, when rainfall occurred predominantly over the northwestern part of the Amazon basin, with low rainfall around the Amazon River mouth.

The fourth EOF (rainfall vs SSS) had the lowest salinity pattern in the WTNA. This

pattern was associated with the third EOF (SST vs rainfall), when positive rainfall anomalies were concentrated in the northwest part of the Amazon basin. This relationship was confirmed through a linear regression between the two analyses. The low SSS pattern linked to this mode was characterized by a spatial structure similar to the Amazon plume dispersion, with an eastward retroflection following the pathway of the NECC. From the EOF and correlation analysis, we identified the negative phase of El Niño Modoki events as the main contributor to this mode. However, a detailed analysis was conducted for the years of 2008 and 2009, when anomalous rainfall in the north of the Amazon basin occurred, followed by an intense Amazon River discharge.

During 2008 a La Niña Modoki event occurred and in April–May of 2009 an anomalous southward shift of the ITCZ took place. Both phenomena resulted in increased SST anomalies in the southwest Atlantic and eastern Pacific, contributing to an intensification of the convergence of ocean winds to the continent. The convergence of surface winds contributed to a strong vertical cell of ascending winds that was present over the north of the Amazon basin from the surface to 200 hPa. In this particular case, both phenomena contributed to anomalous rainfall in the north of the Amazon basin, consequently increasing a two-month lagged Amazon River discharge anomaly in May of 2009.

Despite this particular case, the statistical analysis of the 46-year period indicated that La Niña Modoki events were important contributors to low SSS in the Amazon River plume. Our correlation results also provided evidence that the rainfall mode, associated with La Niña Modoki, responded better to rainfall anomalies over the continent. However, it is important to consider that not all SSS variability in the WTNA could be explained by changes in the Amazon discharge. Oceanic rainfall as well as advection are also important forcings of the SSS variability in this region, with strong boundary currents and strong SSS gradients created by the Amazon outflow, even in the absence of discharge anomalies. This pattern of low salinity makes an important contribution to other processes, such as an increase in productivity, and changes in the surface dynamics, mixed layer thickness, CO_2 fluxes, and light absorption. For example, light absorption is significantly enhanced in low salinity regimes (Subramanian et al., 2008), suggesting that the ocean color in the plume area can be traced back to the freshwater discharge.

In addition, the SSS in the Amazon plume has consequences for air-sea CO_2 exchange and has an impact on biogeochemical cycles. In the WTNA, surface waters with low salinity (< 35) are usually a sink of CO_2 from the atmosphere. The magnitude of these processes can be intensified according to the magnitude and frequency of El Niño Modoki events.

4.3 The relationship between aCDOM and salinity in the Amazon River plume

The third manuscript is being prepared for submission to the *Continetal Shlef Research* periodic. The paper has as main objective establishing CDOM absorption and salinity relationships over the Amazon plume. This paper is described as follow:

Abstract

Chromophoric dissolved organic matter (CDOM) absorption measurements and their relationship with salinity are presented for a highly dynamic oceanic environment. The results were obtained in the context of the Camadas Finas V oceanographic survey in 2014 in the Amazon Plume Continuum. Comparison between CDOM and salinity are considered. Establishing CDOM absorption (*a*CDOM) relationship with salinity is useful because absorption could therefore be inferred from salinity measurements which can be acquired more rapidly and with greater sensitivity than absorption. A significant relationship was identified between *a*CDOM and salinity in surface waters. The dependency of these two variables is especially evident on large input from continental runoff, reflecting the potential of CDOM absorption to be used as a passive tracer of freshwater input.

Keywords: Amazon plume, *a*CDOM, Salinity

Introduction

Chromophoric dissolved organic matter (CDOM; also referred as yellow substance and *gelbstoff* in German) is the fraction of dissolved organic matter (DOM) that interacts with solar radiation (Coble, 1996). CDOM compounds absorb light in the ultraviolet and visible range of the electromagnetic spectrum. This contribution implies that, the active radiation available for the phytoplankton is greatly reduced. Changes in the CDOM absorption can reflect the variations in CDOM composition from several autochthonous or allochthons sources resulting from physical, biological and chemical processes that occur in the water column (Coble, 1996; Del Castillo *et al*., 1999). It is produced naturally in the sea by the decay of organic material, but in estuaries and coastal zones there is a further source in the freshwater that drains trough the land and subsequently enters toward the ocean. CDOM is ubiquitous in the marine environment and spectroscopically unusual. The ultra-violet (UV) visible absorption spectrum of CDOM samples is typically smooth and declines with wavelength in an approximately exponential behaviour (Bricaud *et al*., 1981).

The importance of CDOM to aquatic ecosystems has been well established for some time, with its optical properties extensively studied over the last several decades. CDOM absorbs UV and visible light and is a major determinant of the optical properties of both fresh and marine waters, directly affecting the spectral quality of the underwater light field (Blough and Del Vecchio, 2002; Nelson and Siegel, 2002; Siegel *et al.*, 2002; Zepp *et al.*, 2007). CDOM is most often characterized by its absorption spectra, the absorption coefficient of CDOM (*a*CDOM) is typically evaluated at a specific wavelength, λ using:

$$a\text{CDOM}(\lambda) = \text{CDOM}(\lambda o) \times e^{S(\lambda-\lambda o)} \quad (9)$$

Where *a*CDOM is expressed in m^{-1} and S (nm^{-1}) is the spectral slope dependent on the type of CDOM present (Green and Blough, 1994). The value of S can be found by linear regression of log-transformed data (Bricaud et al., 1981) or by nonlinear fit of an exponential model to the *a*CDOM data (Stedmon and Markager, 2001, Twardowski *et al.*, 2004). Values of S depend strongly on the chosen wavelength interval and less strongly on the method used to find the parameter. In addition, nonlinear fits are less biased to longer-wavelength data (a problem when using linear fits to log-transformed aCDOM data) (Nelson and Siegel, 2013). Nevertheless, S values for *a*CDOM spectra in the visible and UV wavebands are typically in the range of 0.015-0.03 nm^{-1} for open ocean waters (Bricaud et al., 1981; Nelson et al., 2002).

Determining the chemical composition of the open ocean CDOM is subject to the same problems encountered while analysing dissolved organic carbon (DOC), with the added complication that CDOM is likely a small fraction of the total dissolved organic matter (DOM) pool (Yamashita and Tanoue, 2008). Spectroscopic analyses, including UV-visible absorption spectroscopy, remain the main useful technique for analysing the origin and composition of CDOM (Nelson and Coble, 2010).

CDOM is by far the most important factor regulating total absorption in the upper layers of the open ocean. Nearly 50% of the total light absorption at 400 nm and more than 70% of the total light absorption at 300 nm are due CDOM (Nelson and Siegel, 2013). Clearly, CDOM dominates light absorption throughout the blue and especially in the UV spectral regions of the open ocean. The other absorption components make a much smaller contribution to the total light absorption budget in the surface ocean. Phytoplankton absorption never dominates the open ocean spectral light absorption budget, and its contribution is only equal to that of CDOM absorption for wavelengths greater than 450 nm. Above 450 nm, seawater itself dominates light

absorption, thus, the *a*CDOM may be correlated to other environmental variables (Nelson and Siegel, 2013).

The ocean remote sensing (R/S) community has recently focused much attention on the study of CDOM in coastal areas, which often show anomalous and unique geophysical and hydrographical properties. To accommodate for the special requirements of these regions, specific or local algorithms must be formulated, in order to develop and validate these local R/S algorithms for current generation of satellite sensors. This study, as well as other less recent works, shows that despite the numerous sources of CDOM and the different characteristics of these sources, there appears to be a consistent and marked correlation between *a*CDOM and salinity.

Freshwater inputs may change the stratification and influence the nutrient flux and light regime in the upper mixed layer, thus controlling phytoplankton growth (Smith and DeMaster, 1996; Shipe et al., 2002). The Amazon River discharge, for example, is responsible for substantial algal blooms that occur on the Amazonian shelf (Milliman and Boyle, 1975; Edmond et al., 1981; DeMaster et al., 1996), confirming that the Amazon River is very important to the nutrient budgets of the shelf area. River plumes undergo with seawater as they move away from the shore. However, the buoyancy of the plume and very high CDOM concentrations can contribute to persistence such that plumes from large rivers can be discernible many kilometers from the coast. Muller-Karger et al. (2005) cite several examples where the influence of rivers on ocean color is visible in satellite imagery and has application to the study of ocean circulation, assessment of terrestrial inputs to coral reef ecology, and other coastal management issues.

This study has been focused on two different objectives:

(1) To obtain accurate *a*CDOM data at the levels found in the Amazon plume during an oceanographic survey. (2) To investigate the relationship between *a*CDOM and salinity.

Methods

CDOM samples were collected from September 18th to 24th of 2014 during oceanographic survey *Camadas Finas V* with an orientation towards the measurements of apparent optical properties (AOP) and inherent optical properties (IOP) of waters influenced by the Amazon River plume. This ship campaign was planned as the result of collaboration between the UFPE (*Universidade Federal de Pernambuco*) in Recife (Brazil), UVic (University of Victoria) in Victoria (Canada) and DHN (*Diretoria de Hidrografia e Navegação – Marinha do Brasil*) in Niterói (Brazil)

The station locations of this cruise are shown in Figure 31. The sampling was performed in two distinct zones: (1) Open Ocean (stations made after the shelf break) and (2) Shelf zone (stations made above the shelf that are strongly influenced by the Amazon River). These different zones were delimited according to the presumed (different) inputs of CDOM. A well-established correlation between an optically active component and a physical parameter (i.e. salinity), could therefore be used as an indicator of hydrography in those highly dynamic regions.

Figure 31. Sample stations from September 18th to 24th oceanographic survey along the Amazon River plume (shelf water, blue circles and red triangles; and open ocean, green squares). Attenuation coefficient at 490 nm (Kd490) is used to delimit the plume area. White pixels are no data.

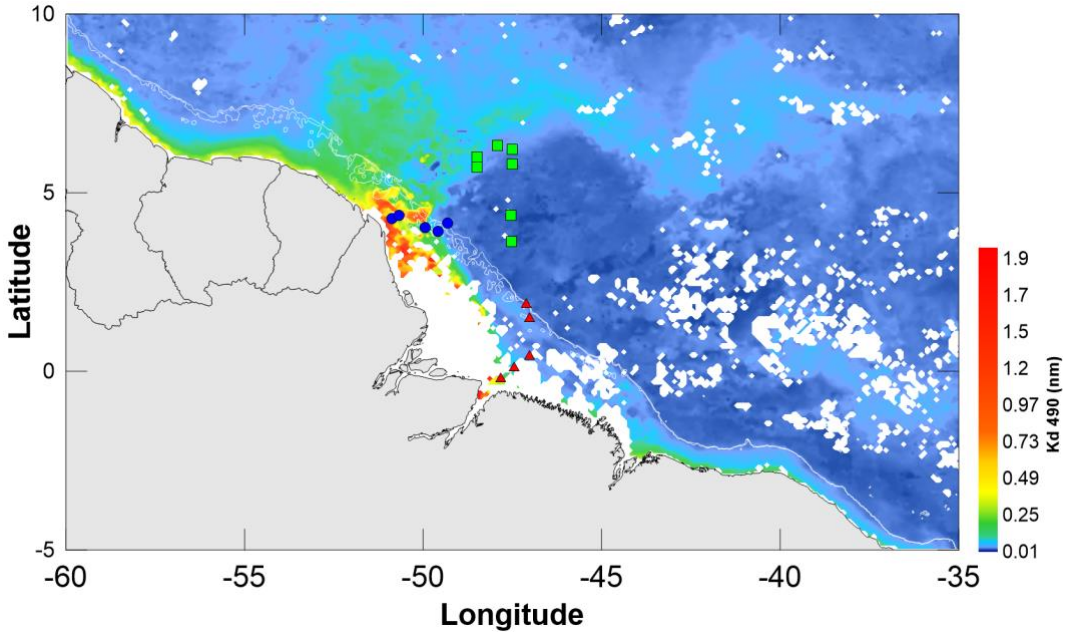

Source: the author

The area of Amazon plume defined as the area covered by water with sea surface salinity < 35 PSU. In this zone, the CDOM belongs to the pool of the background dissolved organic matter, which is a result of the biochemical degradation of organic matter either formed in situ or transported. The coastal zone is an area in which the quantities of CDOM are mainly influenced by the Amazon River input, which drain an intensive coastal-forested area. The western tropical North Atlantic (WTNA) presents unique features in light availability due CDOM properties affected by the high inputs from the Amazon River (mean discharge 1.7 x 10^4 m^3 s^{-1}), whose large drainage basin (approximately 6.915.000 km^2) is far main source of freshwater to the Atlantic Ocean (Wisser et al., 2010).

During the survey, salinity measurements was acquired with a SeaBird 911+ CTD probe. CDOM samples were collected using 10 l Niskin bottles from the CTD carrousel at a minimum of two depths. For each depth triplets were collected in 1 l Nalgene bottles and first filtered in Whatman GF/F of 0.7 μm of porosity membranes to separate the pigments. The leftover water was filtered in 0.2 μm acetate Pall membranes and stored in 100 ml amber bottles in a dark environment at 4 °C. The absorption measurements were performed 4 hours after the filtration in accordance with guidelines following storage test results as described by Loos and Costa, 2010. The filtrates of the 0.2 μm membrane was used for the CDOM absorption (*a*CDOM) measurements, which were performed directly onboard the vessel. These *a*CDOM values were obtained using an Ocean Optics USB4000 Spectrometer, following post-processing protocols as described by Pegau et al., 2003; Blough and Del Vecchio, 2002.

Results

As commented, CDOM is the main contributor to light absorption in the blue region of the spectrum in the Amazon plume waters. The contribution is considering the spectral range 400–500 nm, in which CDOM absorbs approximately three times more than the photosynthetic particles. Figure 32 illustrates absorption spectra averaged from the coastal stations 10, 11 and 13 for the September 2014 cruise

Figure 32. *a*CDOM in the surface waters (a) and maximum chlorophyll depth (b), from September 18th to 24th oceanographic survey along the Amazon River plume.

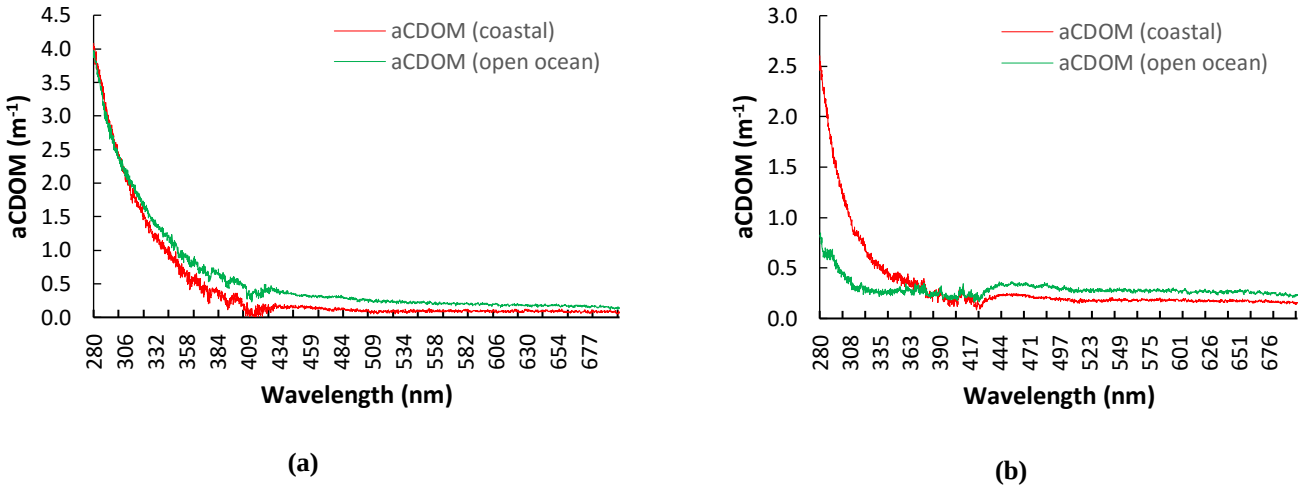

Source: the author

The general relationship between salinity and CDOM absorption is illustrated in Figure 33.

Figure 33. Correlations between *a*CDOM and salinity in the surface waters and maximum chlorophyll depth, from September 18th to 24th oceanographic survey along the Amazon River plume.

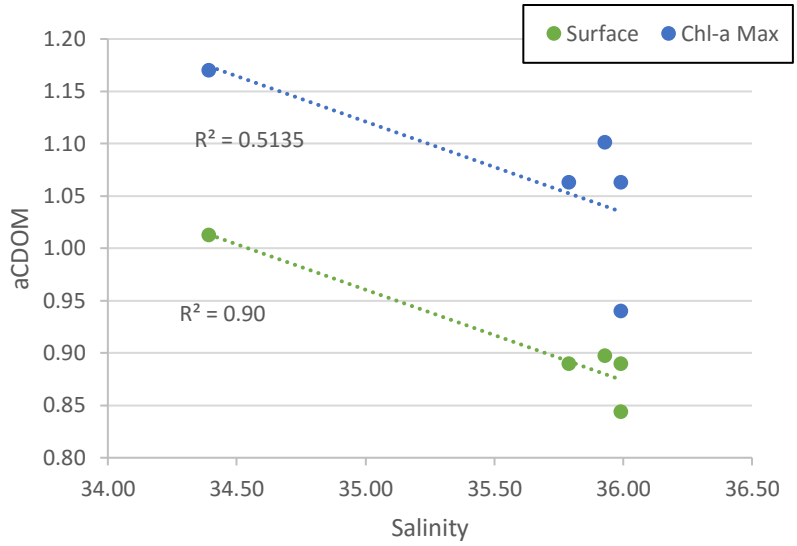

Source: the author

When considering only the surface water for the cited stations, a significant dependency of *a*CDOM on salinity is observed (r^2 = 0.90) as shown in Figure 33, so reflecting the conservative properties of CDOM in surface waters. The correlation should be considered as acceptable when the very low salinity gradients of the Amazon River with respect to the other areas is considered and the irregular distribution of the points. The derived regression equation is:

$$a\text{CDOM}_{(355)} = -0.0867 * \text{SAL} + 3.9967 \quad (10)$$

Where SAL is the salinity in practical salinity units. In this range, all of the samples show a signal measurable with good accuracy, whereas at the longer wavelengths the signal is low and may be affected by subparticle residual scattering. The spectral slope (S) is measured in the spectral range 400–600 nm subtracting, when existing, the baseline at 600 nm. This residual absorption is generally attributed to the subparticle backscattering. This correction is not applied in case of high CDOM absorption values (>25m^1 at 355 nm) of stations located close to the river mouths, rich in soluble humic matter where the absorbance is measurable even at 700 nm. The slope S1 has been found largely invariant despite the different sample collection areas and highly varying CDOM absorption. The constant nature of S (0·0197 ± 0.008) allows extrapolation the absorption at 412 nm which is the dedicated band sensitive to CDOM absorption of the MODIS/Aqua satellite sensor.

The data would suggest the need to use a different slope (0·0177 ± 0·0014) in such extrapolation, although, with respect to 0·0197, the error would be 12%, with an overlapping of the respective error bands. The correlation coefficients shown in the Figure 333 are also extremely high apart from those of the open sea where no significant correlation was found.

This is, however, explained by the fact that there is almost no variability in the salinity and *a*CDOM when this data set is considered independently. Furthermore, it was found, when the best fit line for the whole data set was compared to a best fit line for the subset excluding the higher values from stations 12 and 17, that the slope was essentially the same.

Discussion and conclusions

The results show that CDOM absorption values are significantly correlated with the salinity in surface waters. The dependency is especially evident through- out the water column with a large input from continental runoff. Therefore, the semi-conservative nature of CDOM with respect to salinity would imply that its use as a passive tracer of fresh water input and therefore local hydrography in this region is supported. It is however obvious that although this relationship exists, it is purely a local relationship which does not coincide with the more general relationships identified to date (Doerffer et al., 1995). This is undoubtedly due to the high gradient of CDOM in the Amazon plume continuum and relatively low gradient of salinity.

The spectral slope seems to be dependent of the geographical site. Moreover, the spectral absorption characteristics of CDOM are not strictly dependent on the various sources and on the total amount of CDOM for the area investigated. The results presented in this study confirm that CDOM absorption can be derived from standardized salinity measurements using a general expression that appears to be valid for diverse marine and coastal waters. The open ocean area shows a larger variability, mainly due to the lack of low *a*CDOM data (0-1m^{-1}), while a general observation is that, if the high river values are removed, the intercept increases.

This variation can be explained by the diminished contribution to the CDOM pool due to riverine and estuarine sources which are characterized by a high quantum yield of CDOM. This aspect is, at present, poorly investigated and requires further study. Recent works have demonstrated that relative to the areas and seasons investigated *a*CDOM can be used to infer DOC concentration (Vodacek et al., 1995; Ferrari et al., 1996). This opens the possibility for using R/S products (active or passive aCDOM on large areas) to assess DOC concentration in surface marine waters. The potential of CDOM as passive tracer, should provide a good indication of surface patterns and especially of freshwater dispersion.

5 CONCLUSIONS AND PERSPECTIVES

This work aims to contribute to a better understanding of the Pacific and Atlantic oceans climate teleconnections effects over the western tropical North Atlantic (WTNA) specifically regarding to the chlorophyll-*a* (*Chl*) and sea surface salinity (SSS) over the Amazon River plume. To derive the special and temporal patters of this these variables remote sensing images and modelling data was used applying statistical methods as cross-correlations and empirical orthogonal functions (EOF).

The Amazon River plume itself represents a site of intense physical, biogeochemical and ecological complexity. Being considered the largest source of fresh water in the Atlantic Ocean, this plume varies spatially and temporally throughout the year, governed by events of maximum and minimum discharge of the Amazon River, Intertropical Convergence Zone (ITCZ) precipitation over the sea, trade winds and ocean currents in the region like the North Brazilian Current (NBC) and North Equatorial Counter Current (NECC).

As the main local climate index, the Tropical Atlantic Dipole plays an important role in the climate dynamics over the Brazilian coast. The SST pattern is dominant on decadal timescales. It has a period of about 12 years, with the SST positive anomalies around the Equator. This decadal scale SST pattern constitutes one of the key features of SST variability in the Tropical Atlantic Ocean, with another one being the Atlantic Equatorial Mode or Atlantic Niño, which occurs in the zonal (east-west) direction at interannual timescales, with SST anomalies being observed in the eastern equatorial basin.

Brazil is one of the key regions that are severely affected by Tropical Atlantic Dipole variability. More specifically, an anomalous displacement of the ITCZ toward the north leads to anomalous rainfall patterns and thus significant drying over NE Brazil; this is also associated with a pattern of anomalous warm SST in the northern tropical Atlantic and with directly opposite conditions across the southern tropical Atlantic. On the other hand, SST across the tropical Pacific described as El Niño Southern Oscillation (ENSO) contribute significantly to the observed patterns of tropical rainfall. The mean patterns of sea surface temperature in and equatorial rainfall are accompanied by low level easterly winds. As recent studies have shown that canonical El Niño events are less frequent and Modoki El Niño occurring more frequently in recent decades, with this last, presenting a great influence in the positive rainfall anomalies over the Amazon basin.

The results presented in the 4.1 section here revealed a strong seasonal and interannual cycle dominating the variability of *Chl* in the western tropical North Atlantic (WTNA). The results showed distinct surface *Chl* concentration patterns concerning different ENSO phases

(El Niño - La Niña) and indexes (canonical and Modoki), which is linked to river discharge variability due to higher rainfall over the Amazon Basin. The seasonal and interannual variability of *Chl* concentrations in the study area is the result of different stages in the local and remote forcing. *Chl* is influenced by the river discharge (Q), SST, meridional wind stress (τy) and zonal currents (u) variability on a seasonal scale. The *Chl* distribution and concentration over the WTA is influenced by nutrient supply from the high Q, by southeast τy and u east intensification, where nutrients are carried eastward to the open ocean. Also, ENSO variability have strong influence in the Q and *Chl* concentration not only at seasonal scales, but throughout the year as *Chl* positive anomalies are linked to strong rainfall/Q events influenced by canonical (La Niña phase) and more strongly by Modoki (La Niña/El Niño) modes with an interannual variability.

In the section 4.2, 46 years of SST, rainfall and SSS data indicated that La Niña Modoki events were important contributors to low SSS in the Amazon River plume. Correlations also provided evidence that, the rainfall mode, associated with La Niña Modoki, corresponds to rainfall anomalies over the continent. It is important to consider that not all SSS variability in the WTNA could be explained by changes in the Amazon discharge. Oceanic rainfall provided by the ITCZ, as well as advection are also important forcings of the SSS variability in this region, with strong boundary currents and strong SSS gradients created by the Amazon outflow, even in the absence of discharge anomalies.

Knowledge of the heterogeneity of *Chl* concentration in oligotrophic waters is essential for understanding the dynamics of marine ecosystems. As the main optical variable, *Chl*-a plays an important role in biogeochemistry by phytoplankton photosynthesis. Besides that, changes in salinity patterns caused by large river plumes indicate where marine and land systems mix, ocean salinity variability is an indicator of changes in the global hydrological cycle and large-scale climatic variability. The SSS plays an important role in thermohaline circulation and mass and heat distribution and also reflects the patterns of ocean-atmosphere fluxes, evaporation and precipitation, heat, energy, and solubility.

These results (sections 4.1 and 4.2) presented in this manuscript show that the influence of El Niño Modoki on rainfall in the Amazon basin has been a preponderant factor for the positive anomalies in the concentration of *Chl* and negative anomalies of salinity in the Amazon River plume. The *a*CDOM results presented in section 4.3, provide an indication of freshwater dispersion. Satellite and modelled derived *Chl* and SSS, *a*CDOM patterns over the Amazon plume can give us a portrait concerning the biogeochemical variability. These results also support future studies on large-scale climatic variability, thermohaline circulation, global

hydrological cycle, sediments deposition, biogeochemistry, ocean-atmosphere fluxes, CO_2 uptake and ecological impacts on the food chain in the WTNA.

References

Antonov J. I., Locarnini, R. A., Boyer, T. P., Mishonov, A. V., Garcia H. E., 2006. World Ocean Atlas 2005, Volume 2: Salinity. NOAA Atlas NESDIS 62, NOAA, U.S. Government Printing Office, Washington D.C.

Araujo, M., Noriega, C., Lefèvre, N. 2014. Nutrients and carbon fluxes in the estuaries of major rivers flowing into the tropical Atlantic. Front. Mar. Sci. 1. doi: 10.3389/fmars.2014.00010

Ashok, K., Behera, S. K., Rao, S. A., Weng, H., Yamagata, T., 2007. El Niño Modoki and its possible teleconnection. J. Geophys. Res. 112, C11007. doi: 10.1029/2006JC003798.

Ashok, K., Yamagata, T., 2009. Climate change: The El Niño with a difference. Nature 461, 481–484. doi:10.1038/461481a.

Balaguru, K., P., Chang, R., Saravanan, L. R., Leung, Z., Xu, M., Li, L., Hsieh, J.S., 2012. Ocean Barrier layers' effect on tropical cyclone intensification, PNAS, 109 (36), 14343–14347, doi:10.1073/pnas.1201364109.

Balmaseda, M.A., Vidard, A., Anderson, D.L., 2008: The ECMWF Ocean Analysis System: ORA-S3. Mon. Wea. Rev., 136, 30183034, https://doi.org/10.1175/2008MWR2433.1.

Balmaseda, M. A., Mogensen, K., Weaver, A. T., 2013. Evaluation of the ECMWF ocean reanalysis system ORAS4. Q.J.R. Meteorol. Soc., 139: 1132–1161. doi:10.1002/qj.2063.

Belkin, I. M., 2009. Rapid warming of Large Marine Ecosystems. Prog. Oceanogr. 81, 207–213.

Beluco, A., Souza, P. K. D., 2014. Energy at the junction of the rivers Negro and Solimões, contributors of the Amazon River, in the Brazilian Amazon. Int. Schol.Res. Notic. doi:10. 1155/2014/794583.

Blough, N. V., Del Vecchio, R., 2002.Chromophoric DOM in the Coastal Environment, in: Biogeochemistry of Marine Dissolved Organic Matter, edited by: Hansell, D.A.and Carlson, C. A., Academic Press, San Diego, 509–540.

Brandt, P. et al., 2006. Circulation in the central equatorial Atlantic: Mean and intraseasonal to seasonal variability. Geophys. Res. Lett. 33, L07609. doi:10.1029/2005GL025498.

Bretherton, C., Smith, C., Wallace, J., 1992. An Intercomparison of Methods for Finding Coupled Patterns in Climate Data. J. Clim., 5, 541 – 560. doi:10.1175/15200442005%3C0541: AIOMFF%3E2.0.CO;2

Bricaud, A., Morel, A., Prieur, L., 1981. Absorption by dissolved organic-matter of the sea (yellow substance) in the UV and visible domains. Limnology and Oceanography 26 (1), 43-53.

Cane, M., 1983. Oceanographic events during El Niño, Science, 222(4629), 1189–1195

Chang, P., L. Ji, H. Li, 1997: A decadal climate variation in the tropical Atlantic Ocean from thermodynamic air–sea interactions. Nature, 385, 516–518

Coble, P. G. 1996. Characterization of marine and terrestrial DOM in seawater using excitation emission spectroscopy. Mar. Chem., v. 51, p. 325-346.

Coles, V. J., Brooks, M. T., Hopkins, J., Stukel, M. R., Yager, P. L., Hood, R. R., 2013. The pathways and properties of the Amazon River Plume in the tropical North Atlantic Ocean, J. Geophys. Res. Oceans, 118, 6894–6913,doi:10.1002/2013JC008981.

Cooley S. R., Coles V. J., Subramaniam A., Yager P. L., 2007. Seasonal variations in the Amazon plume-related atmospheric carbon sink. Glob. Biogeochem. Cycles, doi:21GB301410.0129/2006GB002831

Dai, A. and Trenberth, K. E. 2002. Estimates of Freshwater Discharge from Continents: Latitudinal and Seasonal Variations. J. Hydrometeorol. 3, 660 – 687.

Del Castillo, C. E.; Coble, R. E.; Morell, J. M.; Lopez, J. M.; Corredor, J. E., 1999. Analysis of the optical properties of the Orinoco River plume by absorption and fluorescence spectroscopy.Mar. Chem.,v. 66, p. 35-51.

DeMaster, D. J., Smith, W. O., Nelson, D. M., Aller, J. Y. 1996, Biogeochemical processes in Amazon shelf waters: chemical distributions and uptake rates of silicon, carbon and nitrogen. Cont. Shelf Res. 16, 617–643.

Di Lorenzo, E., Liguori, G., Schneider, N., Furtado, J. C., Anderson, B. T. and Alexander, M. A., 2015. ENSO and meridional modes: A null hypothesis for Pacific climate variability, Geophys. Res. Lett., 42, doi:10.1002/2015GL066281.

Doerffer, R., Sorensen, K. and Aiken, J., 1995. MERIS: potential for coastal zone application. Proceedings of the 21st Annual Conference of the Remote Sensing Society. pp. 166–175.

Du, Y., Zhang, Y., Feng, M., Wang, T., Zhang, N. and Wijffels, S., 2015. Decadal trends of the upper ocean salinity in the tropical Indo-Pacific since mid-1990s. Sci.Rep., 5, 16050. http://doi.org/10.1038/srep16050.

Ducet N, Le Traon P-Y, Reverdin G., 2000. Global high-resolution mapping of ocean circulation from TOPEX/POSEIDON and ERS-1/2. J Geophys Res 105:19477–19498.

Edmond, J. M., Boyle, E. A., Grant, B. and Stallard, R. F., 1981. The chemical mass balance in the Amazon plume I: The nutrients. Deep Sea Res. Part A. Oceanogr. Res. Pap.28, 1339–1374.

Enfield, D.B., A.M. Mestas-Nuñez, D.A. Mayer, and Cid-Serrano. L., 1999. How ubiquitous is the dipole relationship in tropical Atlantic sea surface temperature? Journal of Geophysical Research 104: 7841–7848.

Ferrari, G. M., Dowell, M. D., Grossi, S. and Targa, C., 1996. Relationship between optical properties of chromophoric dissolved organic matter and total concentration of dissolved organic carbon in the Southern Baltic Sea region. Marine Chemistry 55, 299–316.

Ferry, N., and Reverdin, G., 2004. Sea surface salinity interannual variability in the western tropical Atlantic: An ocean general circulation model study, J. Geophys. Res., 109, C05026, doi:10.1029/2003JC002122.

Ffield, A., 2007. Amazon and Orinoco River Plumes and NBC Rings: Bystanders or Participants in Hurricane Events?. J. Climate, 20, 316-333, doi.:10.1175/JCLI3985.1.

Foltz, G.R., M.J. McPhaden, Lumpkin R., 2012. A Strong Atlantic Meridional Mode Event in 2009: The Role of Mixed Layer Dynamics. J. Clim., 25, 363–380, https://doi.org/10.1175/JCLI-D-11-00150.1.

Foltz, G.R., Schmid, C., Lumpkin, R., 2015. Transport of Surface Freshwater from the Equatorial to the Subtropical North Atlantic Ocean. J. Phys. Oceanogr. 45, 1086-1102.

Fratantoni, D. M. and Glickson, D. A., 2002, North Brazil Current Ring Generation and Evolution Observed with SeaWiFS. J. Phys. Oceanogr. 32, 1058–1074.

Froidefond, J. M.; Gardel, L.; Guiral, D. l.; Parra, M.; Ternon, J. F., 2002. Spectral remote sensing reflectances of coastal waters in French Guiana under the Amazon influence. Remote Sensing of Environment v. 80, n. 2, p. 225– 232.

Garçon V, Oschlies A, Doney S, McGillicuddy D, Waniek J., 2001. The role of mesoscale variability on plankton dynamics in the North Atlantic. Deep Sea Res II 48:2199–2226.

Geider J. R., et al., 2001. Primary productivity of planet earth: biological determinants and physical constraints in terrestrial and aquatic habitats. Glob. Chan. Biol., 7,849-882.

Geyer, W. R. and Beardsley, R. C., 1995. Introduction to special section on Physical Oceanography of the Amazon Shelf. J. Geophys. Res. 100, 2281 - 2282.

Girard C, Sudre J, Benhamou S, Roos D, Luschi P., 2006. Homing in green turtles Chelonia mydas: oceanic currents act as a constraint rather than as an information source. Mar Ecol Prog Ser 322:281–289.

Green, S. A. and Blough, N. V., 1994. Optical absorption and fluorescence properties of chromophoric dissolved organic matter in natural waters. Limnology and Oceanography 38, 1903–1916.

Grimm, A.M.; Barros, V.R.; Doyle, M.E., 2000. Climate variability in southern South America associated with El Niño and La Niña events. J. Clim., 13: 35-58.

Grimm, A. M., 2003. The El Niño impact on summer monsoon in Brazil: Regional processes versus remote influences. J. Clim., 16, 263–280.

Grimm, A. M., 2004. How do La Niña events disturb the summer monsoon system in Brazil? Climate Dyn., 22, 123–138.

Grodsky, S. A., Reul, N., Lagerloef, G., Reverdin, G., Carton, J. A., Chapron, B., Quilfen, Y., Kudryavtsev, V. N., and Kao, H.Y., 2012. Haline hurricane wake in the Amazon/Orinoco plume: AQUARIUS/SACD and SMOS observations, Geophys. Res. Lett., 39, L20603, doi:10.1029/2012GL053335.

Grodsky, S. A., G. Reverdin, J. A. Carton, and V., Coles J., 2014a. Year-to-year salinity changes in the Amazon plume: Contrasting 2011 and 2012 Aquarius/SACD and SMOS satellite data, Remote Sens. Environ., 140, 14–22, doi:10.1016/j.rse.2013.08.033.

Grodsky, S. A., J. A. Carton, Bryan, F. O., 2014b. A curious local surface salinity maximum in the northwestern tropical Atlantic, J. Geophys. Res. Oceans, 119, 484–495, doi:10.1002/2013JC009450.

Grodsky, S. A., Johnson, B. K., Carton, J. A., and Bryan, F. O., 2015. Interannual Caribbean salinity in satellite data and model simulations, J. Geophys. Res. Oceans, 120, 1375 – 1387, doi:10.1002/2014JC010625.

Hellweger, F. L., and Gordon, A. L., 2002. Tracing Amazon River water into the Caribbean Sea, J. Mar. Res., 60, 537–549, doi:10.1357/ 002224002762324202.

Hickey, B. M. et al., 2010. River Influences on Shelf Ecosystems: Introduction and synthesis. J. Geophys. Res. 115, C00B17. doi: 10.1029/2009JC005452.

Hounsou-Gbo, G.A., Servain, J., Araujo, M., Martins, E.S., Bourlès, B. and Caniaux, G., 2016. Oceanic Indices for Forecasting Seasonal Rainfall over the Northern Part of Brazilian Northeast. *American Journal of Climate Change*, **5**, 261-274. http://dx.doi.org/10.4236/ajcc.2016.52022.

Hu, C., Lee, Z., and Franz, B., 2012. Chlorophyll-a algorithms for oligotrophic oceans: A novel approach based on three-band reflectance difference. Journal of Geophysical Research, 117(C1). doi: 10.1029/2011jc007395.

Ibánhez, J. S. P., Flores, M., and Lefèvre, N., 2017. Collapse of the tropical and subtropical North Atlantic CO_2 sink in boreal spring of 2010. Sci.Rep., 7, 41694. http://doi.org/10.1038/srep41694.

Jiménez-Muñoz, J. C. et al., 2016. Record-breaking warming and extreme drought in the Amazon rainforest during the course of El Niño 2015–2016. Sci. Rep., 6, 33130.http://doi.org/10.1038/srep33130.

Johns, W. E., Lee, T. N., Schott, F. A., Zantopp, R. J. and Evans, R. H., 1990. The North BrazilCurrent retroflection: Seasonal structure and eddy variability. J. Geophys. Res. 95, 22103.

doi: 10.1029/JC095iC12p22103.

Johns, W.E., Lee, T.N., Beardsley, R.C., Candela, J., Limeburner, R., Castro, B., 1998. Annual cycle and variability of the North Brazil Current. J. Phys. Oceanogr., 28, 103 – 128.

Jutla, A. S., Akanda, A. S., Griffiths, J. K., Colwell, R. and Islam, S., 2011. Warming Oceans, Phytoplankton, and River Discharge: Implications for Cholera Outbreaks. Am. J. Trop. Med. Hyg. 85, 303–308 (2011).

Kao, H.Y., and J.Y. Yu, 2009. Contrasting Eastern-Pacific and Central-Pacific Types of ENSO, J. Clim., 22(3), 615–632, doi:10.1175/2008JCLI2309.1.

Kelly P. S., Lwiza K. M. M., Cowen R. K., and Goni G. J., 2000. Low-salinity pools at Barbados, West Indies: Their origin, frequency, and variability, J. Geophys. Res., 105(C8), 19,699–19,708.

Korosov, A., F. Counillon, Johannessen J. A., 2015. Monitoring the spreading of the Amazon freshwater plume by MODIS, SMOS, Aquarius, and TOPAZ, J. Geophys. Res. Oceans, 120, 268–283, doi:10.1002/2014JC010155.

Körtzinger, A., 2003. A significant CO_2 sink in the tropical Atlantic Ocean associated with the Amazon River plume. Geophys. Res. Lett. 30, 2287. doi: 10.1029/2003GL018841.

Kossin, J. P. and Vimont, D. J., 2007. A More General Framework for Understanding Atlantic Hurricane Variability and Trends. Bull. Am. Meteorol. Soc. 88, 1767–1781.

Kug, J.S., Jin, F.F. and An, S.I., 2009. Two Types of El Niño Events: Cold Tongue El Niño and Warm Pool El Niño. J. Clim. 22, 1499–1515.

Kulkarni, M. N., and Siingh, D., 2016. The atmospheric electrical index for ENSO modoki: Is ENSO Modoki one of the factors responsible for the warming trend slowdown? Sci. Rep., 6, 24009. http://doi.org/10.1038/srep24009.

Labat, D., 2004. Wavelet analysis of Amazon hydrological regime variability. Geophys. Res. Lett. 31, L02501. doi: 10.1029/2003GL018741.

Laraque A, Ronchail J, Cochonneau G, Pombosa R, Guyot JL., 2007. Heterogeneous distribution of rainfall and discharge regimes in the Ecuadorian Amazon basin. Journal of hydrometeorology 8: 1364–1381.

Lee, T., and M. J. McPhaden, 2010. Increasing intensity of El Niño in the central-equatorial Pacific, Geophys. Res. Lett., 37, L14603, doi:10.1029/2010GL044007.

Lefèvre, N., Caniaux, G., Janicot, S. and Gueye, A. K., 2013. Increased CO_2 outgassing in February-May 2010 in the tropical Atlantic following the 2009 Pacific El Niño. J. Geophys. Res. Ocean. 118, 1645–1657.

Lefèvre, N., Diverrès, D., and Gallois, F., 2010. Origin of CO_2 undersaturation in the western

tropical Atlantic. Tellus, Series B: Chem. Phys. Meteorol., 62, 595–607. doi:10.1111/j.1600-0889. 2010.00475.x.

Lentz, S. J., 1995. Seasonal variations in the horizontal structure of the Amazon Plume inferred from historical hydrographic data, J. Geophys. Res., 100(C2), 2391–2400, doi:10.1029/94JC01847.

Li, W., Zhang, P., Ye, J., Li, L., and Baker, P. A., 2011. Impact of two different types of El Niño events on the amazon climate and ecosystem productivity. J. Plant Ecol. 4, 91–99. doi:10.1093/jpe/rtq039.

Liebmann, B. and Marengo, J., 2001. Interannual Variability of the Rainy Season and Rainfall in the Brazilian Amazon Basin. J. Clim. 14, 4308–4318.

Locarnini R A, Mishonov A V, Antonov J I, Boyer T P and Garcia H. E., 2006. World Ocean Atlas 2005, Volume 1: Temperature. NOAA Atlas NESDIS 61, NOAA, U.S. Government Printing Office, Washington D.C.

Loos, E. A., and Costa, M., 2010. Inherent optical properties and optical mass classification of the waters of the Strait of Georgia, British Columbia, Canada. Progress in Oceanography, 87(1), 144–156.

Madec G., 2008. NEMO ocean engine. Note du Pôle de modélisation, Institut Pierre Simon Laplace (IPSL), France, No 27, ISSN No 1288-1619.

Marengo, J. A., 1992. Interannual variability of surface climate in the Amazon basin. Int. J. Clim., 12: 853–863. doi:10.1002/joc.3370120808.

Marengo, J. A.; Espinoza, J. C., 2015. Extreme seasonal droughts and floods in Amazonia: causes, trends and impacts. Int. J. Clim., 36: 1033-1050.

Marengo, J.A., Alves, L.M., Soares, W.R., Rodriguez, D.A., Camargo, H., Riveros, M., and Pabló, A., 2013. Two Contrasting Severe Seasonal Extremes in Tropical South America in 2012: Flood in Amazonia and Drought in Northeast Brazil. J. Clim., 26, 9137–9154, doi: 10.1175/JCLI-D-12-00642.1.

Marengo, J.A., Nobre, C.A., Tomasella, J., Oyama, M.D., Sampaio de Oliveira, G., de Oliveira, R., Camargo, H., Alves, L.M., and Brown, I., 2008. The Drought of Amazonia in 2005. J. Clim., 21, 495–516, doi: 10.1175/2007JCLI1600.1.

McKee, B. A., Aller, R. C., Allison, M. A., Bianchi, T. S. and Kineke, G. C., 2004. Transport and transformation of dissolved and particulate materials on continental margins influenced by major rivers: benthic boundary layer and seabed processes. Cont. Shelf Res. 24, 899–926.

McPhaden, M. J., Lee, T. and McClurg, D., 2011. El Niño and its relationship to changing background conditions in the tropical Pacific Ocean. Geophys. Res. Lett. 38. doi:

10.1029/2011GL048275.

Meyer-Christoffer, A.; Becker, A.; Finger, P.; Rudolf, B.; Schneider, U.; Ziese, M., 2011. GPCC Climatology Version 2011 at 0.25°: Monthly Land-Surface Precipitation Climatology for Every Month and the Total Year from Rain-Gauges Built on GTS-Based and Historic Data; GPCC: Offenbach, Germany.

Meyer-Christoffer, A.; Becker, A.; Finger, P.; Rudolf, B.; Schneider, U.; Ziese, M., 2015. GPCC Climatology Version 2015 at 0.25◦ : Monthly Land-Surface Precipitation Climatology for Every Month and the Total Year from Rain-Gauges Built on GTS-Based and Historic Data; GPCC: Offenbach, Germany.

Milliman, J. D. and Boyle, E., 1975. Biological uptake of dissolved silica in the Amazon river estuary. Science 189, 995 – 997.

Misra, V., 2008a. Coupled interactions of the monsoons. Geophys. Res. Lett., 35, L12705, doi:10.1029/2008GL033562.

Misra, V., 2008b. Coupled air, sea, and land interactions of the South American monsoon. J. Clim., 21, 6389–6403.

Morrow RA, Fang F, Fieux M, Molcard R., 2003. Anatomy of three warm-core Leeuwin Current eddies. Deep Sea Res II 50:2229– 2243.

Muller-Karger, F.E., McClain, C.R., Richardson, P.L., 1988. The dispersal of the Amazon water. Nature. 333, 56–59.

Muller-Karger, F. E., R. Varela, R., Thunell, R., Luerssen, C., Hu, And J. J. Walsh., 2005. The importance of continental margins in the global carbon cycle. Geophys. Res. Lett. 32: L01602.

Nelson NB, Coble PG., 2010. Optical analysis of chromophoric dissolved organic matter. In Practical Guidelines for the Analysis of Seawater, ed. O Wurl, pp. 79–96. Boca Raton, FL: CRC.

Nelson, N. B. and Siegel, D. A., 2002. Chromophoric DOM in the Open Ocean, in: Biogeochemistry of Marine Dissolved Organic Mat- ter, edited by: Hansell, D. A. and Carlson, C. A., Academic Press, San Diego, 547–578.

Nelson, N.B., Siegel, D.A., 2013. The global distributon and dynamics of chromophoric dissolved organic matter. Annu. Rev. Mar. Sci., 5:447–76.

Nittrouer, C.A. E Demaster, D.J., 1996, The Amazon shelf setting: tropical, energetic, and influenced by a large river, Continental Shelf Research, v. 16, n. 5/6, pp. 553-573.

Noriega, C., Araujo, M., 2014. Carbon dioxide emissions from estuaries of northern and northeastern Brazil. Sci. Rep. 4, 6164. doi: 10.1038/srep06164.

O'Reilly, J.E. et al., 1998. Ocean color chlorophyll algorithms for SeaWiFS, Journal of

Geophysical Research 103, 24937-24953, doi: 10.1029/98JC02160.

O'Reilly, J. E. et al., 2000. SeaWiFS postlaunch calibration and validation analyses, part 3. Tech. Rep. NASA Technical Memorandum 2000- 206892, Volume 11, NASA.

Paegle, J.N. and Mo K.C., 2002. Linkages between summer rainfall variability over South America and sea surface temperature anomalies. J. Clim, 15:1389-1407.

Pegau, S., Zaneveld, J. R. V., Mitchell, B. G., Kahru, M., Wieland, J., Stramska, M., 2003. Ocean optics protocols for satellite ocean color sensor validation, Revision 4, Volume IV: Inherent optical properties: Instruments, characterizations, measurements and data analysis protocols. Tech. Rep. NASA/TM-2003-211621/Rev4-Vol.IV, NASA Goddard Space Flight Space Center.

Rasmusson, E. M., and T. H. Carpenter, 1982: Variations in tropical sea surface temperature and surface wind fields associated with the Southern Oscillation/El Niño. Mon. Wea. Rev., 110, 354-384.

Regnier, P. et al., 2013. Anthropogenic perturbation of the carbon fluxes from land to ocean. Nat. Geosci. 6, 597–607.

Reul, N. et al., 2014. Multisensor observations of the Amazon-Orinoco river plume interactions with hurricanes. J. Geophys. Res. Ocean. 119, 8271–8295 (2014).

Richardson, P. L., G. Hufford, R. Limeburner, and W. Brown, 1994. North Brazil Current retroflection eddies, J. Geophys. Res., 99, 5081–5093.

Rodrigues, R. R., Haarsma, R. J., Campos, E. J. D. and Ambrizzi, T., 2011. The Impacts of Inter–El Niño Variability on the Tropical Atlantic and Northeast Brazil Climate. J. Clim. 24, 3402–3422.

Ronchail, J., Cochonneau, G., Molinier, M., Guyot, J.L., Chaves, A.G.D., Guimarães, V., de Oliveira, E., 2002. Interannual rainfall variability in the Amazon basin and sea-surface temperatures in the equatorial Pacific and the tropical Atlantic Oceans. Int. J. Clim., 22:1663 - 1686.

Salisbury, J., Vandemark, D., Campbell, J., Hunt, C., Wisser, D., Reul, N., Chapron, B., 2011. Spatial and temporal coherence between Amazon River discharge, salinity, and light absorption by colored organic carbon in western tropical Atlantic surface waters. J. Geophys. Res., 116, C00H02. doi: 10.1029/2011JC006989.

Santos, M. L. S. et al., 2008a. Influence of the Amazon and Pará Rivers on Water Composition and Phytoplankton Biomass on the Adjacent Shelf. J. Coast. Res. 243, 585–593.

Santos, M. L. S., Muniz, K., Barros-Neto, B. and Araujo, M., 2008b. Nutrient and phytoplankton biomass in the Amazon River shelf waters. An. Acad. Bras. Cienc. 80, 703–717.

Sarmiento, J. L. et al., 2004. Response of ocean ecosystems to climate warming. Global Biogeochem. Cycles 18. doi: 10.1029/2003GB002134.

Sathyendranath, S., Cota, G., Stuart, V., Maass, H., Platt, T., 2001. Remote sensing of phytoplankton pigments: a comparison of empirical and theoretical approaches. International Journal of Remote Sensing 22 (2-3), 249-273.

Schmitt R. N. W., 2008. Salinity and the global water cycle. Oceanography. 21, 12–19.

Schneider, U., Becker, A., Finger, P., Meyer-Christoffer, A., Ziese, M., and Rudolf, B., 2014. GPCCS's new land surface precipitation climatology based on quality-controlled in situ data and its role in quantifying the global water cycle. Theor. Appl. Climatol., 115, 15–40. doi:10.1007/ s00704-013-0860-x.

Schneider, U., Becker, A., Finger, P., Meyer-Christoffer, A., Rudolf, B., Ziese, M., 2015. GPCC Full Data Reanalysis Version 7.0 at 0.5°: Monthly Land-Surface Precipitation from Rain Gauges built on GTS-based and Historic Data. DOI: 10.5676/DWD_GPCC/FD_M_V7_050.

Schwalb, A., 1978. The TIROS-N/NOAA A-G satellite series, NOAA Tech. Memo., NESS 95, 75 pp.

Servain, J., Caniaux, G., Kouadio, Y. K., McPhaden, M. J. and Araujo, M., 2014. Recent climatic trends in the tropical Atlantic. Clim. Dyn. 43, 3071–3089.

Shinoda T. Hurlburt H. E. and Metzger E. J., 2011. Anomalous tropical ocean circulation associated with La Niña Modoki. J. Geophys. Res. 116, C12001, doi:10.1029/2011JC00730.

Shipe, R. et al., 2002. Effects of the 1997–98 El Niño on seasonal variations in suspended and sinking particles in the Santa Barbara basin. Prog. Oceanogr. 54, 105–127.

Siegel, D. A., Maritorena, S., Nelson, N. B., Hansell, D. A., and Lorenzi-Kayser, M., 2002: Global distribution and dynamics of col- ored dissolved and detrital organic materials, J. Geophys. Res., 107(C12), 3228, doi:10.1029/2001JC000965.

Silva, A. C. da, Santos, M. de L. S., Araujo, M. C. and Bourlès, B., 2009. Observações hidrológicas e resultados de modelagem no espalhamento sazonal e espacial da pluma de água Amazônica. Acta Amaz. 39, 361–369.

Smith, W.O. Jr., Demaster, D.J., 1996. Phytoplankton and biomass productivity in the Amazon river plume: correlation with seasonal river discharge. Cont. Shelf Res. 16: 291-317.

Stedmon, C.A., Markager, S., 2001. The optics of chromophoric dissolved organic matter (CDOM) in the Greenland Sea: an algorithm for differentiation between marine and terrestrially derived organic matter. Limnol. Oceanogr. 46 (8), 2087–2093.

Subramanian, A. et al., 2008. Amazon River enhances diazotrophy and carbon sequestration in the tropical north Atlantic Ocean. Proc. Natl. Acad. Sci. U S A., 105, 10460–5.

doi:10.1073/pnas.0710279105.

Tokinaga, H and Xie, S., 2011. Weakening of the equatorial Atlantic cold tongue over the past six decades. Nat. Geosci. 4. 222-234. http://dx.doi.org/10.1038/ngeo1078.

Twardowski M.S., Boss E., Sullivan J.M., Donaghay P.L., 2004. Modeling the spectral shape of absorption by chromophoric dissolved organic matter. Mar. Chem. 89:69–88.

Uvo, C., C.A. Repelli, S.E. Zebiak, and Y. Kushnir, 1998. The Relationships between Tropical Pacific and Atlantic SST and Northeast Brazil Monthly Precipitation. J. Clim., 11, 551–562, doi: 10.1175/1520-0442(1998)011<0551:TRBTPA>2.0.CO;2.

Vodacek, A. et al., 1995. The use of in situ and airborne fluorescence measurements to determine UV adsorption coefficients and DOC concentrations in surface waters. Limnology and Oceanography 40, 411–415.

Wallace, J., Smith, C., and Bretherton, C., 1992. Singular Value Decomposition of Wintertime Sea Surface Temperature and 500-mb Height Anomalies. J. Clim., 5, 561–576. doi:10.1175/1520-0442(1992)005%3C0561:SVDOWS%3E2.0.CO;2

Walton, C. C., W. G. Pichel, and J. F. Sapper, 1998. The development and operational application of non-linear algorithms for the measurement of sea surface temperatures with the NOAA polar-orbiting environmental satellites, J. Geophys. Res., 103, 27,999-28,012.

Wang, X. and Wang, C., 2014. Different impacts of various El Niño events on the Indian Ocean Dipole. Clim. Dyn. 42, 991–1005.

Weng, H., Ashok, K., Behera, S. K., Rao, S. A., and Yamagata, T., 2007. Impacts of recent El Niño Modoki on dry/wet conditions in the pacific rim during boreal summer. Clim. Dyn. 29, 113–129. doi:10.1007/s00382-007-0234-0.

Wilks, D.S., 1995. Statistical methods in the atmospheric sciences: An introduction. San Diego: Academic Press, 467p.

Wisser, D., Fekete, B. M., Vörösmarty, C. J. and Schumann, A. H., 2010. Reconstructing 20th century global hydrography: a contribution to the Global Terrestrial Network- Hydrology (GTN-H). Hydrol. Earth Syst. Sci. 14, 1–24.

Wyrtki, K., 1975. El Niño-The dynamic response of the equatorial Pacific Ocean to atmospheric forcing. Journal of Physical Oceanography. 5(4), 572-584.

Xie, F., Li, J., Tian, W., Li, Y., and Feng, J., 2014. Indo-pacific warm pool area expansion, Modoki activity, and tropical cold-point tropopause temperature variations. Sci.Rep., 4, 4552. doi:10. 1038/srep04552.

Yamashita Y, Tanoue E., 2008. Production of bio-refractory fluorescent dissolved organic matter in the ocean interior. Nat. Geosci. 1:579–82.

Yeh, S.W., and B. P. Kirtman., 2004. Tropical Pacific decadal variability and ENSO amplitude modulations in a CGCM. J. Geophys. Res., 109, C11009, doi:10.1029/2004JC002442.

Yeh, S.W. et al., 2009. El Niño in a changing climate. Nature 461, 511–4. doi:10.1038/nature08316.

Yi, D., Mysak, L.A., Venegas, S.A., 1999. Singular value decomposition of Arctic sea ice cover and overlying atmospheric circulation fluctuations. Atmos-Ocean 37:389–415.

Yu L., Jin X., and Weller R. A., 2007. Annual, seasonal, and interannual variability of air-sea heat fluxes in the Indian Ocean. J. Clim., 20, 3190–3209.

Yu, J. Y., Kao, H. Y., and Lee, T., 2010. Subtropics-related interannual sea surface temperature variability in the central equatorial pacific. J. Clim., 23, 2869–2884. doi:10.1175/2010JCLI3171.1.

Yu, J.-Y., and S. T. Kim, 2010. Three evolution patterns of Central-Pacific El Niño, Geophys. Res. Lett., 37, L08706, doi:10.1029/ 2010GL042810.

Zepp, R.G., Erickson III, D.J., Paul, N.D., Sulzberger, B., 2007. Interactive effects of solar UV radiation and climate change on biogeochemical cycling. Photochem. Photobiol. Sci. 6 (3), 286–300.